Hollow-Electrode Pulsed Plasma Deposition of Titanium and Carbon Thin Films

by

Robert H. Hyde

A thesis submitted in partial fulfillment
of the requirements for the dual degrees of
Master of Science
Department of Physics
College of Arts and Science
and
Master of Science in Engineering Science
Department of Electrical Engineering
College of Engineering
University of South Florida

Major Professor: Pritish Mukherjee, Ph.D.
Sarath Witanachchi, Ph.D.
George S. Nolas, Ph.D.
Yun-Leei Chiou, Ph.D.
Andrew M. Hoff, Ph.D.

Date of Approval:
November 13, 2006

Keywords: anode, cathode, pulsed, arc, PFN

DEDICATION

Sincerest thanks to Lisa Michele Hyde.

ACKNOWLEDGEMENTS

I would like to express my appreciation to Dr. Pritish Mukherjee and Dr. Sarath Witanachchi for their support and guidance during this project.

I would like to thank Dr. Yun-Leei Chiou, Dr. Andrew M. Hoff, and Dr. George S. Nolas for serving on my examining committee.

Many thanks to the following people who helped in many ways, the members of LAMSAT: Houssam Abou Mourad, James Winslow, and John Cuff, and to the Physics department staff: Sam Valenti, Phil Bergeron, and Sue Wolfe.

TABLE OF CONTENTS

LIST OF FIGURES

LIST OF TABLES

LIST OF ABBREVIATIONS

A_V	area under the recorded voltage signal
A_I	area under current signal
CO_2	carbon dioxide
C	capacitance
CAPD	cathodic arc plasma deposition
CVD	chemical-vapor deposition
Δd	deposition rate
E_C	energy discharged from the PFN capacitor stage
EDS	energy dispersive x-ray spectroscopy
FWHM	full width at half maximum
HSS	high-speed steel
ICCD	intensified charged-coupled device
IV	current-voltage relation
$I(t)$	current
k_I	current signal proportionality constant
k_V	voltage signal proportionality constant
OMA	optical emission spectroscopy
PFN	pulse forming network
PLD	pulsed laser ablation
psi	pounds per square inch

PVD	physical vapor deposition
RF	radio frequency
q	charge
SEM	scanning electron microscopy
TEA	transversely excited at atmosphere pressure
TOF	time of flight
V_f	PFN final discharge voltage
V_i	PFN initial voltage
V_s	voltage source
XRD	x-ray iffraction
ZnSe	zinc selenide
$Z(t)$	impedance

HOLLOW-ELECTRODE PULSED PLASMA DEPOSITION OF TITANIUM AND CARBON THIN FILMS

Robert H. Hyde

ABSTRACT

This thesis presents a study of a pulsed distributed arc plasma deposition method that has been developed to produce highly ionized pulsed plasma plumes of metallic species in the presence of a low-pressure inert or reactive gas glow discharge. A pulse-forming network (PFN) is used to form a transient electrical discharge in a hollow electrode which is triggered by two different methods; a pulsed CO_2 laser or a pulsed high voltage glow discharge. With the PFN charged to a voltage of 70 - 100 VDC, current pulses with peak currents up to 3 kA and pulse widths as long 3.7 milliseconds have been reached. A detailed treatment of the influence of process parameters, such as the PFN discharge energy and ambient gas pressure and type, on the plasma properties is presented. These experiments also demonstrated a higher on-axis growth rate of carbon in an ambient of nitrogen than in argon. The higher argon mass leads to broader plasma expansion producing broader deposition profiles which results in lower on-axis growth rates. Deposition rates of 3.5 Å/pulse for carbon and 2.1 Å/pulse for titanium have been achieved. Thickness profiles and the morphology of carbon films and titanium films deposited by this method, which utilize the energetic advantage of ions in film formation allowing reduced substrate temperatures and good adhesion, are presented.

CHAPTER 1. PULSED PLASMA THIN FILM DEPOSITION: INTRODUCTION AND OVERVIEW

This chapter serves as an introduction to cathodic arc plasma deposition for thin film growth, including its advantages and disadvantages. The motivation for the project is also discussed in detail. The studies conducted as part of this project and the layout of the project is summarized in Section 1.2.

1.1. Introduction

Physical vapor deposition (PVD) techniques for depositing metal vapor on a substrate can be divided into three main groups: evaporation, sputtering, and ion plating. Specific techniques from these groups currently used for PVD hard coatings are: low voltage electron beam evaporation, magnetron sputtering, and cathodic arc deposition [1]. The differences between these deposition techniques are the way that the source material is vaporized, the way in which the plasma is created, and the number and types of ions, electrons, and gas atoms that constitute the plasma [2].

The traditional evaporation and sputtering techniques were found to be inadequate for the deposition of hard, wear-resistant films because of the relatively low deposition energies they produce. Conventional thermal evaporation produces atoms of the source material in the vapor state with energies in the range of 0.1 to 0.6 eV. Sputtering improves upon these energies, emitting atoms with energies in the range of 4.0 to 10 eV.

In both cases the depositing species are neutral atoms and afford limited options to increase their deposition energy which is lower than what is required to produce the level of adhesion and film properties needed. The properties and structure of the deposited coatings can be modified by increasing the substrate temperature during deposition, or by applying a bias to the substrate. In many situations, the nature of the substrate limits the temperature that can be used. The utilization of these options still failed to produce coatings that could tolerate the conditions created in many wear-related applications [3].

The momentum for the development of a higher energy deposition technique came from the high-speed steel (HSS) cutting tool industry. As an example of a technique used, a chemical-vapor deposition (CVD) process had been employed to apply hard coatings of titanium nitride to carbide cutting tools. The 1000 ºC temperature required for the process exceeded the annealing temperature of the tools. A method was needed that produced coatings having high adhesion and density without requiring high substrate temperatures during deposition. The ion plating processes, which achieve good coating qualities by ion bombardment as opposed to elevated temperature, fulfilled these conditions.

1.1.1. Ion Plating

The energies of a deposition process can be significantly enhanced if the substrate and growing film are continuously bombarded by energetic ions; this is the basis of ion plating [4]. The term ion plating is defined as a film deposition process in which the substrate surface and growing film are subjected to a flux of high energy ions sufficient to cause appreciable sputtering prior to and/or during deposition. The depositing species, in the case of evaporative and sputter ion plating, are ionized after leaving the source. A

high negative bias voltage applied to the substrate created the ionizing plasma discharge and accelerates the resulting ions to the substrate [5 – 8].

Bombardment of the substrate during film growth has a number of effects on the coating being deposited. Bombardment produces the creation of vacancy and interstitial point defects and the disruption of surface crystallography and morphology. Bombardment during interface formation results in physical mixing between the depositing species and the substrate surface and in enhanced inter-diffusion. The bombarding ions sputter more of the loosely bound atoms from the developing surface, with the net result that the more tightly bound atoms dominate the adhesion mechanism. The dependence of the film morphology and structure on temperature is significantly diminished, to the extent that they are temperature-independent in most circumstances [9, 10]. Other physical properties, such as hardness and yield strength, may also be beneficially affected by bombardment. A practical benefit of these bombardment effects is the ability to deposited high-quality, dense, hard films at relatively low substrate temperatures [11, 12].

In the basic ion plating process only 0.1 to 1.0% of the atoms are ionized meaning the majority of the depositing species in evaporative and sputter ion plating are neutral. The low arrival energy of these neutrals at the substrate leaves them relatively weakly bound and therefore more prone to being sputtered off the surface by the energetic bombarding ions. Cathodic arc plasma deposition (CAPD) belongs to the ion plating family of high-energy deposition processes. The CAPD process, by comparison, generates a very high degree of ionization of the source material, with the result that a high percentage of the depositing species are energetic ions that become tightly bound.

As a consequence of the reduced re-sputtering, the CAPD process provides higher net deposition than can be achieved by the alternative ion plating techniques.

1.1.2. Arc Plasma Deposition

Cathodic arc deposition is a PVD technique by which a source material is vaporized under an arcing condition. There are two types of arc evaporation sources. One is the thermionic arc, and the other is the cathode arc or the anode arc. The anodic arc has ionization processes quite different from the cathodic arc. The regularly interchanged terms are, but not limited to, vacuum arc, metal vapor vacuum arc, arc plasma, and arc vapor deposition. A cathodic arc is a low-voltage, high-current discharge between metal electrodes in a vacuum. The cathodic arc is characterized by inter-electrode metal plasma which is generated at the cathode spots. The term ‘metal’ refers to all solid conductive materials, including alloys, carbon, and doped semiconductors [13]. Very high deposition rates combined with highly ionized plasma can be easily achieved by arc plasma deposition, much more than by sputtering [14].The cathodic arcs also occur at elevated gas pressure when the gas participates significantly in the discharge processes. The importance of the cathodic arc plasma discharge lies in its abundant and efficient production of metal plasma and its simplicity, features that make it well suited for film deposition applications [15].

At the cathode, the target of the vacuum arc, the current is concentrated at a small number of discrete sites called cathode spots. The cathode spot size is very small, from 10^{-8} to 10^{-4} m^2, and acts as an intense plasma source, capable of a current density of 10^6 – 10^{12} $A \cdot m^{-2}$. The spot is formed by an explosive process, the plasma pressure within a cathode spot is high, and the strong pressure gradient causes the plasma generated to

plume away from the surface similar to the plasma plume generated by a focused laser beam at a target surface [16]. The current carried by a cathode spot is typically a few to a few tens of amperes, depending on the metal, and if the arc is caused to conduct a higher total current, then more cathode spots are formed; thus a typical cathodic arc discharge of several hundred amperes arc current might involve the participation of several tens of cathode spots [15]. The arc spot is active for a short period of time, then self-extinguishes and re-ignites in a new location adjacent to the previous arc crater causing an apparent motion of the arc [3].

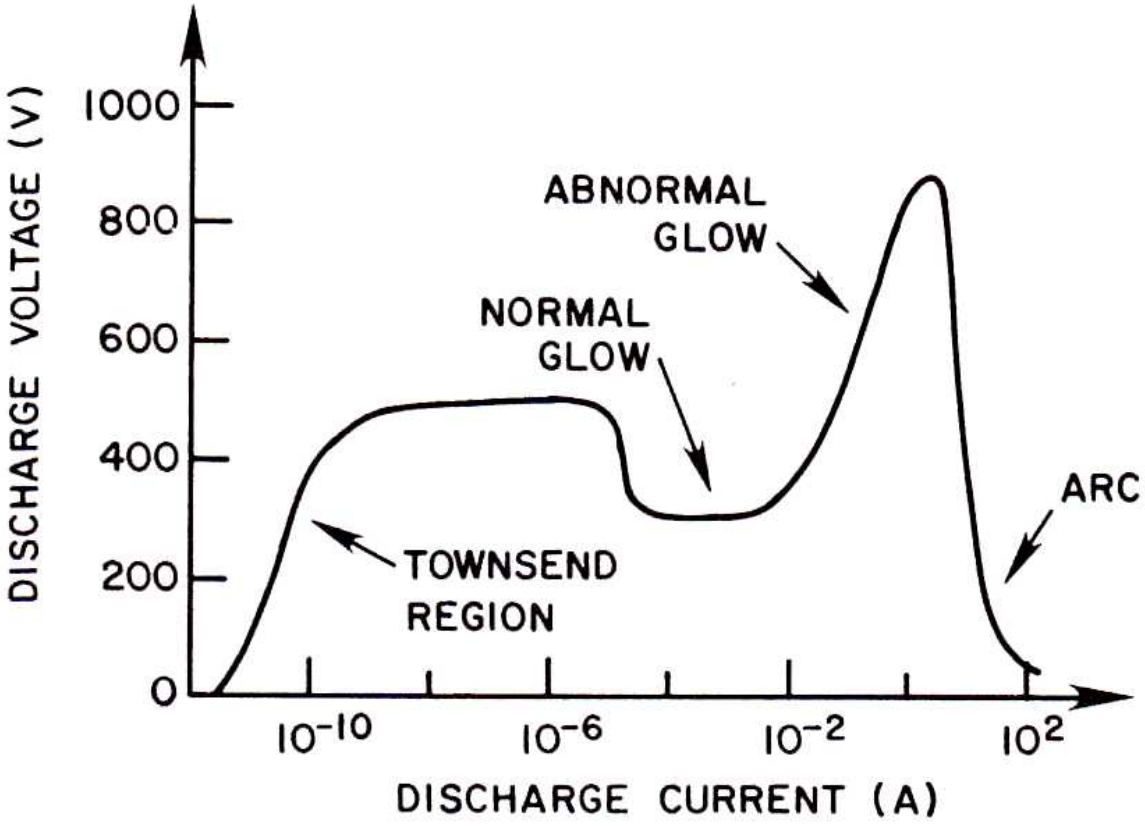

Figure 1.1. Current-voltage relation for various types of plasma discharges between two powered electrodes. Reprinted from J. L. Vossen, et. al., Thin Film Processes II, pg 21, San Diego: Academic Press, (1991).

'Breakdown' is a condition that rapidly occurs when secondary electrons cause further ionization of the gas or vapor. The discharge, for a DC discharge, that develops

between the electrodes following breakdown has a number of modes, depending on the current level, as shown in Figure 1.1. Starting from a low discharge current and increasing, the discharge modes are the Townsend region, normal glow, abnormal glow, and arc. As the ionizing discharge is increased, by small increases in voltage, the coverage of the cathode by the glow also increases. Eventually, the entire cathode surface is covered, and further increases in the discharge current require much larger increases in discharge voltage. This is the abnormal glow region and is the mode most often used in processing plasmas. At higher and higher discharge currents, the cathode will heat significantly, either to the point of melting or, if it is constructed of refractory materials, to the point of thermionic electron emission. This latter, low voltage, high current mode is known as an arc. The structure of the discharge modes will depend on the geometry of the electrodes and chamber, the gas, and the electrode material [17].

There are three types of arc processes which have been mainly adopted into thin film technology:

1) Continuous arc;
2) Distributed arc, and;
3) Pulsed arc.

The continuous arc process is supplied by a DC power source. The disadvantages with this process are principally the macro-particle production, the confinement of the arc on the cathode surface, and the cathode design where high thermal power dissipation must be obtained, in the range of a few kW.

In the distributed arc process, vaporization of the source material can be obtained, choosing the proper source, at the anode or at the cathode: the current densities are lower than in the continuous cathodic arc process, but melting of anode or cathode is generally

obtained [18]. This technique can does not produce micro-droplets and atoms emitted are singly ionized.

The pulsed arc is similar to the continuous arc, but the power source is pulsed: in such a way that water cooling of the sources can be reduced or even omitted, and a reduced erosion of the target is obtained. An important aspect of this kind of source is that the ion charge state of the emitted atoms depends on the pulse frequency [17].

1.1.3. Ion Emission

The principal advantage of arc evaporation for film deposition lies in the high percentage of ions in the emitted flux, on the order of 10-100%, and the high kinetic energy of these ions, in the range of 40-100 eV [19]. Techniques based on pulsed laser ablation (PLD) such as single laser ablation produce plumes with a percentage of ionization as low as 8% [19] and dual-laser ablated plumes can be over 70% ionized [21]. The presence of these energetic ions in the film growth processes is desirable, since many of the benefits of ion-assisted deposition may be realized. These benefits include enhanced adhesion, increased film packing density, and high reactivity for compound film formation [22].

The plasma ions form the material required for film deposition, and as a result some of the ion flux generated at the cathode spots serves to carry the arc current, along with the much greater electron flux, and some is diverted to be used for deposition at a location distant from the arc itself. A characteristic of the vacuum arc discharge is the relationship between the metal ion flux that is generated at the cathode spots and the current that drives the arc. Crossed electric and magnetic fields have been used to extract the ion current from the arc source flux [23]. For all cathode materials and for typical arc

currents in the several hundred amperes range, the plasma current is a constant fraction of the arc current,

$$I_{ion} = \varepsilon I_{arc} \qquad [1.1]$$

where $\varepsilon \approx 0.10 \pm 0.02$. The magnitude of the ion current leaving the cathode is approximately 10% of the arc current for a wide range of metals [15, 24-25].

	Degree of Ionization (%)			
Arc Current	**I**	**II**	**III**	**IV**
50	26	55	19	0.6
100	30	54	15	0
200	31	55	14	0.3

Table 1.1. The fractional distribution of ion flux from copper. I is singly ionized, II is doubly ionized, etc. Reprinted from J. L. Vossen and W. Kern (eds.), Thin Film Processes II, pp 239, (1991).

High average ion energies, greater than the potential difference between the cathode and the anode, have been explained in terms of a potential peak associated with the extremely dense plasma located close to the cathode surface. The energy distributions of various ions are similar: the fraction of singly charged ions increases with increasing arc current, the location of the ion-energy distribution peak shifts to lower energies as the degree of ionization increases, the distribution is peaked at energies greater than the arc voltage, and the location of the peak shifts towards lower energies as the arc current increases [26]. As the arc current increases, the proportion of singly charged ions also increases, as shown in Table 1.1. The ions are predominantly singly charged for low-melting-point metals, while for refractory metals, charge states as high as 5+ and 6+ may be observed.

1.1.4. Micro-Droplets

Along with the intense plasma flux that is generated at the cathode spots, there is also a component of cathode debris in the form of micro-droplets, sometimes referred to as macro-particles because they are macroscopic compared with the plasma particles. These metallic globules are ejected from the cathode in the molten state and rapidly solidify in flight. The emission of micro-droplets by cathodic arcs is a concern in the deposition of thin films, because it is micro-droplets that become macro-particles in the deposited film. The presence of macro-particles in the deposited films has inhibited a more widespread application of the CAPD method.

Micro-droplets are typically in the range of 0.10-10 μm in diameter. The size and population of micro droplets can be affected by the choice of cathode material, adjustments to the operation of the system, and designs of the sources that reduce or eliminate them. Once the cathode material is selected, the number and size of micro-droplets is influenced by cathode-substrate geometry, arc current, magnetic field, gas species, and pressure. Lowering the level of arc current reduces the size and concentration of micro-droplets emitted. Higher pressures of reactive gases reduce the number of micro-droplets in reactive deposition processes because, it is believed, reaction on the target surface forms a compound surface film. The presence of such a film on the surface of the target leads to reduced melting [15].

The spatial and size distribution of micro-droplets emitted shows that the population of particles decreases with increasing size. It was noted that the distribution of neutral atoms supported the argument that the source of the neutrals was evaporation from hot micro-droplets [27]. The emission is heaviest from low-melting-point materials and from slow moving arcs.

It has been noted that the ratio of volumes carried by the particles and the vapor depended strongly on the cathode material. The percentage of the volume transported by micro-droplets for Mg, Au, and Pd was found to be 80%, 50%, and 10%, respectively – that is, the percentage decreased with an increasing melting-point temperature of the cathode material [28].

It has been confirmed that ions and molten particles dominated the mass flow and there is also a natural separation of the macro-particles from the plasma. Ions were emitted mainly in the forward direction, predominantly in a direction perpendicular to the plane of the cathode. Micro-droplets were emitted mainly in the plane of the cathode at low angles (0^{o} to 30^{o}) [15, 29]. The choice of coating-system geometry therefore influences the concentration of macro-particles on the substrate.

1.1.5. Elimination of Macro-Particles

The number and size of macro-particles can be reduced by the proper selection of operating conditions; but they cannot be completely eliminated by these means. A method of eliminating micro-droplets involves the use of a diffuse arc [30] in which the discharge extends over the surface of the target and the target is in a molten state. No micro-droplets are emitted in this operating mode [31]. Other alternatives include electrostatic/magnetic ion optics to separate the ions from the micro-droplets and hence a particle-free coating, low-angle emission shielding, and increased arc spot velocity induced by an applied magnetic field.

A method for eliminating macro-particles has been described by using a plasma optic system to deflect the path of the ions in the emission flux. The plasma optic consisted of a curved metal tube having a longitudinal magnetic field of several hundred

oersteds and a radial electric field of tens of volts. It was demonstrated, by studying the deposited films that the ions could be successfully separated from the macro-particles and that macro-free coatings could be produced [32, 33]. Measurements of the radial ion-current density profile at the exit of the plasma optic system indicated a high degree of ion focusing along the axis of the system. Since the paths of neutral atoms and micro-droplets are unaffected by the magnetic and electric fields, they followed linear paths and were collected on the inner surface of the curved duct. Another design to eliminate macro-particles and minimize plasma loss by utilizing magnetic guiding has been developed [34]. The filtered CAPD system uses a 'twist' filter which is a 3-dimensional S-shaped coiled tube, see Figure 1.2. It efficiently filters out macro-particles while optimizing plasma throughput from the traditional 10-25% to over 50%. The ratio of the ion current that can be extracted from the filtered plasma, to the plasma producing current is reported as high as 7%, compared to the traditional 1-3%.

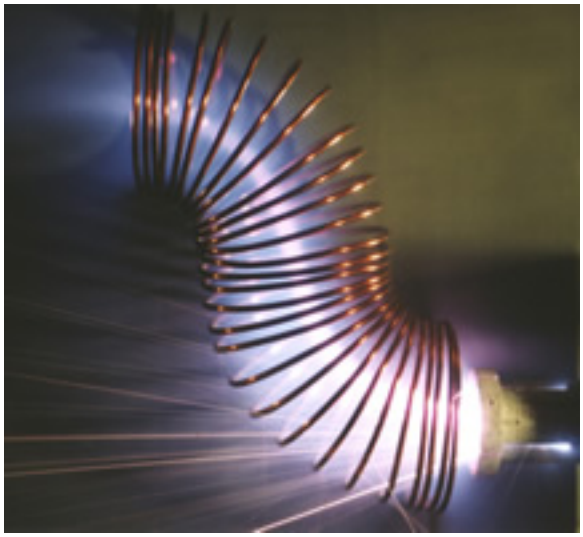

Figure 1.2. Cathodic arc plasma system with a twist filter for macro-particle removal. Reprinted from A. Anders, et. al. U.S. Patent #6,465,780 (2002).

Removal or reduction of macro-particles from the plasma by passing the plasma stream through a magnetic duct macro-particle filter is becoming a common procedure. Macro-particle contamination of the cathodic arc plasma is for most applications a disadvantage and for some a fatal defect. Applications such as decorative coatings, removal of macro-particles is unnecessary and is not done [15].

The method of removing micro-droplets from the deposition flux by passing the plasma through a duct is somewhat cumbersome for application in commercial deposition equipment. Simpler approaches have been implemented and have proven to be extremely effective. Practical and presently implemented methods of reducing the number of particles which reach the substrate include the following:

1) Low-angle shielding to block the flux of micro-droplets and stop them reaching the substrate;
2) Increasing the velocity of the cathode spot by magnetic means to reduce the mean residence time of the spot at any one point and reduce the volume of material that is melted and explosively emitted from the crater;
3) Reduction of the arc current, because micro-droplet emission is directly related to arc current, and;
4) Adjustment of gas pressure in reactive processes; selection of the optimum reactive gas pressure during deposition can reduce the number and size of macro-particles.

1.1.6. Arc Triggering

Triggering of arcs is an important concern. Special means are usually required to initiate an arc discharge and can be created using different triggering mechanisms [35,

36]. Depending on the parameters and operational mode of the source involved, triggering can be done electronically, electromechanically, or purely mechanically, and it can be initiated by laser, gas-breakdown, or surface breakdown [15, 37-41].

All triggering mechanisms have in common that they produce initial plasma at one of the electrodes. The arc is established when the initial plasma bridges between the cathode and the anode allowing a high current to flow at a relatively low voltage. The arc is maintained when the supply circuit is capable of delivering a current greater than the 'chopping' current, a material-dependent critical minimum current which is associated with the minimum metal plasma production [13].

The advantages and disadvantages of triggering methods are listed in Table 1.2. The most frequently used approach is high-voltage surface flashover through edge triggering because it is relatively easy to achieve as well as being simple to manufacture [13]. In this mode, the plasma is established by a high-voltage surface flashover between the cathode material and trigger electrode across an insulator. This type of trigger can fail due to excessive deposition of cathode material onto the insulator, creating a short between the cathode and trigger electrode [35].

Another commonly used method of igniting an arc in a CAPD system is to make momentary contact to the target surface with a contactor. This method is very reliable, provided a molybdenum contactor is used. As the surface temperature of the target increases, the possibility of the contactor becoming welded to the target also increases; this possibility is avoided by the use of molybdenum.

Alternative contact-less igniters have also been used. One of them is the so-called gas injection triggering, which admits a burst of gas to the chamber to elevate the pressure while simultaneously applying a high-voltage spike to the igniter electrode. RF

ignition may also be used. These techniques have an advantage in that they have no moving parts inside the vacuum, and also do not produce a burst of micro-droplets as in the cases with the contacting striker [42, 43].

Triggering Mechanisms	Advantages	Disavantages
High-voltage vacuum breakdown	No contamination of metal plasma	Requires a high voltage; breakdown voltage changes with electrode conditioning
Fuse wire explosion	No contamination of metal plasma	Not usable for repetitive mode operation
Contact separation	Reliable, simple, repeatable	low repetition rate; contacts may weld
Mechanical triggering	Reliable, simple, repeatable (depending on mechanism)	low repetition rate; contacts may weld and wear; limited number of triggering events ($< 10^4$); large jitter
High-voltage surface discharge	High repetition rates, reliable typically up to 10^5 pulses, low jitter	Needs high-voltage pulser; fails when approching 10^6 pulses; plasma contamination by erosion of insulator
Plasma injection triggering	Moderate to high repetition rates, small jitter	Needs high-voltage pulser; works only with suffucuently strong triggering discharge
Gas injection triggering	No trigger supply	Needs sufficiently high pressure in the discharge vicinity; metal plasma contamination by gas species; very large jitter
ExB gas discharge triggering	Reliable for more than 10^6 pulses, small jittter, gas load negligible for most applications	Requires special electrodes, magnetic coil arrangement and additional power supplies for gas discharge and magnetic field
Laser plasma triggering	Reliable, trigger location controllable, very small jitter	Expensive; needs sustainable optical access to cathode; minimum power density 10^{11} Wm^{-2}
Low-voltage vacuum arc initiation	Reliable for more than 10^6 pulses, simple, high repetition rate possible, works without high voltage	Needs arc switch and moderate 'booster' voltage; may fail for low-melting-point and easily oxidizing cathode materials

Table 1.2. An overview of vacuum arc triggering. Reprinted from A. Anders, *et. al.*, *J. Phys. D: Appl. Phys.* **31** pp. 584-587 (1998).

1.1.7. Summary

The acceptance of CAPD technology is somewhat limited throughout the film deposition industry. There are numerous ways of controlling and manipulating the plasma and the research and development continues to advance. The cathodic arc plasma deposition technique is characterized by having:

1) a high percentage of ionization of the emitted vapor, 30-100%;
2) emission of multiply charged ions, and;
3) a high kinetic energy of the emitted ions, 10-100 eV.

These characteristics of CAPD provide the following benefits in film quality and process control:

1) high film adhesion and density;
2) high deposition rates with excellent coating uniformity;
3) high-quality, stoichiometric reacted coatings;
4) low substrate temperatures during deposition, and;
5) retention of alloy composition from the target to the deposited film.

The presence of macro-particles in the plasma stream is a disadvantage of the CAPD technique. This requires the need for a simple and high-efficiency macro-particle filter system and process controls.

1.2. Overview

The intention of the research project presented in this thesis was to develop a thin film deposition technique that could provide high-growth rate and large area coverage. These characteristics are in comparison to films deposited by single laser PLD.

The organization of this thesis is as follows. The second chapter is a characterization of the laser-triggered hollow-electrode transient plasma discharge system through investigations of the discharge reliability of the PFN, cathode corrosion and characterization of the PFN. The third chapter discusses the material source and film growth of the transient plasma. The fourth chapter discusses the high-voltage triggered hollow-electrode plasma discharge system for thin film growth through characterization of the glow discharge and of the films deposited. The thesis is concluded in the fifth chapter with a presentation of the findings in this thesis as well as related future work.

CHAPTER 2. LASER-TRIGGERED HOLLOW-ELECTRODE PULSED PLASMA DISCHARGE SYSTEM FOR THIN FILM GROWTH

This chapter serves as a description of the experimental apparatus and the mechanism of the laser-triggered hollow-electrode transient plasma process. The motivation for the project is discussed in detail through an investigation of the discharge reliability, corrosion of the cathode, and characterization of the process parameters.

2.1. System Description

This section of the chapter serves as a detailed description of the components of the experimental apparatus. The laser-triggered hollow-electrode transient plasma discharge system primarily consists of a discharge head, a pulse forming network (PFN), a pulsed 10.6 μm CO_2 laser, and a vacuum chamber.

2.1.1. Hollow-Electrode Discharge Head

A cross-sectional detailed diagram of the hollow-electrode discharge head is shown in Figure 2.1. A Pyrex T-tube was constructed to be used as an electrical insulator between the electrodes, a structural support for the electrodes and a delivery path for flowing gas between the electrodes of the discharge head at a predetermined flow rate. The hollow-electrode and rod-electrode of the discharge head are both made of conductive materials. The dimensions of the hollow-electrode are 14.2 mm outside diameter, 11.7 mm inside diameter and 14.8 mm in length. This electrode is firmly

pressure-fitted to the outside of the Pyrex T-tube allowing 7.5 mm of the inside length exposed to the rod electrode. The dimensions of the rod-electrode are 6.25 mm in diameter and approximately 9 cm in length. This electrode is firmly pressure fitted with a Teflon bushing to the inside of the Pyrex T-tube to be coaxial to the hollow-electrode. Electrical leads required thermal and electrical insulation to minimize arcing during the discharge. A positively biased, high voltage (200-1500 VDC), low current (10 mA) ring electrode 8 centimeters in diameter is placed around the Pyrex T-tube. This ring electrode is constructed of 1.5 mm diameter copper wire. The ring electrode is provided in order to 'pre-ionize' the background gas without causing a luminous glow discharge. The pre-ionized gas between the positive ring electrode and electrical ground gives rise to an electron energy and number density which is maintained low enough to prevent the generation of visible light by excitation collisions until initiated by the triggering laser. In a low-pressure glow discharge a negative space charge region with high electron density is formed near the negative electrode, the cathode of the discharge head.

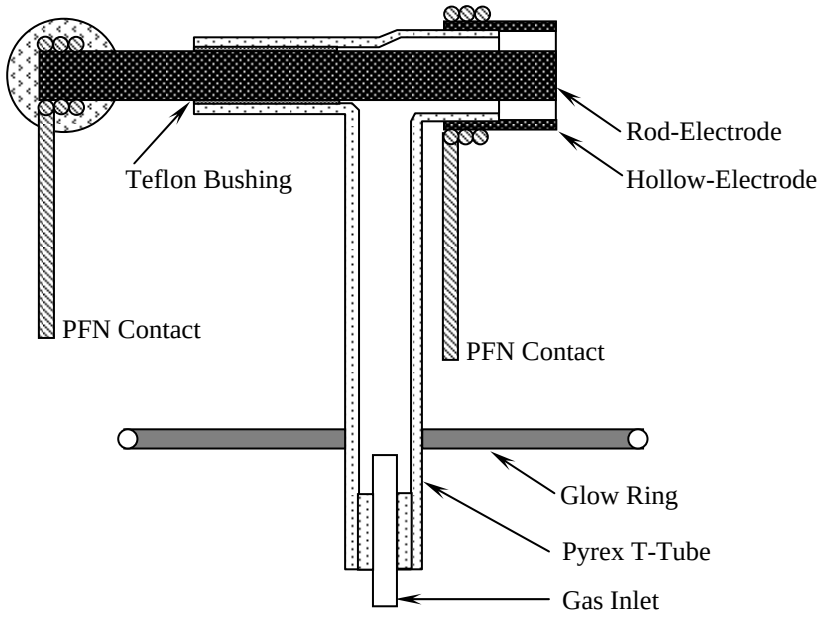

Figure 2.1. Cross-sectional detail of a hollow-electrode discharge head.

2.1.2. Pulse Forming Network

The pulse forming network (PFN) used in the experiments reported here is shown in Figure 2.2. It consists of a power supply, resistor, capacitor bank, and inductor. The discharge head electrodes (see Figure 2.1.) are connected across the positively grounded PFN. The PFN capacitor bank is charged to the desired voltage (V_s) by a low voltage, 0-150V, high current, 0-18A, DC power supply. An air cooled variable power resistor (R) is in series with the power supply (V_s) to limit the circuit current (i) and thus, control the charging time of the capacitor bank (see Figure 2.3.(a.) and (b.)).

$$i = \left(\frac{V_s}{R}\right) e^{-\frac{t}{RC}} \qquad [1.1]$$

This PFN was able to produce current pulses up to 3300 amperes with the FWHM exceeding one millisecond. To generate current pulses in this range, a capacitor stage of 39 mF in the PFN was charged to 100 volts and allowed to discharge through an inductor of 53.2 μH to obtain the required current pulse. Operating the PFN in this range at 1 Hz required cooling of the PFN components to dissipate the heat produced by the 3.6 watts of power, as measured by the area under the IV curve of Figure 2.3.(c.).

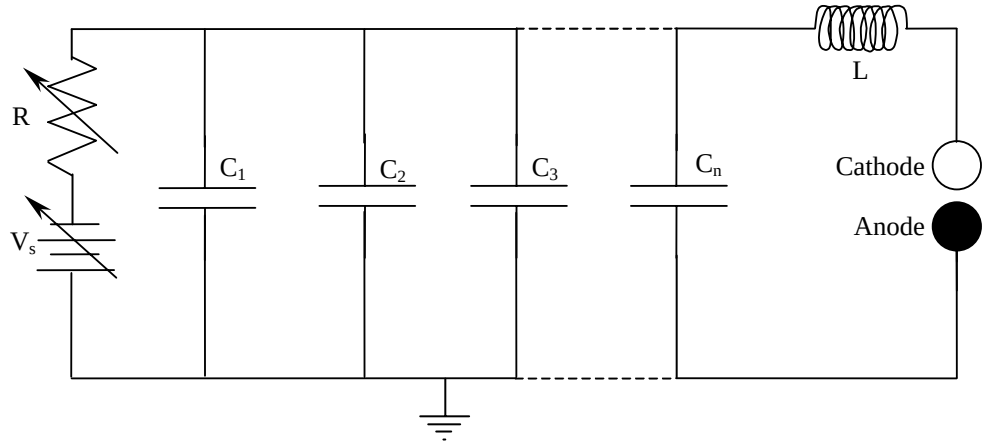

Figure 2.2. The pulse forming network used in the experiments.

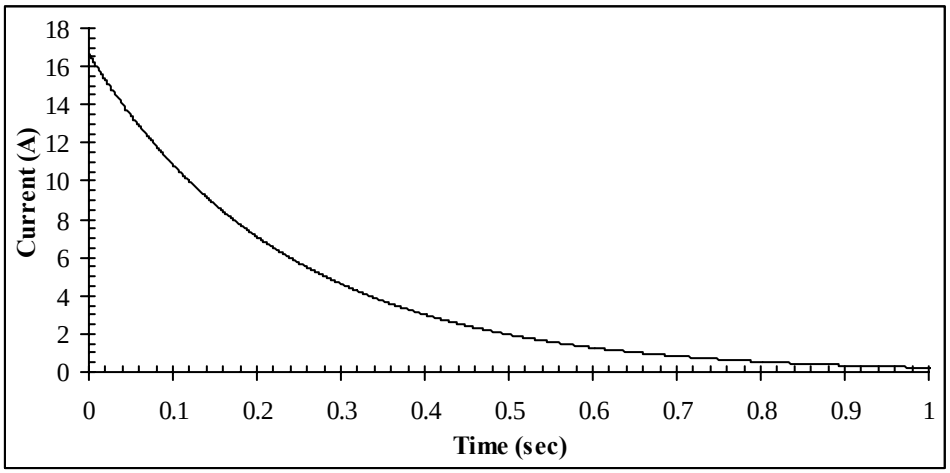

(a)

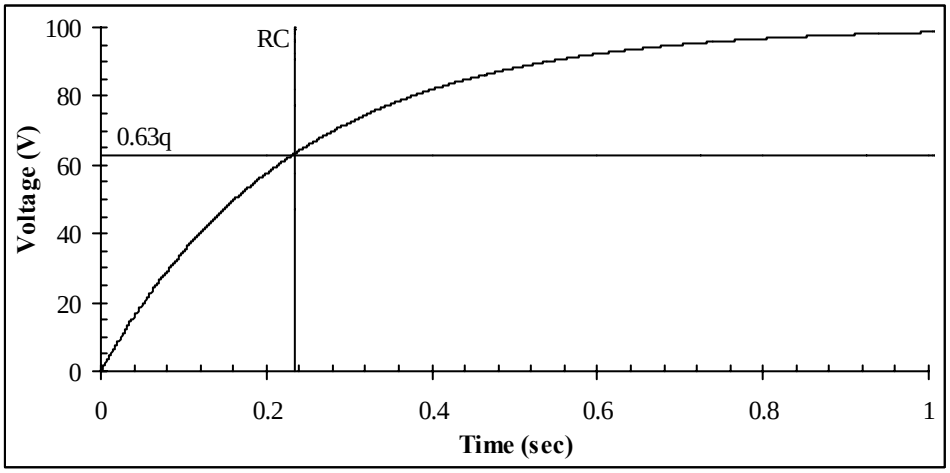

(b)

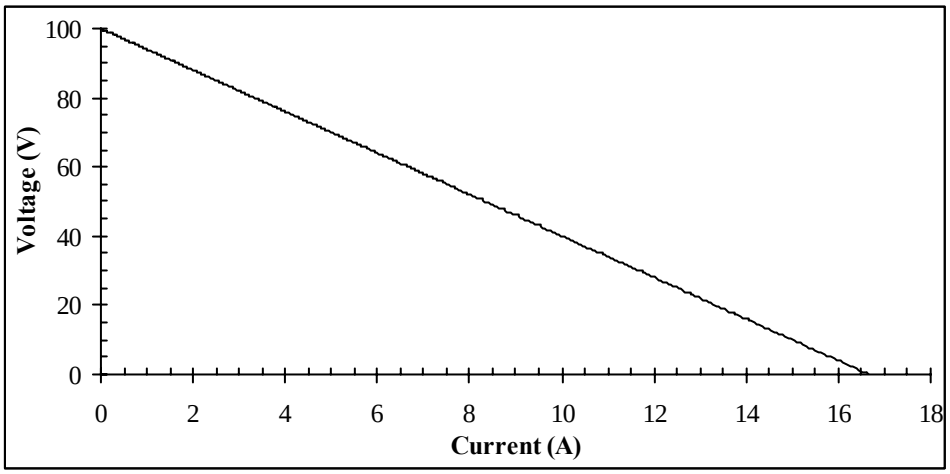

(c)

Figure 2.3. Charging of the PFN, (a) current as a function of time, (b) voltage as a function of time, and (c) voltage as a function of current.

2.1.3. Triggering Laser

Laser pulses from a TEA CO_2 laser at a wavelength of 10.6 μm are directed through a 1.5 inch diameter, 20 inch focal length, plano-convex ZnSe lens and ZnSe window to impinge on the outer surface of the cathode to trigger the transient plasma discharge. Triggering of the PFN requires a sufficient electron density at the cathode. The density of these electrons, in conjunction with the thermionic electrons generated due to rapid heating of a spot on the cathode by the incident CO_2 laser pulse, is sufficient to trigger the plasma arc. Thermionic emission is the mechanism by which electrons are set free from the metal structure of the cathode. By rapidly heating the cathode the electrons are given enough energy to break the bond holding them in the metal. If there were no voltage applied to the electrodes the electrons would just form a cloud around the cathode. The application of the voltage causes the electrons to stream away from the cathode in a ray or beam. The electrons that leave the cathode must eventually be replaced from the power supply. Emission of electrons or ions from substances that are highly heated, produce charged particles called thermions. The number of thermions being emitted increases rapidly as the temperature of the substance rises. If the heated body carries a positive or negative charge, the thermions will be of the same charge. The high current ion beam from the anode to the cathode causes sputtering of the cathode material by positive ions. The high gas pressure inside the hollow-electrode leads to a rapid expansion of the plasma plume to propagate toward the grounded substrate holder.

2.1.4. Vacuum System

A mechanical roughing pump in series with a turbo molecular pump is used to evacuate the vacuum chamber. A 43.2 cm diameter by 73.7 cm high, 0.1 m^3, stainless

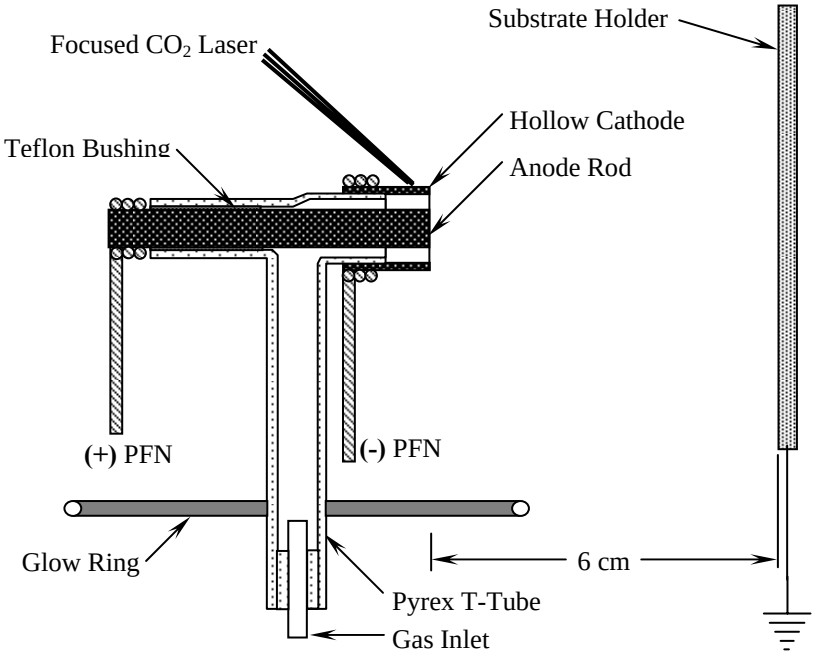

Figure 2.4. Cross-sectional detail of the hollow-cathode discharge head.

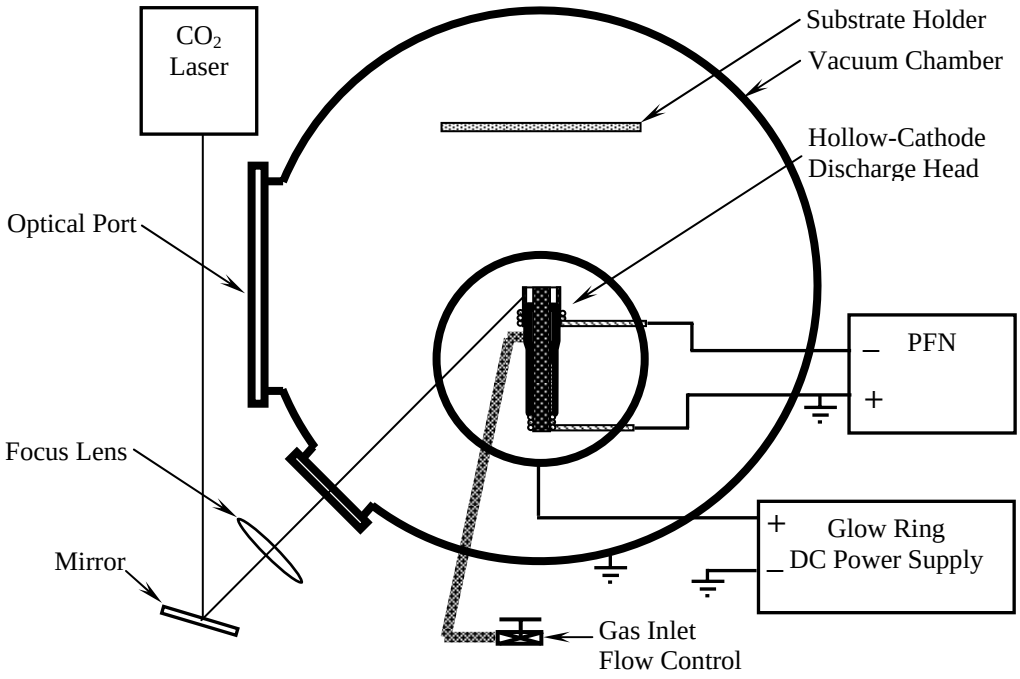

Figure 2.5. Schematic of the laser-triggered hollow-cathode plasma discharge system.

steel vacuum chamber, with Viton seals was used. A cold cathode gauge is used to measure the background pressure and a thermocouple gauge is used to monitor the ambient pressure. The discharge head is positioned in the vacuum chamber with line of sight to, the cathode for the triggering laser, and to the plasma discharge for a 6 inch optical diagnostics port. A movable shield is provided to protect the optical port when not used for diagnostics. A provision for controlled flow of gas into the discharge head was provided.

Various configurations of the discharge head of Figure 2.1. were used in the experiments. In this section a hollow-cathode discharge head, shown in Figure 2.4., and a hollow-anode discharge head, shown in Figure 2.6., were used. The triggering laser impinges on the hollow-electrode of the hollow-cathode system and on the rod-electrode of the hollow-anode system. Top view schematics of the laser triggered hollow-cathode and hollow-anode plasma discharge systems are shown in Figures 2.5. and 2.7. respectively.

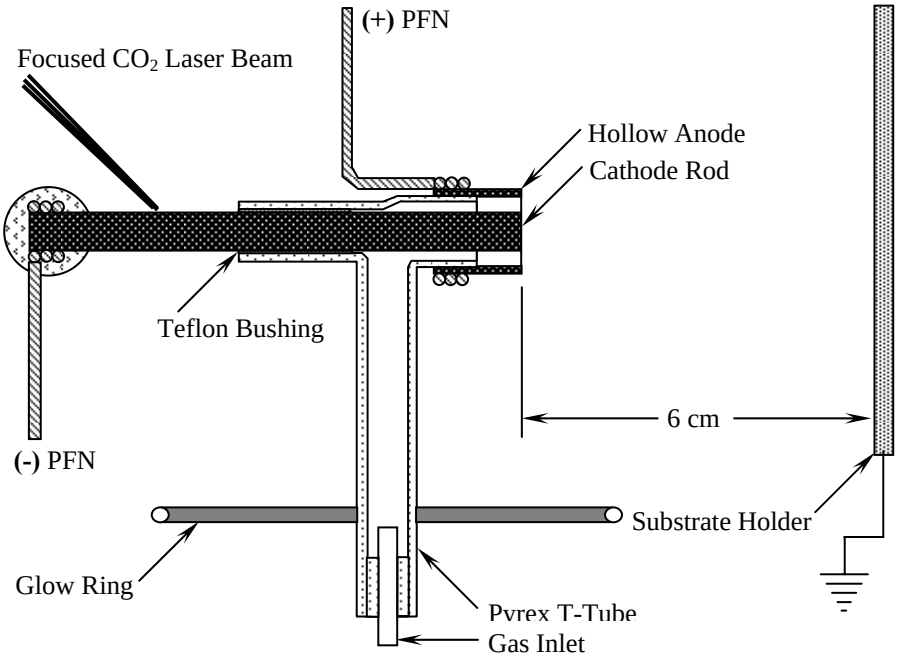

Figure 2.6. Cross-sectional detail of the hollow-anode discharge head.

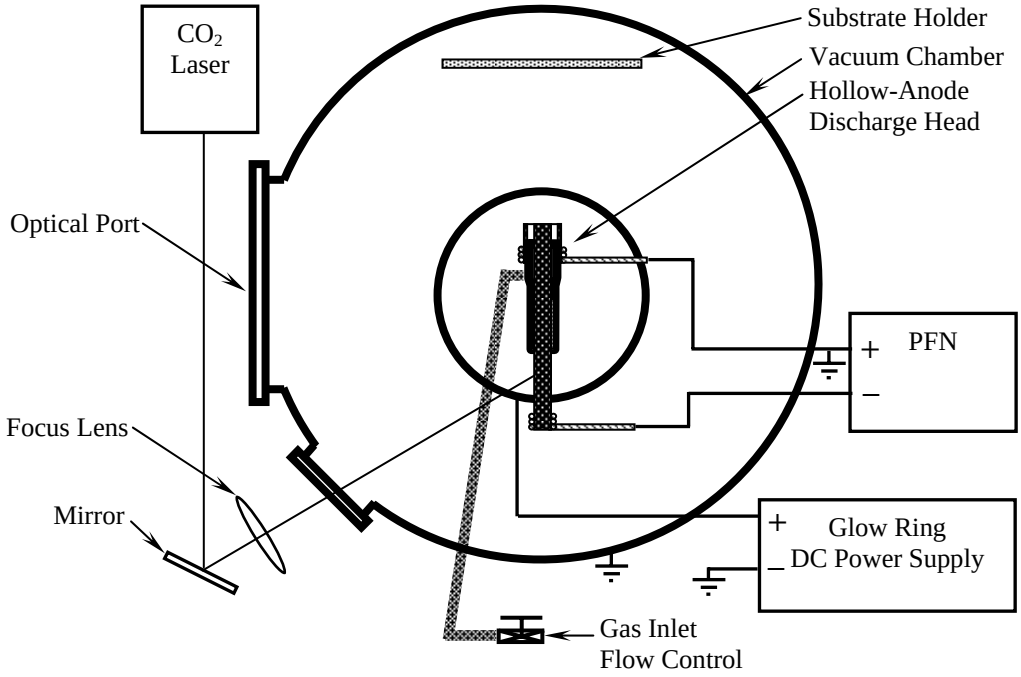

Figure 2.7. Schematic of the laser-triggered hollow-anode plasma discharge system.

2.2. Discharge Reliability of the Pulse Forming Network

The PFN did not produce a discharge each time the cathode was struck by the triggering CO_2 laser pulse, thereby reducing the discharge reliability of the PFN and limiting the ability to properly characterize the system. This section describes the experimental studies carried out to determine the process parameters which affect the discharge reliability of the PFN. During occurrences of PFN non-discharge it was noted that the incident laser pulse caused ablation of the cathode surface. This ablation could lead to corrosion of the cathode material and contamination of the system and deposited film. Therefore, it is important to characterize the conditions of discharge reliability of the PFN to reduce these effects. Preliminary studies have shown that the discharge reliability is dependent on the incident laser fluence, laser modes, gas pressure and type, and the electrode configuration.

2.2.1. Experimental Setup

The initial experiments were conducted using the hollow-cathode configuration, as shown in Figures 2.4. and 2.5. The PFN was operated at an initial voltage of 70V with an inductance of 53.2 μH and a total capacitance of 34 mF. A commercial inductive pick-up coil was placed symmetrically around the lead connecting the hollow-cathode to the PFN. The pick-up coil was connected to a 1GHz oscilloscope through a 50Ω terminator for recording the induced voltage pulse from the discharging PFN. Based on preliminary experiments, the vacuum chamber was evacuated and back filled with nitrogen to a pressure of 12 millitorr. The CO_2 laser was operated at 1Hz and the area of the laser spot size was varied by moving the focusing lens position, forming various spot sizes at the

surface of the cathode in the range of 1.2 mm^2 to 13.7 mm^2. The spots were elliptical in shape at the target surface.

Errors are shown by plus/minus one standard deviation calculated by;

$$S.D. = \sqrt{\frac{\sum \left(x - \bar{x}\right)^2}{n-1}} \qquad [2.1]$$

Standard deviation is a measure of how widely values are dispersed from the average (mean) calculated using the 'unbiased' or *n*-1 method. The sample mean average is $\bar{x}$, and the sample size is *n*. Trend lines are fitted by regression analysis when displayed in graphs.

2.2.2. Reliability Dependence on the Discharge Duty Cycle

An increase in non-discharges as the number of total laser shots increased was initially suspected to be due to increasing temperature of the discharge head during the experimental run as a result of the duty cycle. A crude initial trial was conducted for a total of 600 laser shots at CO_2 laser energy of 145.8 mJ ± 5.3 mJ and a spot size of 10.6 mm^2 at a rate of 1 Hz, giving a laser fluence of 13.7 ± 0.5 mJ/mm^2. This laser spot size was chosen from preliminary studies because it was the size with the lowest recorded number of PFN non-discharges, so it would have the highest number of discharges leading to the greatest possible heat accumulation. One trial was conducted at continuous duty for a total of 600 laser shots recording the number of non-discharges for each of six 100 shot intervals. A second trial was then conducted where 100 laser shots were conducted followed by 15 minutes for the discharge head temperature to reduce by radiation and/or conduction while still in vacuum (12 millitorr of nitrogen), and successive replications of the 100 shot exposures until a total of 600 shots had been

completed. The results are shown in Figure 2.8. Both trials increased at nearly the same rate of non-discharges implying that the increase in non-discharges is not due to the rise in the temperature of the discharge head during a run.

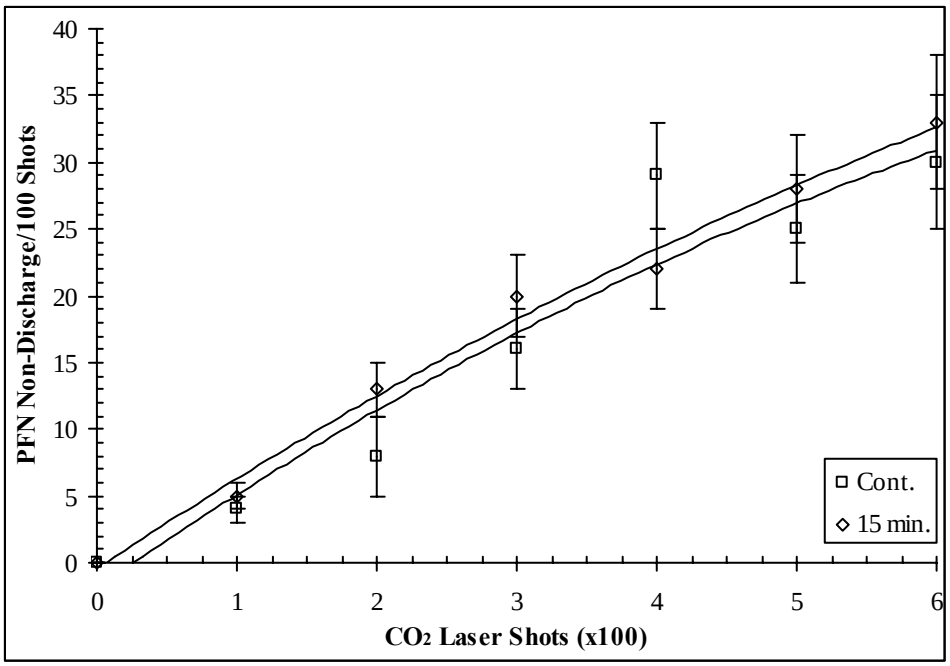

Figure 2.8. PFN non-discharges as a function of the number of CO_2 laser shots at continuous duty and 100 shots at 15 minute intervals.

2.2.3. Reliability Dependence on the CO_2 Laser Characteristics

It was observed that the discharge reliability of the pulse forming network is dependent on characteristics of the triggering CO_2 laser. Investigations were performed varying the triggering laser spot size, and energy to control the laser fluence. These investigations were also conducted using lasers with various modes.

2.2.3.1. Reliability Dependence on Laser Fluence

The discharge reliability dependence on the laser fluence was initially studied by varying the spot size of the incident laser pulse. Scale representations, of the elliptical

CO_2 laser spot sizes and the area of the spot sizes used in the experiment, are shown in Figure 2.9. The incident laser spot size was measured by striking graphite paper at the impinging site of the laser pulse on the cathode. The laser pulse ablates the graphite from the paper and the dimensions of the resulting elliptical spot are measured and the area of the spot is calculated by equation 2.2. The CO_2 laser was operated with a pulse energy of 193.0 mJ ± 5.2 mJ.

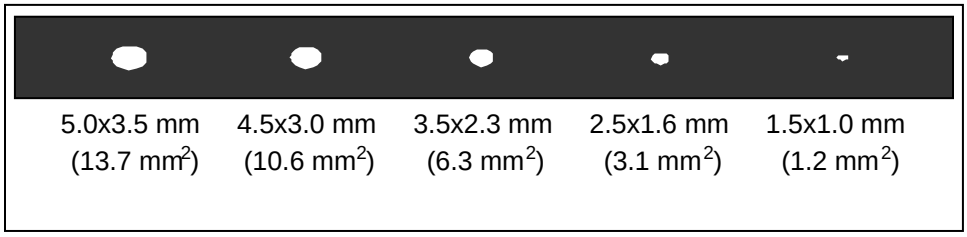

Figure 2.9. Scale representation of the CO_2 laser spot sizes.

$$A_s = ab\pi \qquad [2.2]$$

The results for the PFN non-discharges per 100 shots for a total of 500 shots as a function of CO_2 laser shots are shown in Figure 2.10. It was found that as the total number of laser shots increased, the percentage of PFN non-discharges increased non-linearly. It was also found that as the area of the spot size increased from 1.2 mm^2 to 10.6 mm^2, the average number of PFN non-discharges decreased, but from 10.6 mm^2 to 13.7 mm^2 the average number of PFN non-discharges increased dramatically, as shown in Figure 2.11. The average number of PFN non-discharges was also plotted as a function of the CO_2 laser fluence, the laser energy per unit area, as shown in Figure 2.12.

Triggering of the PFN requires a sufficient electron density at the cathode in order for current to flow from the anode to the cathode. The density of the electrons provided

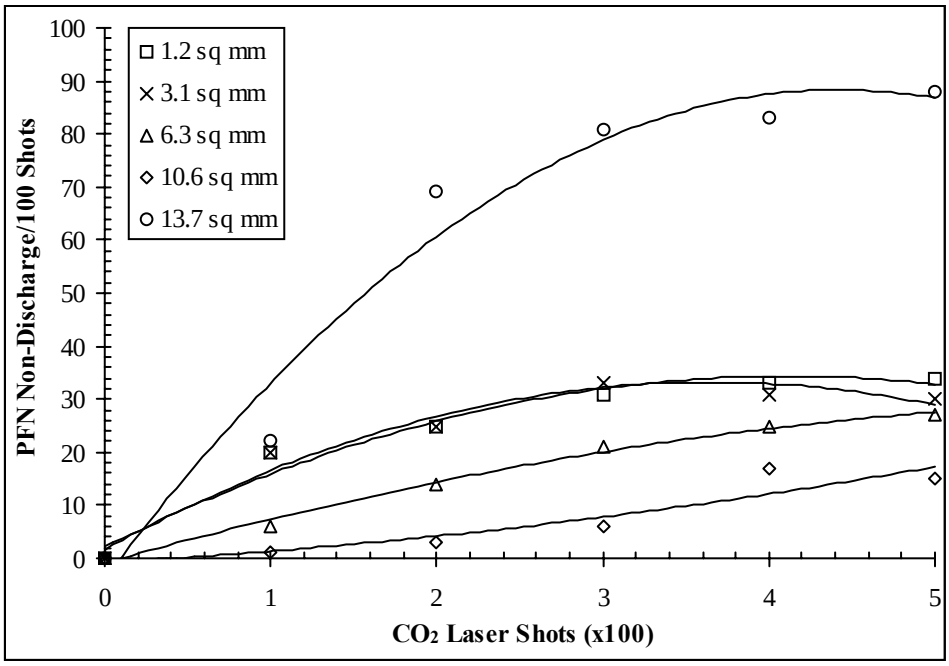

Figure 2.10. PFN non-discharges as a function of CO_2 laser shots for various laser spot sizes at a laser energy of 193.0 mJ ± 5.2 mJ.

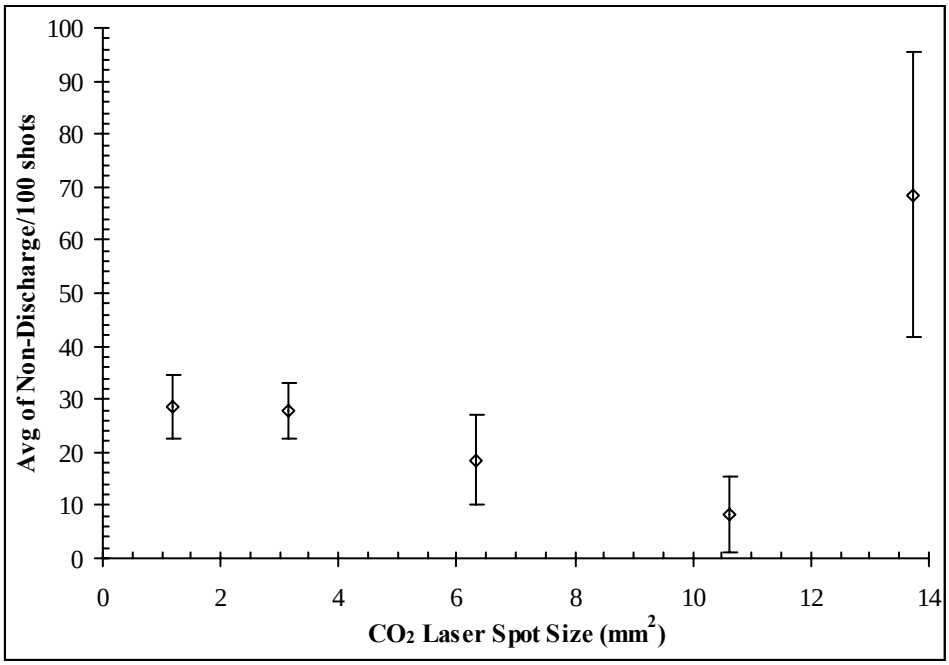

Figure 2.11. Average number of PFN non-discharges as a function of CO_2 laser spot size at laser energy of 193.0 mJ ± 5.2 mJ.

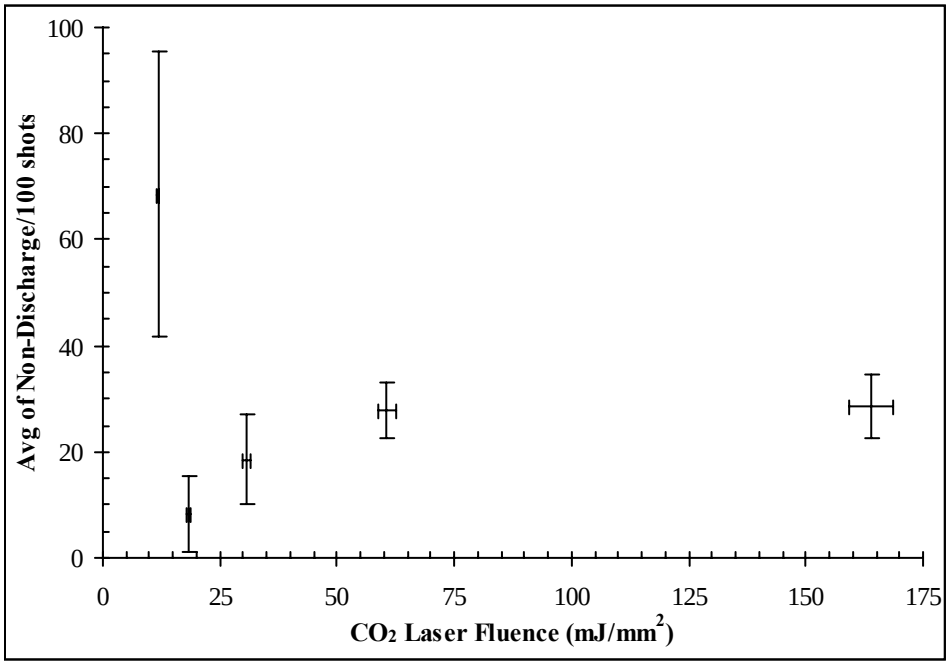

Figure 2.12. Average number of PFN non-discharges as a function of the CO_2 laser fluence at laser energy of 193.0 mJ ± 5.2 mJ.

by the pre-ionizing ring electrode, in conjunction with the thermionic electrons generated due to rapid heating of a spot on the cathode by the incident CO_2 laser pulse, is the mechanism to trigger the plasma arc. PFN non-discharges may be due to a low electron density. The increase in the non-discharges as the number of lasers shots increased may be due to a structural change of the surface of the cathode at the site of the impinging laser strike affecting the absorption of the laser energy.

2.2.3.2. Reliability Dependence on Laser Modes

The CO_2 laser used in the previous experiments was found to have multiple spatial modes (intensity distributions) and multiple longitudinal modes (wavelengths). A variety of mode configurations were investigated; multiple spatial modes with multiple longitudinal modes, single spatial mode with multiple longitudinal modes, and single spatial mode with single longitudinal mode. Three different lasers, each with one of the

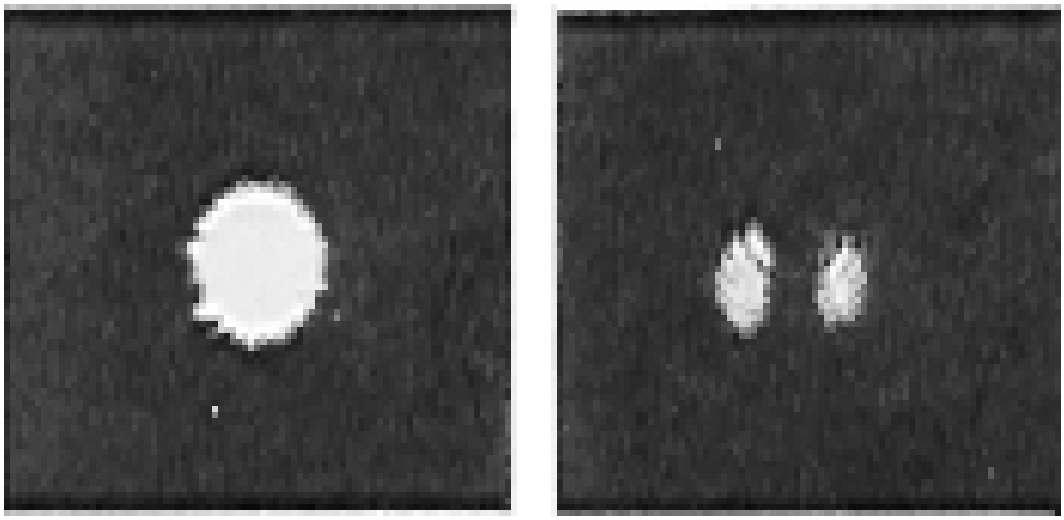

TEM 00 TEM 10

Figure 2.13. Examples of CO2 spatial modes, TEM 00 and TEM 10.

above mode characteristics were used to investigate the PFN discharge reliability. The lasers single or multiple spatial modes were determined by observing the intensity distributions of the laser output projected on a dark card. Examples of single spatial mode, TEM 00, and multiple spatial mode, TEM 10 are shown in Figure 2.13. Presence of longitudinal modes was determined by observing the laser output pulse signals using a pyro-electric detector. Multiple longitudinal modes in a laser pulse cause periodic intensity variations in time to appear on the recorded signal, as shown in the longitudinal mode detail in Figures 2.14(b) and (d). These laser modes were investigated as a function of laser spot size and laser fluence.

The laser energy was varied from 10 to 230 mJ depending on the capability of the given laser. It was observed that PFN non-discharges increased as the spot size increased and as the laser energy decreased, shown in Figure 2.15. Use of the single spatial mode with single longitudinal mode laser had the lowest occurrence of PFN non-discharges as the spot size and laser energy was varied, shown in Figure 2.15. (c). Use of the single

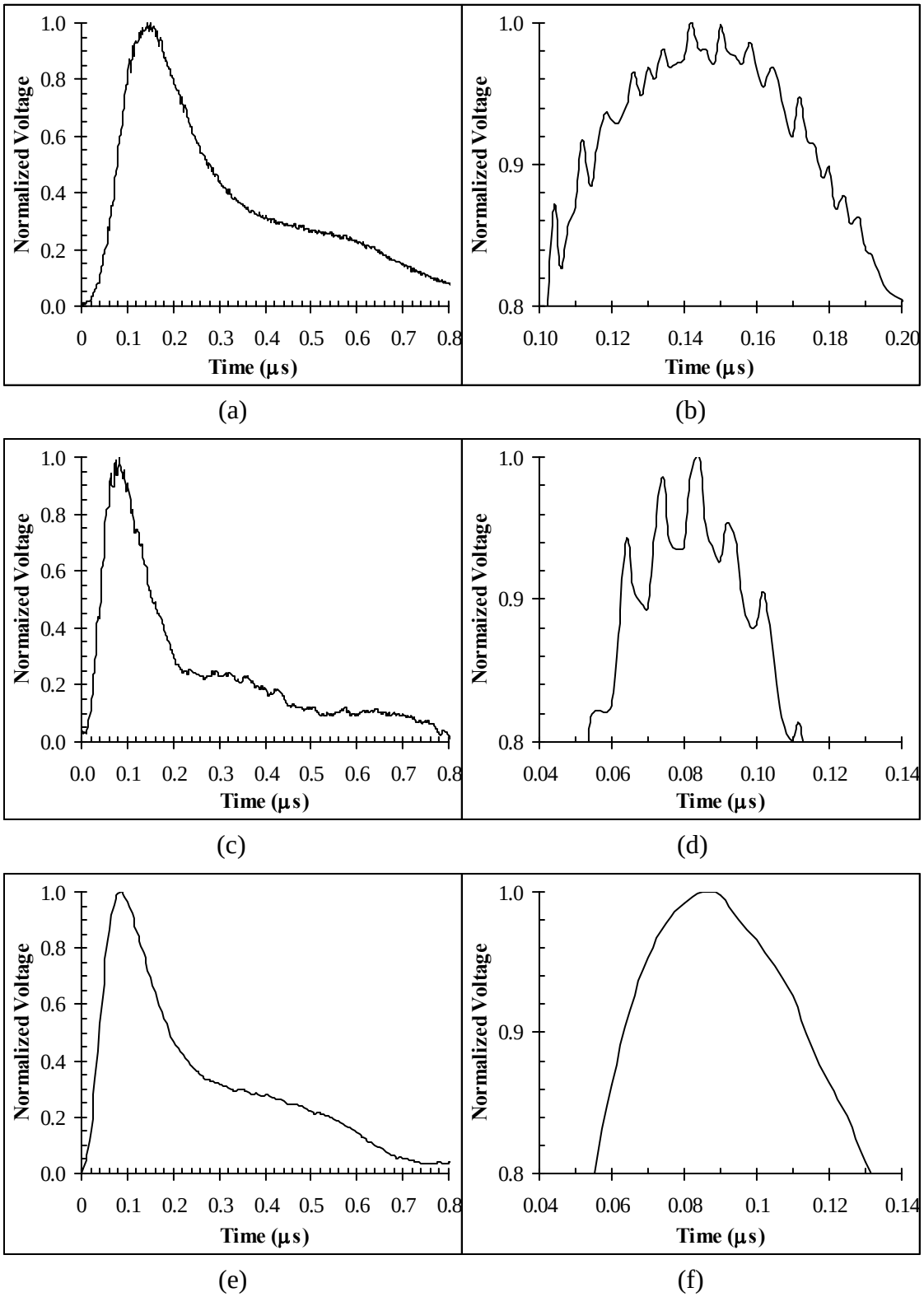

Figure 2.14. CO_2 laser pulses with a variety of longitudinal modes, (a) multi-mode with (b) longitudinal mode detail, (c) single-mode with (d) longitudinal mode detail, (e) single-mode laser with (f) no longitudinal mode.

spatial mode with multiple longitudinal modes laser had the highest occurrence of PFN non-discharges as the laser spot size and energy was varied, shown in Figure 2.15. (b). A variety of mode configurations were investigated; multiple spatial modes with multiple longitudinal modes, single spatial mode with multiple longitudinal modes, and single spatial mode with single longitudinal mode at different laser fluences. It was observed that PFN non-discharges increased as the laser fluence decreased for each laser mode configuration, shown in Figure 2.16. Use of the single spatial mode with single longitudinal mode laser had the lowest occurrence of PFN non-discharges as the laser fluence was decreased, shown in Figure 2.16 (c). Use of the single spatial mode with multiple longitudinal modes laser had the highest occurrence of PFN non-discharges as the laser fluence was decreased, shown in Figure 2.16 (b). The laser with multiple spatial modes with multiple longitudinal modes had the most variation on the PFN non-discharges as the laser fluence was varied.

The laser with single spatial mode and single longitudinal mode was then used to trigger the hollow-anode configuration, see Figure 2.7. The PFN non-discharge as a function of the CO_2 laser fluence for various laser spot sizes is shown in Figure 2.17. The non-discharges occur at higher laser fluence than for the same laser for the hollow-cathode configuration. This may be due to the greater distance between the site of the laser impinging on the rod-cathode and the discharge area between the electrodes, and not enough electrons being freed at lower laser fluences as compared to the hollow-cathode configuration.

A variety of mode configurations were investigated; multiple spatial modes with multiple longitudinal modes, single spatial mode with multiple longitudinal modes, and single spatial mode with single longitudinal mode at different laser fluences. It was

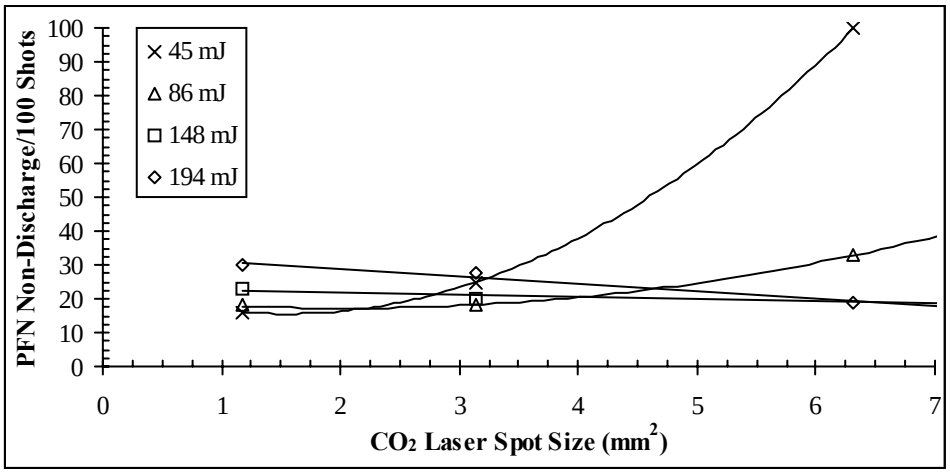

(a)

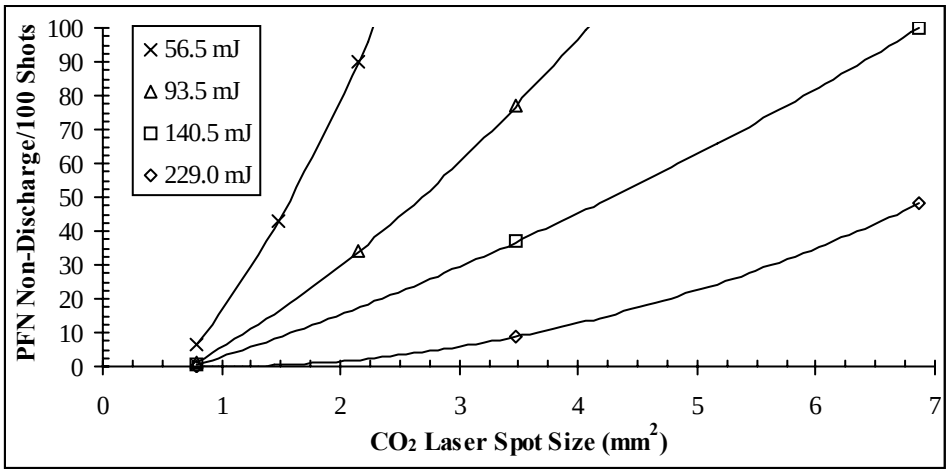

(b)

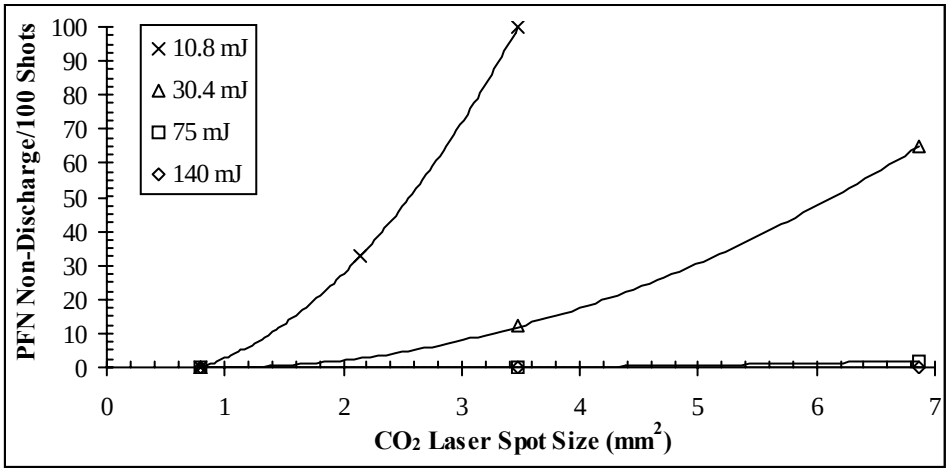

(c)

Figure 2.15. PFN non-discharges for various laser energies and (a) multi-mode with longitudinal modes, (b) single mode with longitudinal modes, and (c) single mode with no longitudinal modes.

observed that PFN non-discharges increased as the laser fluence decreased for each laser mode configuration, shown in Figure 2.16. Use of the single spatial mode with single longitudinal mode laser had the lowest occurrence of PFN non-discharges as the laser fluence was decreased, shown in Figure 2.16 (c). Use of the single spatial mode with multiple longitudinal modes laser had the highest occurrence of PFN non-discharges as the laser fluence was decreased, shown in Figure 2.16 (b). The laser with multiple spatial modes with multiple longitudinal modes had the most variation on the PFN non-discharges as the laser fluence was varied.

The laser with single spatial mode and single longitudinal mode was then used to trigger the hollow-anode configuration, see Figure 2.7. The PFN non-discharge as a function of the CO_2 laser fluence for various laser spot sizes is shown in Figure 2.17. The non-discharges occur at higher laser fluence than for the same laser for the hollow-cathode configuration. This may be due to the greater distance between the site of the laser impinging on the rod-cathode and the discharge area between the electrodes, and not enough electrons being freed at lower laser fluences as compared to the hollow-cathode configuration.

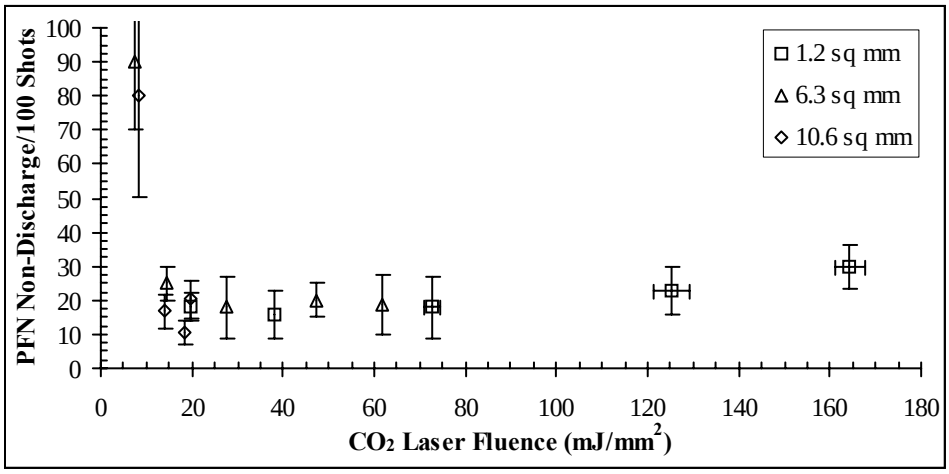

(a)

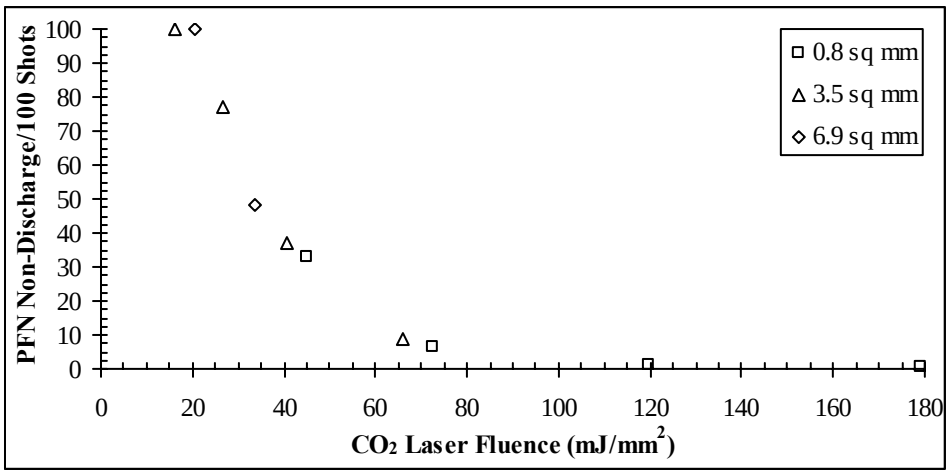

(b)

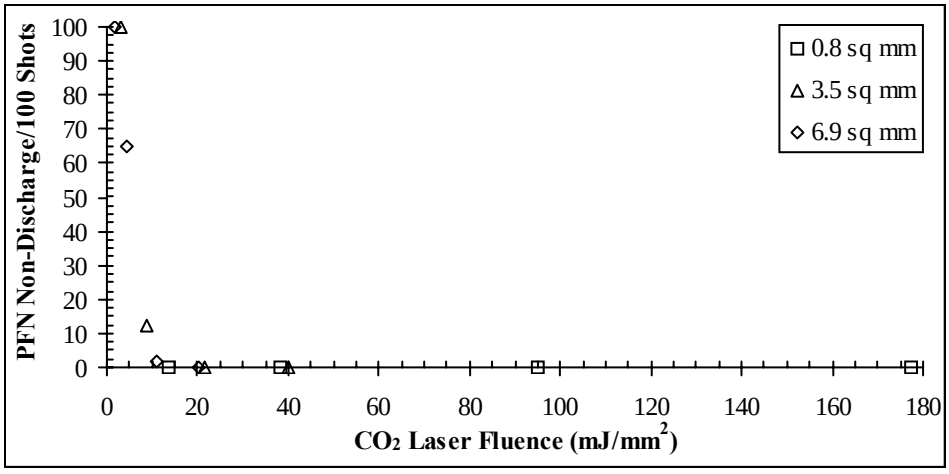

(c)

Figure 2.16. PFN non-discharges versus CO_2 laser fluence for various laser spot sizes and (a) multi-mode with longitudinal modes, (b) single mode with longitudinal modes, and (c) single mode with no longitudinal modes.

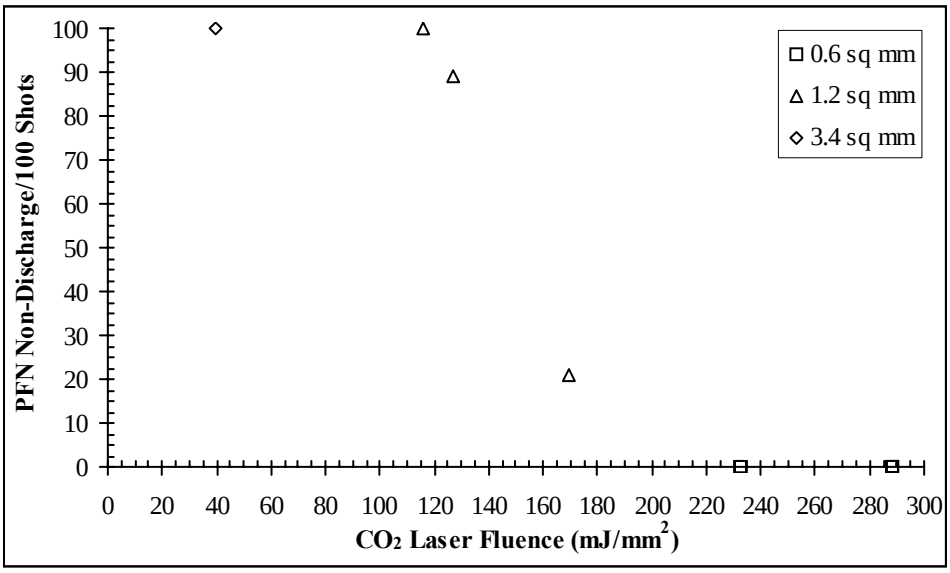

Figure 2.17. PFN non-discharges for various spot sizes for hollow anode.

2.2.4. Reliability Dependence on Ambient Gas Composition

The discharge reliability was found to be dependent on the vacuum pressure and ambient gas type, nitrogen or argon. As the pressure was decreased the occurrence of PFN non-discharges increased for both gas types, shown in Figure 2.18. PFN non-discharge begins to occur at 9 mTorr of nitrogen but as low as 1.5 mTorr for argon. Both gases have greater than 90 percent PFN non-discharges at pressures of 1 mTorr and lower. One hundred percent of triggered PFN discharges occurred at pressures greater than 10 mTorr of nitrogen and 2.5 mTorr of argon.

The relationship between gauge pressures with an ambient of nitrogen as a function of gauge pressure of argon, shown in Figure 2.19. The thermocouple gauge is calibrated for air and nitrogen, so the relationship to argon pressure was measured. A nitrogen gas regulator was set for 3 psi back-pressure, and a needle valve was set to the desired pressure, the regulator and needle valve were then moved to the argon cylinder

and the resulting gauge pressure was recorded. This was repeated for various nitrogen and argon pressures as shown in Figure 2.19. The adjusted argon gauge pressure is also represented as Argon (N2) in Figure 2.18.

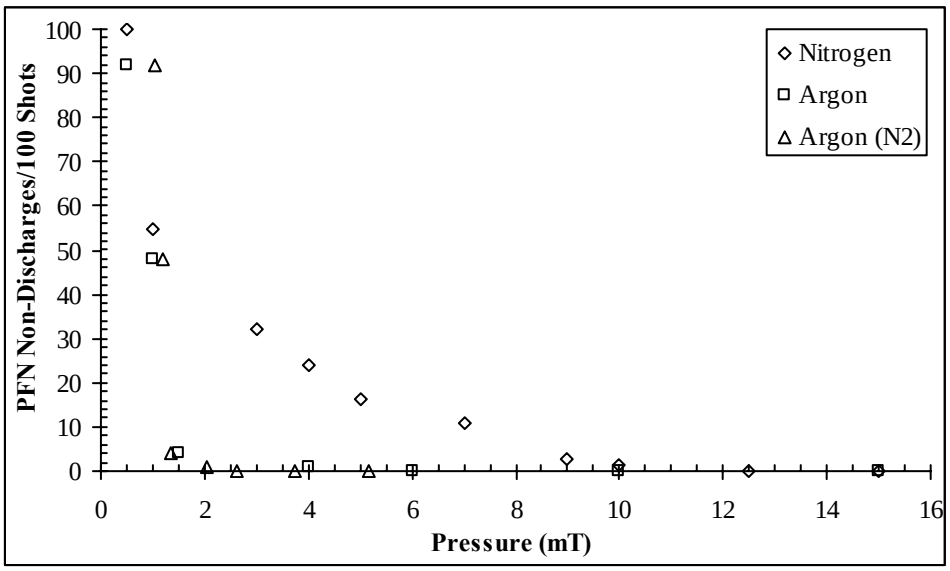

Figure 2.18. PFN non-discharges as a function of pressure for nitrogen and argon ambients.

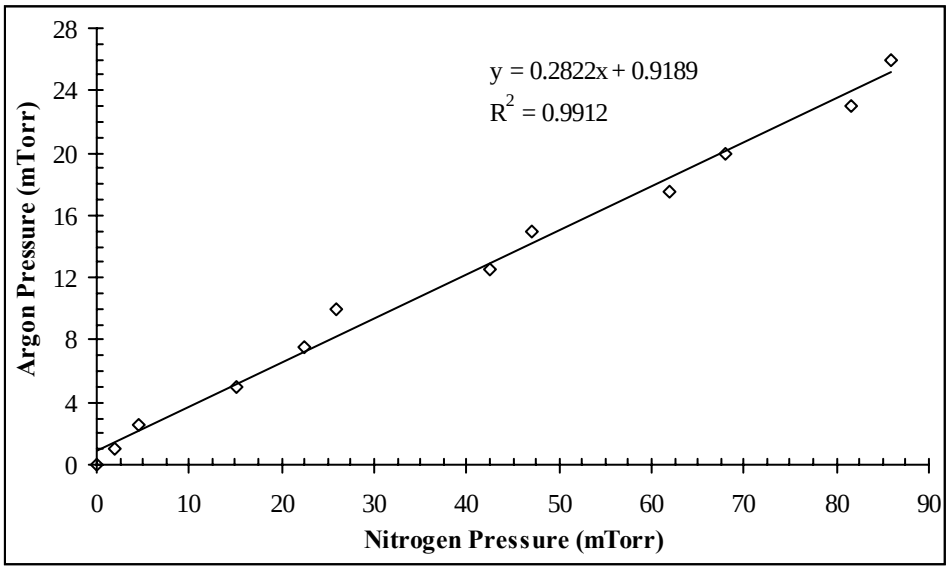

Figure 2.19. Argon pressure as a function of nitrogen pressure.

2.2.5. Reliability Dependence on PFN Initial Voltage

The discharge reliability of the PFN was found to be dependent on the initial voltage of the PFN. The PFN initial voltages in the range of 70 to 100 volts were investigated at various pressures of nitrogen and argon ambient gases. As the pressure was decreased the occurrences of PFN non-discharges increased for both gas types for all voltages, shown in Figures 2.20 and 2.21. In the argon atmosphere the non-discharges did not begin until the pressure was less than 4 mtorr, but in the nitrogen atmosphere the non-discharge began when the pressure was less than 10 mtorr.

In summary, discharge reliability of the PFN is dependent on multiple variables. Non-discharge of the PFN increased as the laser fluence was decreased. The non-discharges also were dependent on the modes of the triggering CO_2 laser. As a function of the decreasing laser fluence; the non-discharges occurred more frequently when triggered by the multiple spatial modes with multiple longitudinal modes laser, than for the single spatial mode with single longitudinal mode laser. The single spatial mode with single longitudinal mode laser allowed the laser fluence to be reduced to 15 mJ/mm^2 without causing non-discharge of the PFN for the hollow-cathode configuration, however, non-discharge occurred at fluences lower than 230 mJ/mm^2 for the hollow-anode configuration.

The discharge reliability of the PFN is dependent on the pressure and type of the ambient gas and the initial voltage of the PFN. Non-discharges of the PFN occurred at pressures less than 10 mtorr in nitrogen, and less than 2 mtorr in argon.

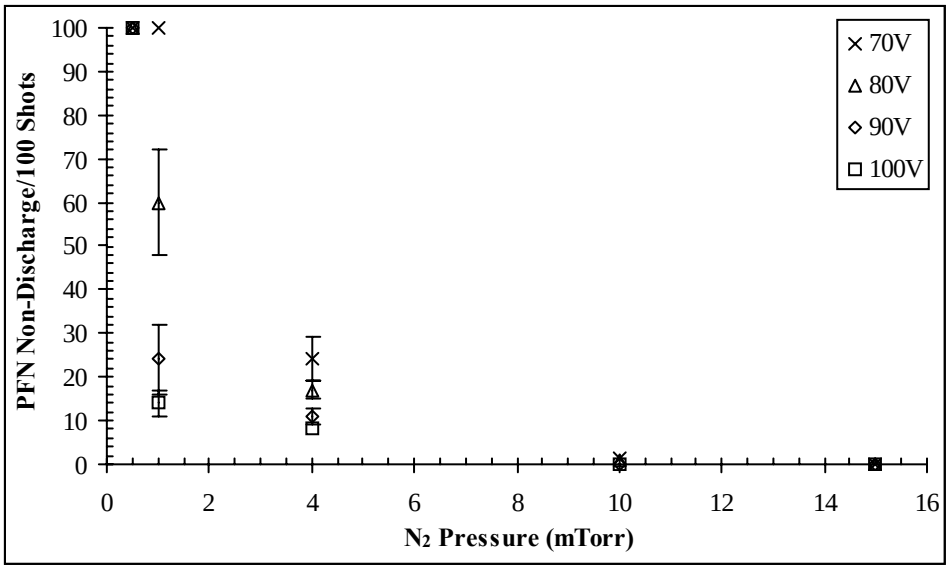

Figure 2.20. PFN non-discharges for various initial PFN voltages as a function of vacuum pressure for nitrogen ambient.

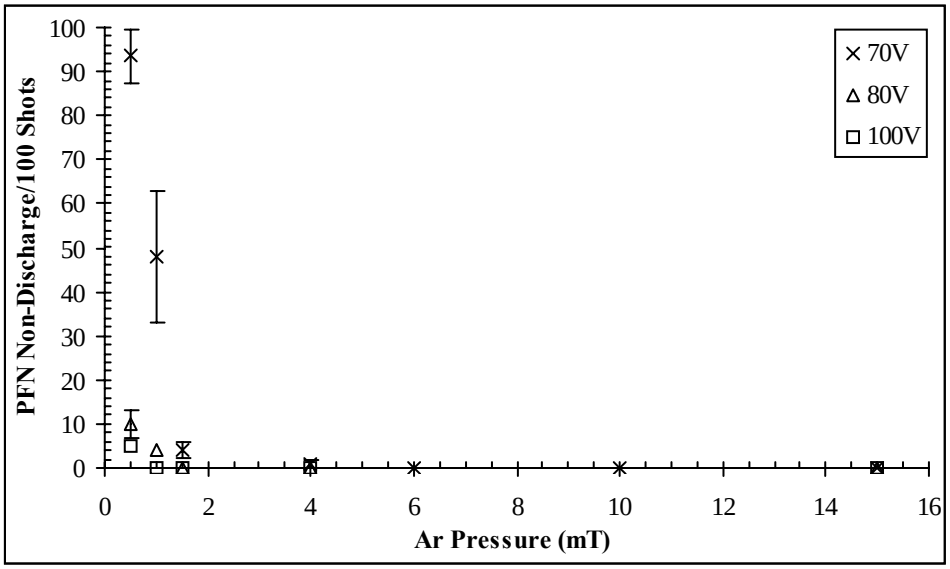

Figure 2.21. PFN non-discharges for various initial PFN voltages as a function of argon ambient pressures.

2.3. Cathode Corrosion

The incident beam of the triggering CO_2 laser caused the carbon hollow-cathode to be corroded. The corroded material can lead to contamination of the system, notably the film. Therefore, it is important to characterize the conditions that lead to corrosion of the cathode.

2.3.1. Experimental Setup

The wall thickness of the carbon hollow cathode was measured and found to be 1.0 millimeter thick. The incident laser shots of the triggering CO_2 laser on the carbon hollow-cathode were counted to determine the number required to corrode through the 1.0 millimeter thick carbon wall. When the incident laser pulses had completely corroded through the wall of the cathode, large particles are visible in the plume exiting the hollow cathode. The three mode types of CO_2 laser were used, multiple spatial modes with multiple longitudinal modes, single spatial mode with multiple longitudinal modes, and single spatial mode with single longitudinal mode.

The initial experiments were conducted using the hollow-cathode configuration, as shown in Figures 2.4. and 2.5. The PFN was operated at an initial voltage of 70V with an inductance of 53.2 μH and a total capacitance of 34 mF. The vacuum chamber was evacuated and back filled with nitrogen to a pressure of 12.5 millitorr. A dynamic pressure was maintained by adjusting the inlet gas flow to produce an ambient pressure of 1.5 millitorr, a gate valve between the chamber and turbo molecular pump was adjusted to restrict the throughput producing the desired back pressure. The CO_2 laser was operated at 1Hz and energy of 196.6 mJ ± 8.1 mJ. The area of the laser spot size was varied by moving the focusing lens position, forming various spot sizes at the surface of

the cathode in the range of 1.2 mm^2 to 10.6 mm^2. The spots were elliptical in shape at the target surface.

2.3.2. Corrosion Dependence on Laser Fluence

The cathode corrosion was found to be dependent on the fluence of the incident CO_2 laser pulse. The laser with multiple spatial modes with multiple longitudinal modes (Laser 1) was used, and operated at 1 Hz and 196.6 ± 8.1 mJ and spot sizes of 1.18 mm^2, 3.14 mm^2, 6.32 mm^2, and 10.6 mm^2. A PFN discharge energy of 10.6 ± 1.9 J was achieved per shot.

Complete corrosion through the hollow-cathode at the various laser spot sizes is shown in Figure 2.22. The white ellipse on each photo is a scale representation of the laser spot size to show the relationship of the corroded area to the size of the laser spot. A pinhole, of approximately the same size, through the wall of the hollow cathode is produced for each laser spot size. The number of laser shots incident on the hollow cathode to corrode through 1.0 millimeter of the cathode wall as a function of the laser spot size is shown in Figure 2.23. The number of shots required to corrode through the cathode increases dramatically as the spot size approaches 1.2 mm^2. There is less corrosion per shot when the laser spot size is small for a given laser energy. As the spot size gets larger more of the laser energy is used to corrode the cathode wall than being used to initiate the plasma.

The number of laser shots required to corrode through 1.0 millimeter of the cathode wall was recorded for the other two CO_2 laser types, single spatial mode with multiple longitudinal modes (Laser 2), and single spatial mode with single longitudinal mode (Laser 3)**.** The laser spot size was set at 0.8 mm^2 and the laser energy per pulse was

varied to achieve a range of laser fluences. The cathode corrosion using each of the three laser types behaved similarly. As the laser fluence was increased the number of laser shots required for complete corrosion increased linearly, but at different rates, as shown in Figure 2.24. To reduce the amount of cathode corrosion, higher laser fluence of the incident triggering CO_2 laser, for a given laser is more desirable.

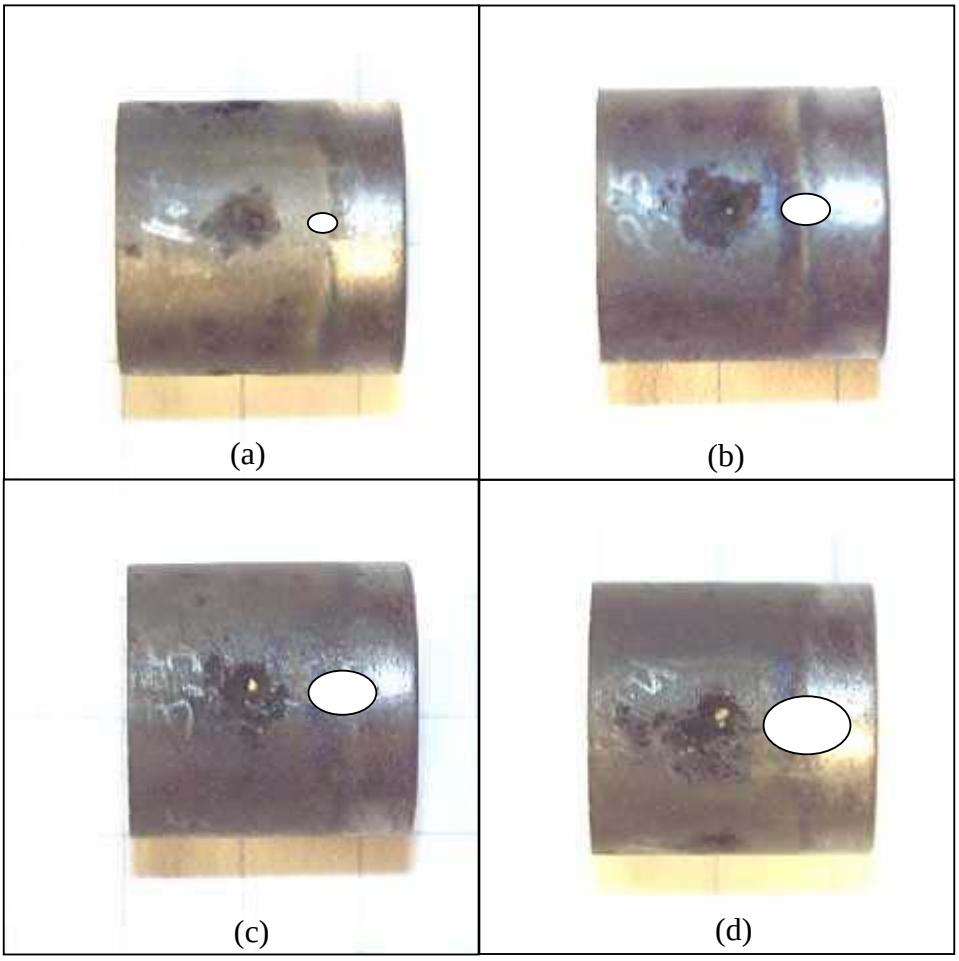

Figure 2.22. Hollow cathode corrosion as a function of laser spot size. The white ellipse is a scale representation of the laser spot size, (a) 1.18 mm^2, (b) 3.14 mm^2, (c) 6.32 mm^2, (d) 10.6 mm^2.

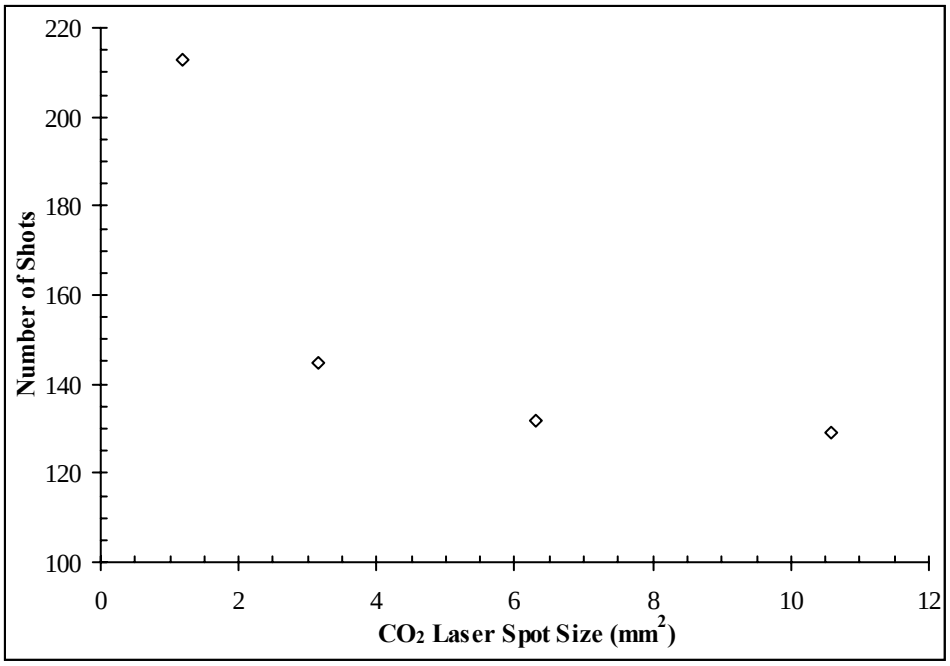

Figure 2.23. Number of laser shots to corrode through 1 mm of carbon as a function of CO_2 laser spot size.

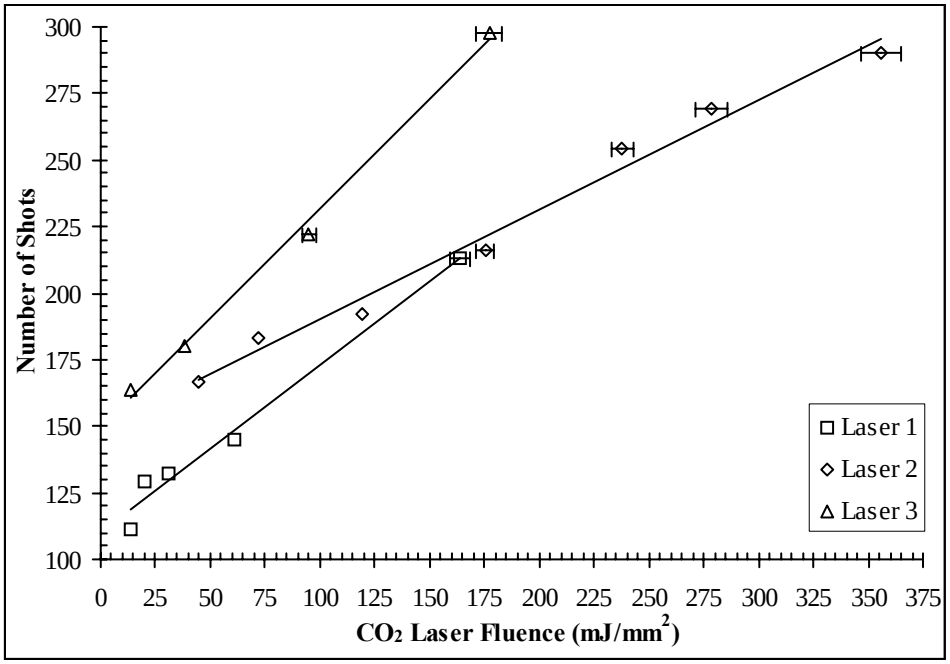

Figure 2.24. Number of laser shots to corrode through 1 mm of carbon as a function of CO_2 laser fluence for each of the three laser types.

2.3.3. Corrosion Dependence on the PFN Discharge Energy

It was observed that cathode corrosion was also dependent on the discharge energy of the PFN. The CO_2 laser with single spatial mode with single longitudinal mode was used, and operated at 1 Hz and 139.8 ± 5.3 mJ and a spot size of 0.8 mm^2, for a laser fluence of 178.1 ± 6.8 mJ/mm^2. The initial voltage of the PFN was varied between 70 and 100 VDC in order to vary the PFN discharge energy. As the PFN discharge energy increased the number of shots required to corrode through the cathode wall increased, decreasing the corrosion rate, as shown in Figure 2.25. At PFN discharge energies greater than 70 J, no corrosion could be detected even after 3500 laser shots. At PFN energies between 60 to 70 J, corrosion was present but not enough to pass through the wall after 2000 shots. At PFN discharge energies lower than 17 J, there appears to be a constant rate of corrosion, as shown in Figure 2.26.

A high PFN discharge energy, greater than 70 J, produces no cathode corrosion at the site of the incident triggering CO_2 laser pulse. At lower energies corrosion is present and can contaminate the system.

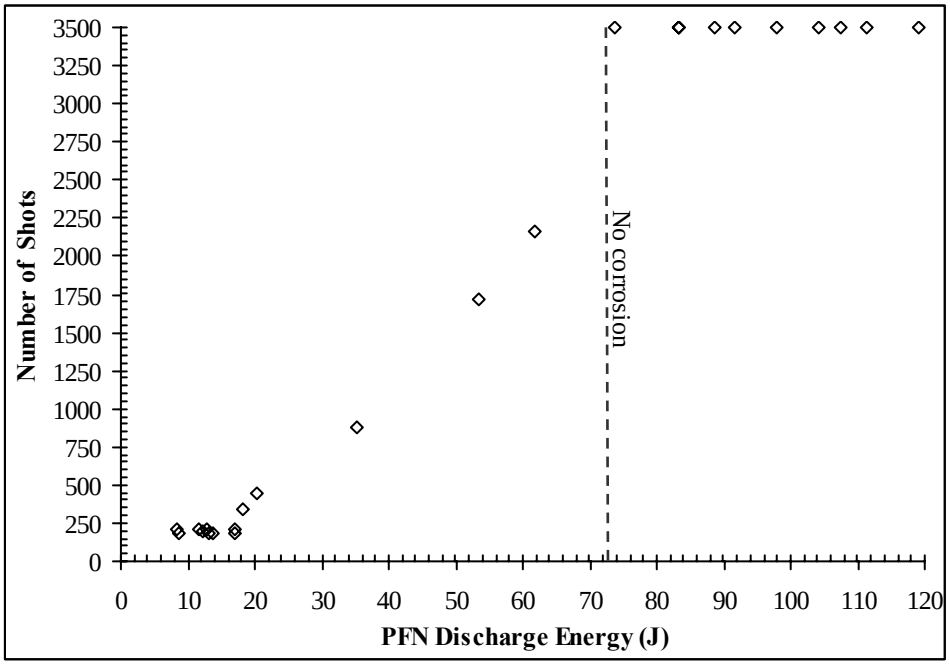

Figure 2.25. Number of laser shots to corrode through 1 mm of carbon as a function of PFN discharge energy.

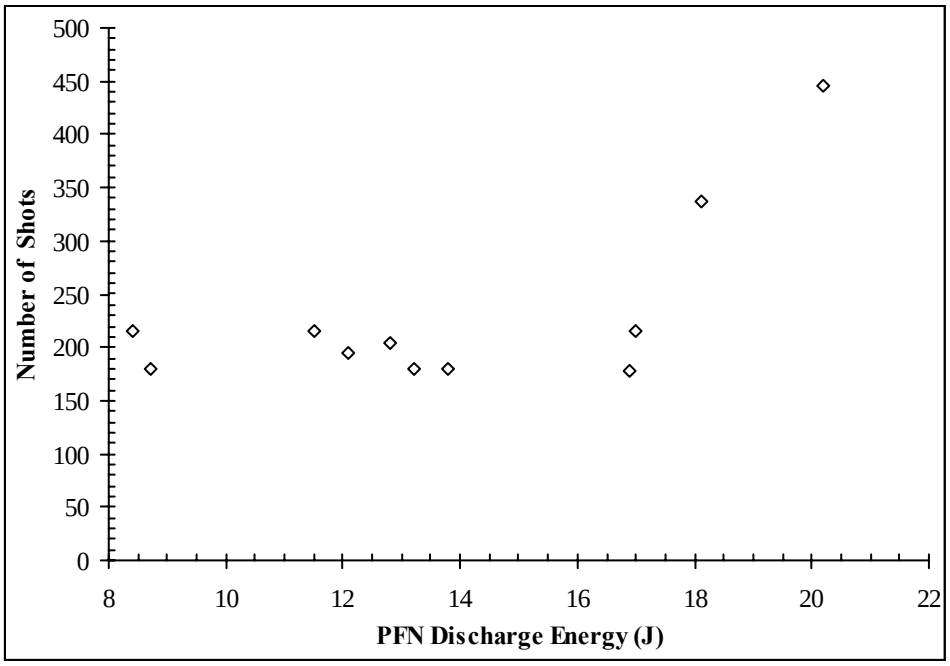

Figure 2.26. Detail of low energy for the number of laser shots to corrode through 1 mm of carbon as a function of low PFN discharge energy.

2.3.4. Ablation Shielding of the Cathode Corrosion

The material ablated from the site of the cathode corrosion ultimately deposits on the substrate. A 10 cm diameter glass ablation shield was constructed with a 1.3 cm diameter hole in the center. The ablation shield was placed concentrically in front of the hollow-cathode discharge head, as shown in Figure 2.27.

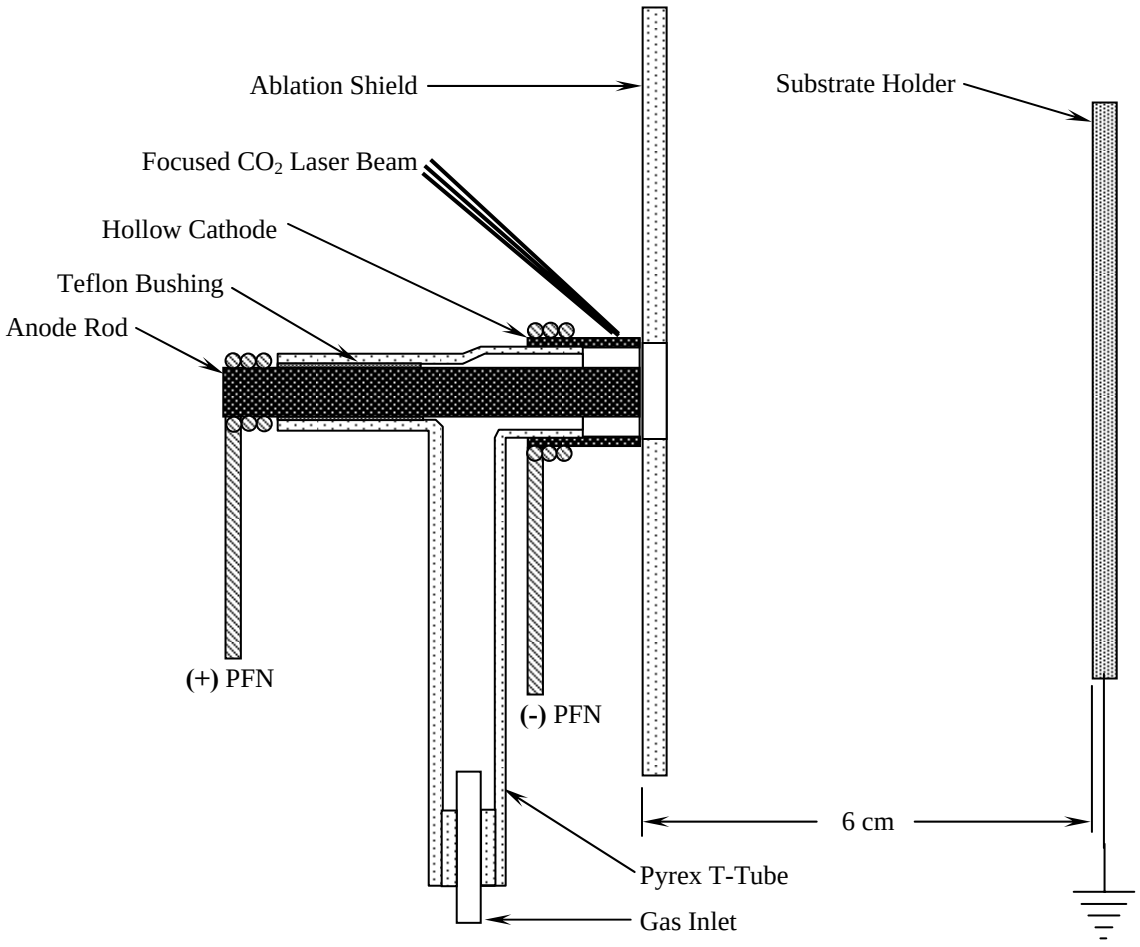

Figure 2.27. Cross-sectional view of the hollow-cathode discharge head with the ablation shield.

The CO_2 laser with single spatial mode with single longitudinal mode was used, and operated at 1 Hz and 145.4 ± 2.5 mJ and a spot size of 0.8 mm^2, for a laser fluence of 185.3 ± 3.2 mJ/mm^2. The initial voltage of the PFN was 70 VDC providing discharge energy of 46.6 ± 1.6 J. Trials were conducted with and without the ablation shield in place to determine the effect on the film growth after 250 discharges. Without the ablation shield in place the resulting film growth was 1.1 – 1.5 Å/shot and no film growth was detectable when the ablation shield was in place, see Figure 2.28. The deposited material was therefore entirely due to ablation of the cathode by the triggering CO_2 laser.

In summary, the incident beam of the triggering CO_2 laser can cause the carbon cathode to be corroded. The material ablated by the triggering laser which causes the corrosion contaminates the film if not properly shielded. The corrosion decreases as the laser fluence and PFN discharge energy is increased. There is no detectable corrosion when the PFN discharge energy is greater than 70 J and the laser fluence was approximately 180 mJ/mm^2.

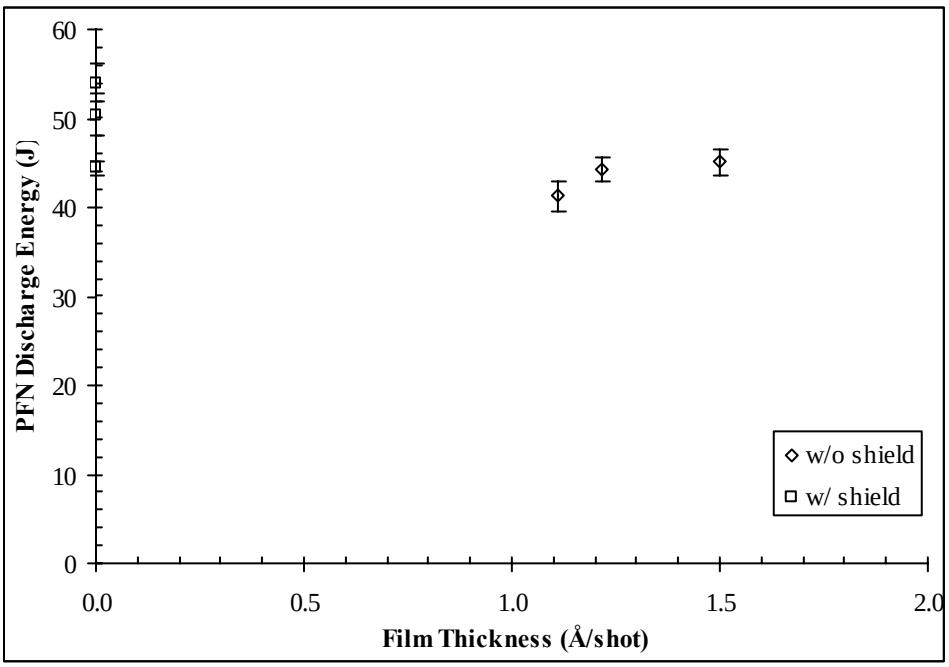

Figure 2.28. Carbon film growth with and without the ablation shield.

2.4. Characterization of the Pulse Forming Network

In the hollow-cathode plasma discharge system, the PFN capacitive stage is charged to the desired voltage to store the energy for the transient discharge. The current flowing in the PFN circuit is determined by the impedance of the circuit with the plasma as the load. The current pulse generated during the arc discharge corresponds to the total energy imparted to the plasma system by the PFN which in turn affects the properties of the resulting plasma. Therefore it is important to characterize the current pulses produced under different conditions to understand the effect of the basic parameters that determine the nature of the transient plasma. Preliminary studies have shown that the current pulse generated during the arc discharge depends on the background pressure, type of ambient gas, PFN initial voltage, total capacitance, and inductance used in the plasma discharge system. This section describes the experimental study carried out to determine the effect of these factors on generated current pulses.

2.4.1. Experimental Setup

The current pulses generated during the plasma arc discharge, at an initial voltage, V_i, of 70 VDC, and a capacitance, C, of 34 mF were obtained using an inductive coil pickup. The inductor used was a commercial pickup coil with a 5 centimeter diameter opening. The pickup coil was placed symmetrically around the wire connecting the positive side of the PFN to the anode of the discharge head. The pickup coil was then connected to a 1 GHz oscilloscope. The EMF generated due to the transient discharge was recorded (as a *.csv file) on the oscilloscope in the form of a voltage signal as a function of time. A voltage signal for a single PFN discharge recorded at 12 mTorr of

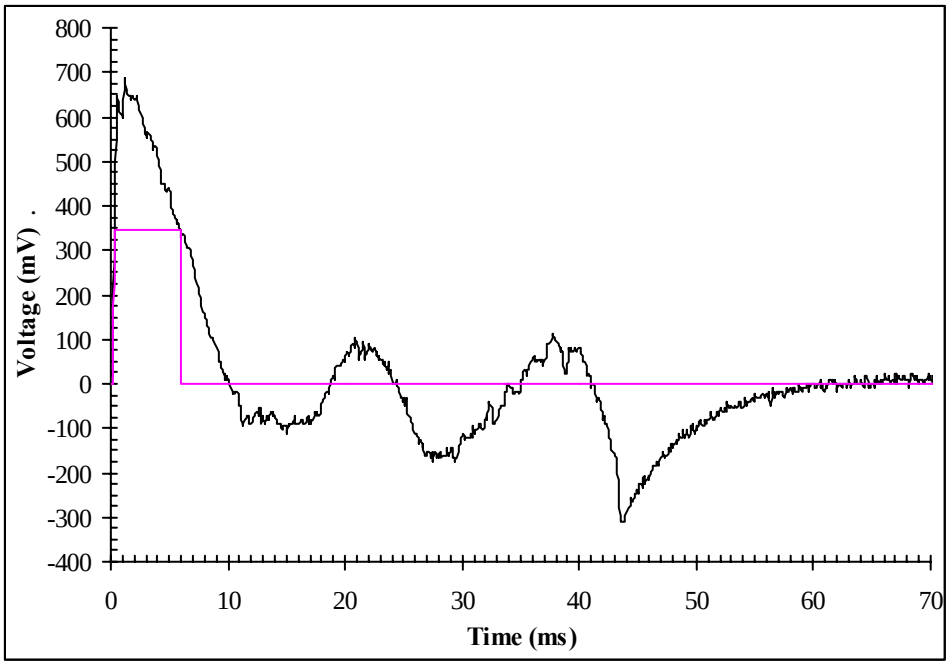

Figure 2.29. A voltage signal for a single PFN discharge at 12 mTorr of nitrogen.

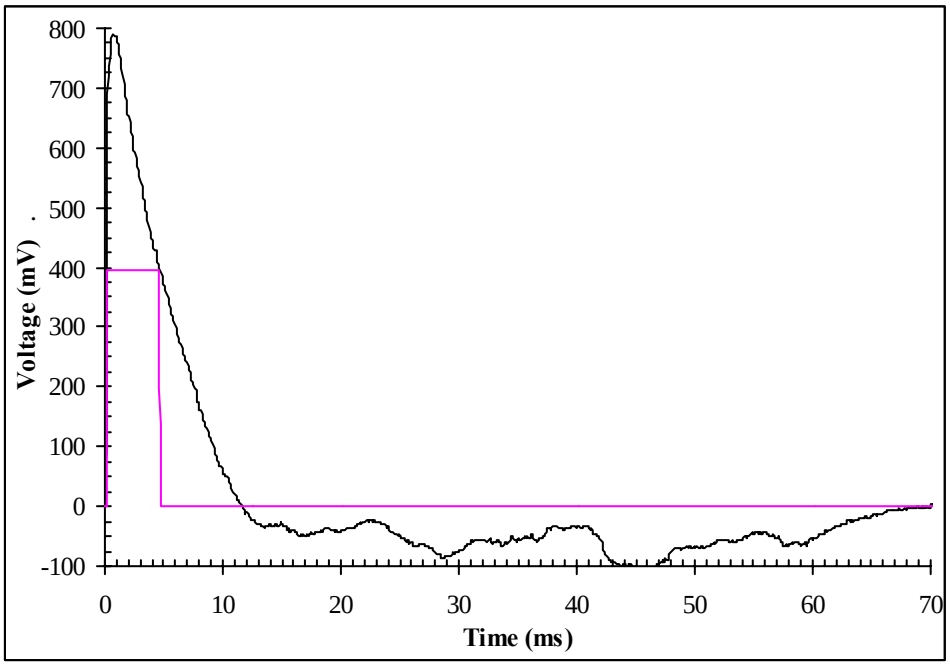

Figure. 2.30. An averaged voltage signal at 12 mTorr of nitrogen.

nitrogen is shown in Figure 2.29. An averaged voltage signal for 16 PFN discharges was recorded for current pulse calculations, shown in Figure 2.30.

To determine the final discharge voltage, V_f, of the PFN capacitor stage, the capacitor(s) was charged to its initial value and the discharge was triggered with the charging power supply disconnected. This prevented the charging of the capacitor after the discharge and allowed the determination of the final residual voltage of the capacitor. This procedure was repeated to obtain an average value and standard deviation for V_f.

The area, A_V, under the recorded voltage signal, as shown in Figure 2.30., is proportional to the total charge, q, out of the capacitor by a constant factor of k_V. The area, A_V, under the averaged voltage signal is calculated by summation of slivers of area, a, under the curve from the recorded signal, as shown in Figure 2.31. An instance of area a is calculated by equation 2.3 such that;

$$\begin{aligned} a &= bh_1 + \frac{1}{2}b(h_2 - h_1) \\ a &= bh_1 + \frac{1}{2}bh_2 - \frac{1}{2}bh_1 \\ a &= \frac{1}{2}bh_1 + \frac{1}{2}bh_2 \\ a &= \frac{1}{2}b(h_1 + h_2) \\ a &= \frac{1}{2}(t_2 - t_1)(V_1 + V_2) \end{aligned} \qquad [2.3]$$

then the area A_V can be calculated by equation 2.4;

$$\begin{aligned} A_V &= \sum_{n=0}^{t} a(V,t) \\ A_V &= \sum_{n=0}^{t} \frac{1}{2}(t_{n+1} - t_n)(V_n + V_{n+1}) \end{aligned} \qquad [2.4]$$

where t_n and V_n are data points recorded in the oscilloscope file of the transient discharge. Then the constant of proportionality k_V can be calculated by equation 2.5;

$$\begin{aligned} k_V \cdot A_V &= q \\ k_V \cdot A_V &= CV \\ k_V \cdot A_V &= C\Delta V \\ k_V \cdot A_V &= C(V_i - V_f) \end{aligned}$$

$$k_V = \frac{C(V_i - V_f)}{A_V} \qquad [2.5]$$

The voltage, $V(t)_C$, on the capacitor stage, the potential across the discharge head, at time t can be calculated by rearranging equation 2.5 for V_f and calculating the area under the recorded voltage signal up to the time of interest by equation 2.6;

$$\begin{aligned} V_f &= V_i - \frac{k_V A_V}{C} \\ V(t)_C &= V_i - \frac{k_V \sum_{n=0}^{t} A(t)_V}{C} \end{aligned} \qquad [2.6]$$

The discharge voltage, $V(t)_C$ signal as a function of time is shown in Figure 2.32.

The energy, U, stored on a charged capacitor is given by equation 2.7;

$$U = \frac{1}{2} CV^2 \qquad [2.7]$$

The total energy, E_C, discharged from the PFN capacitor stage can then be determined by the difference between the initial energy stored on the capacitor and the final energy remaining stored on the capacitor after the pulsed discharge is complete, given by equation 2.8;

$$\begin{aligned} E_C &= \frac{1}{2} CV_i^2 - \frac{1}{2} CV_f^2 \\ E_C &= \frac{1}{2} C(V_i^2 - V_f^2) \end{aligned} \qquad [2.8]$$

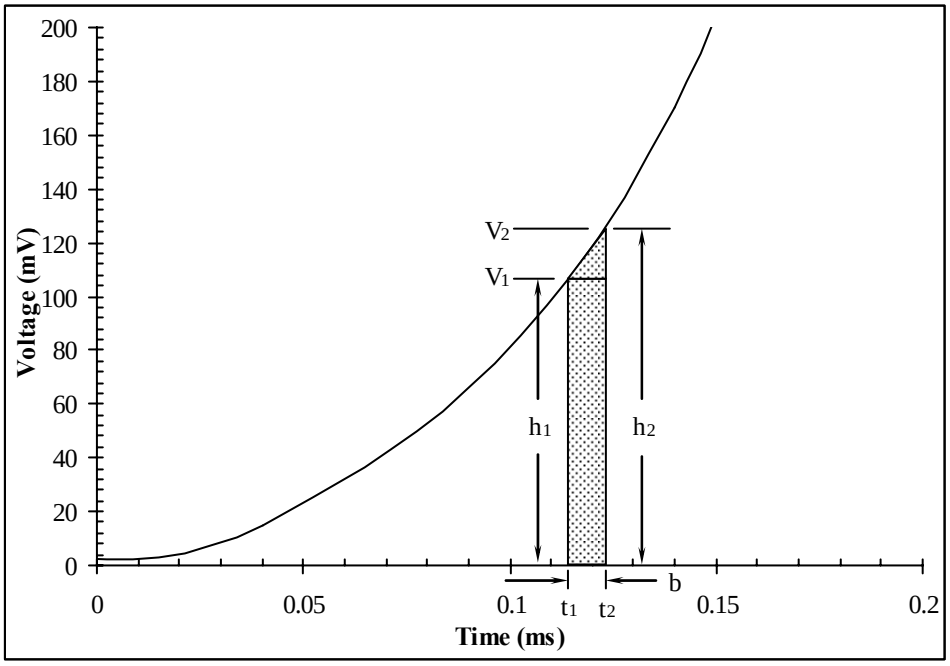

Figure. 2.31. Calculation of the area, A_V, under the signal curve.

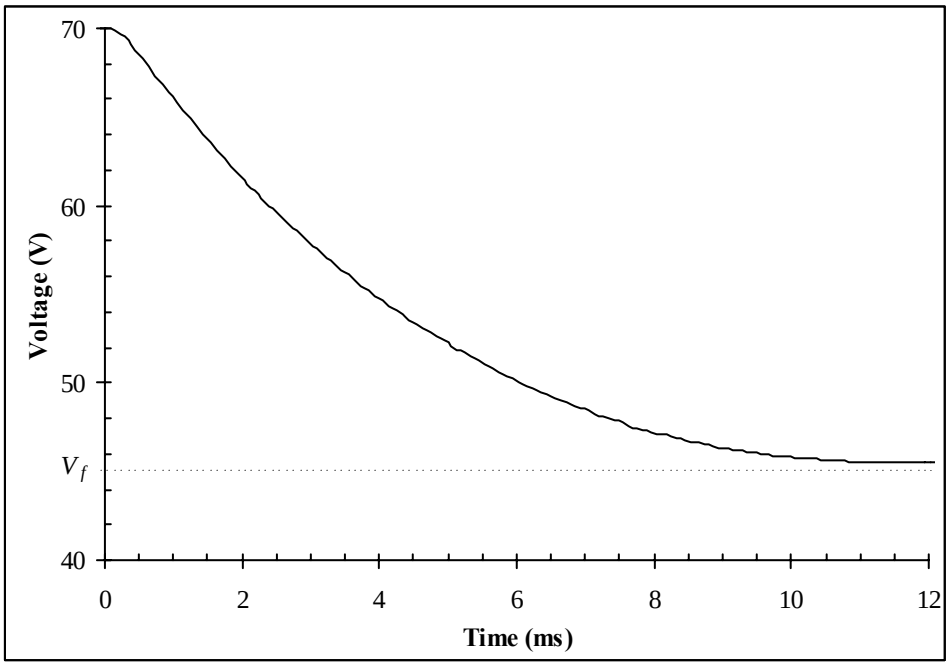

Figure. 2.32. Voltage across the PFN capacitor stage as a function of time.

The discharge energy as a function of time is calculated by substituting $V(t)_C$ from equation 2.6 for V_f as shown in equation 2.9;

$$E_C(t) = \frac{1}{2}C(V_i^{\,2} - V(t)_C^{\,2}) \qquad [2.9]$$

The energy, $E_C(t)$, discharged from the PFN as a function of time is shown in Figure 2.33.

The area under the current pulse curve, A_I, can be calculated from equation 2.6 such that;

$$\begin{aligned} U &= \frac{1}{2}CV^2 \\ U &= \frac{1}{2}\frac{q}{V}V^2 \\ U &= \frac{1}{2}qV \\ U &= \frac{1}{2}V\int I \cdot dt \end{aligned} \qquad [2.10]$$

and since;

$$A_I = \int I \cdot dt \qquad [2.11]$$

then, combining equations 2.10, 2.11 and the results of equation 2.6, a calculated value for the area under the current pulse curve, A_I, is given by equation 2.12;

$$\begin{aligned} U &= \frac{1}{2}VA_I \\ E_C &= \frac{1}{2}V_iA_I \\ A_I &= \frac{2E_C}{V_i} \end{aligned} \qquad [2.12]$$

The constant of proportionality for the current pulse, k_I, can be determined by the ratio given by the results of equation 2.10 to equation 2.4 such that;

$$k_I = \frac{A_I}{A_V} \qquad [2.11]$$

Then the current as a function of time, *I(t)*, can be calculated from the recorded voltage signal as shown in Figure 2.30. and by equation 2.12;

$$I(t) = k_I \cdot V(t) \qquad [2.12]$$

The calibrated current signal as a function of time is shown Figure 2.34. The peak current, I_p, is then obtained from the maximum of equation 2.12, and the full width half maximum of the current pulse, $FWHM_I$.

The impedance, *Z(t)*, of the plasma system can be determined by the result of equation 2.4 and 2.12 such that equation 2.13 is;

$$Z(t) = \frac{V(t)_C}{I(t)} \qquad [2.13]$$

The impedance of the plasma system as a function of time is shown in Figure 2.35.

These calculations are then compiled to characterize the discharge of the PFN. The typical results that are monitored are; the PFN discharge voltage (V_f), the current pulse full width half maximum ($FWHM_I$), the peak discharge current (I_p), and the total PFN discharge energy (E_C).

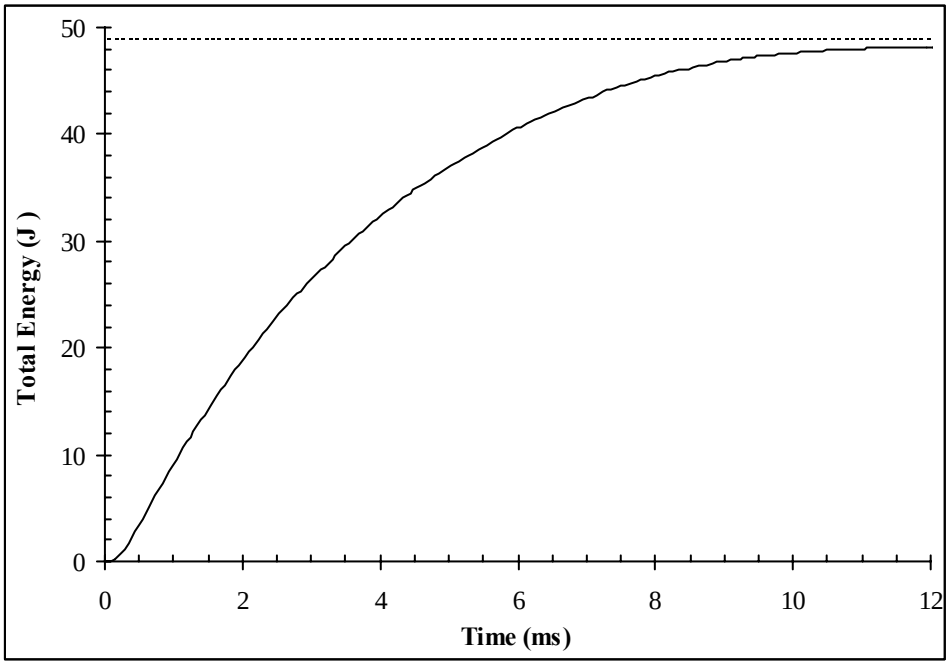

Figure. 2.33. Energy discharged from the PFN as a function of time.

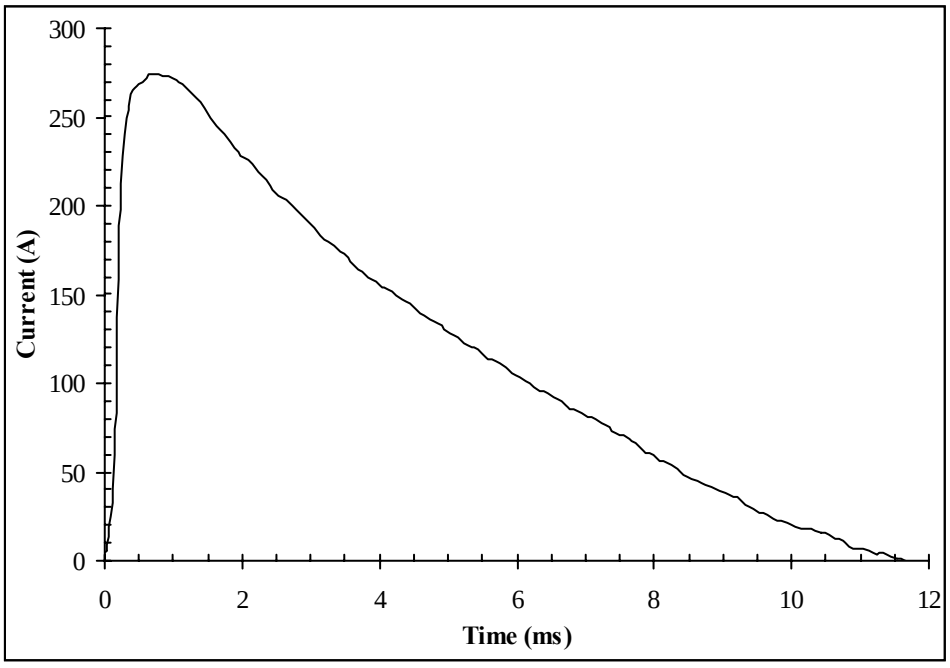

Figure. 2.34. The calibrated discharge current signal at 12 mTorr of nitrogen.

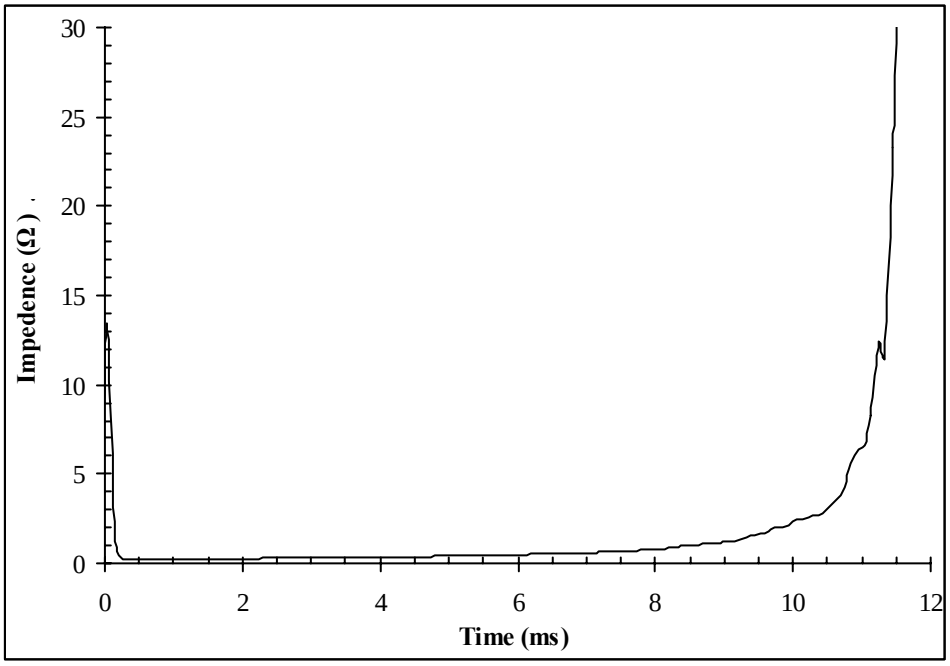

Figure. 2.35. Impedance of the plasma system as a function of time.

2.4.2. PFN Dependence on Triggering Laser Fluence

This section describes the arc discharge through investigations of the current pulses generated during the plasma arc discharge with different fluences of the triggering CO_2 laser. The arc discharge is described by the final discharge voltage (V_f) the current pulse $FWHM_I$, the peak current (I_p) of the current pulse, and the total discharge energy (E_C) of the PFN. The triggering CO_2 laser was operated at energies in the range of 11 to 281 mJ with a spot size of 0.8 mm^2 at the cathode, producing laser fluences in the range of 13.8 to 358.0 mJ/mm^2. The system was operated in a nitrogen ambient at a pressure of 12 mTorr, and a PFN capacitance of 34 mF at an initial voltage of 70 VDC. The single spatial mode with single longitudinal mode laser was utilized as the triggering laser to minimize the PFN non-discharges that could occur during the trial, as investigated in Chapter 2.2.4.2.

In summary, the characteristics of the current pulse discharge, V_f, $FWHM_I$, I_P, and E_C, are independent of the triggering laser fluence, linear and fairly constant over the range of laser fluences with little significant difference from one extreme to the other. The final PFN discharge voltage, V_f, averaged 44.5 ± 2.2 V, as shown in Figure 2.36. V_f decreased slightly as laser fluence was increased, but not significantly different. The current pulse $FWHM_I$ averaged 4.1 ± 0.5 ms, as shown in Figure 2.37. The peak current, I_P, and total discharge energy, E_C, imparted to the plasma system were calculated based on V_i, V_f, and the PFN capacitance, C, as described in Chapter 2.4.1. The peak current, I_P, averaged 287.7 ± 20.8 A, as shown in Figure 2.38. I_P increased slightly as the laser fluence was increased, but not significantly different. The total energy discharged from the PFN, E_C, averaged 49.7 ± 3.2 J, as shown in Figure 2.39. E_C increased slightly as the laser fluence was increased, but not significantly different.

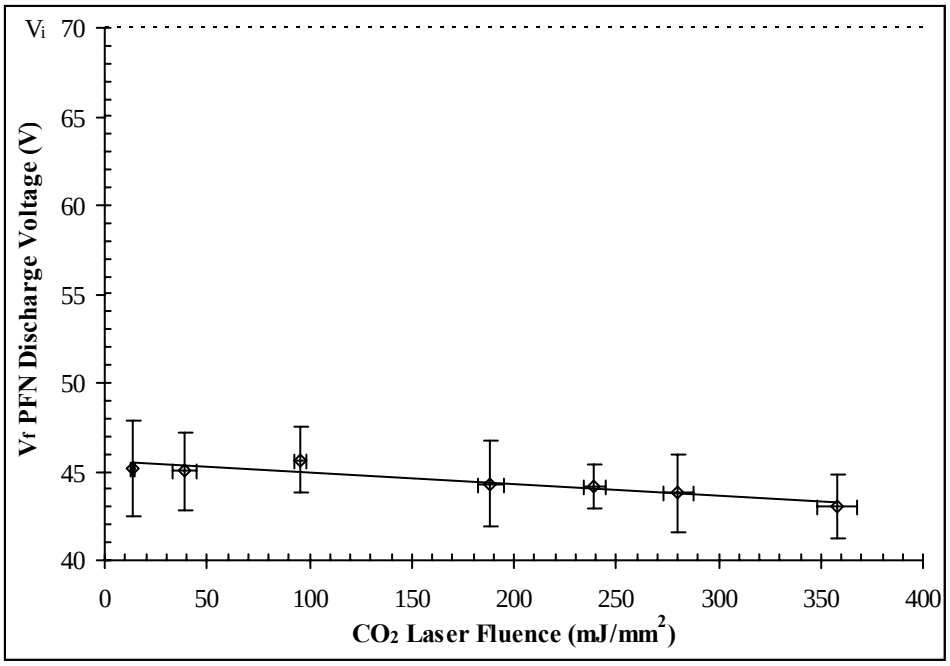

Figure 2.36. PFN discharge voltage as a function of CO_2 laser fluence.

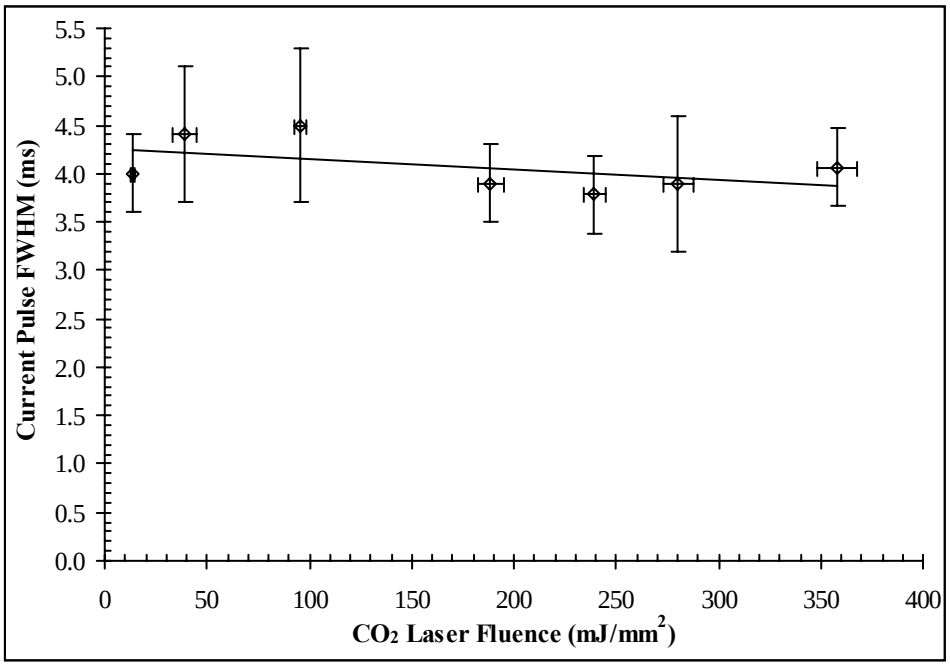

Figure 2.37. Current pulse FWHM as a function of CO_2 laser fluence.

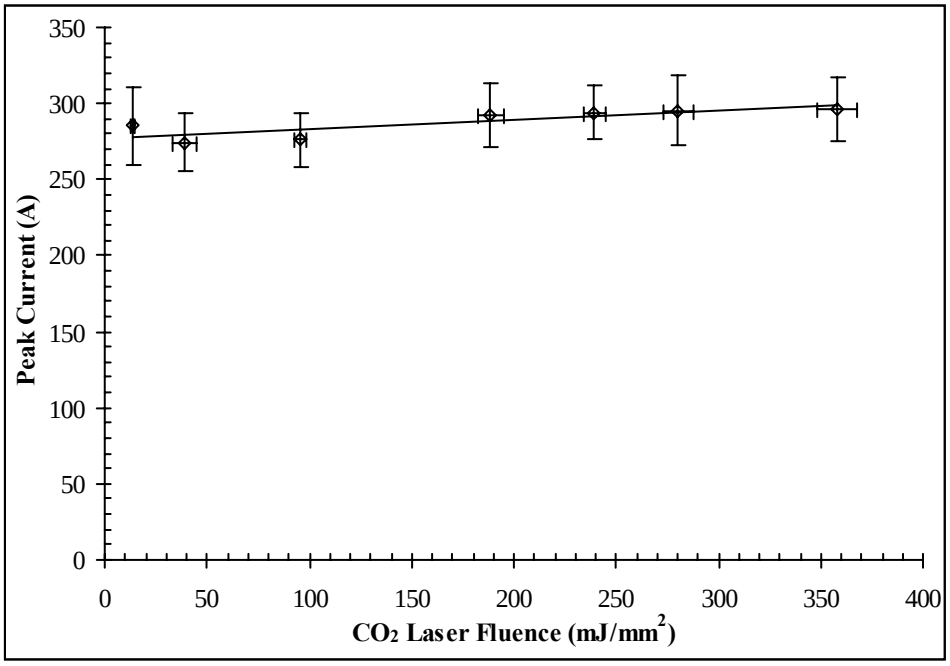

Figure 2.38. Peak current as a function of CO_2 laser fluence.

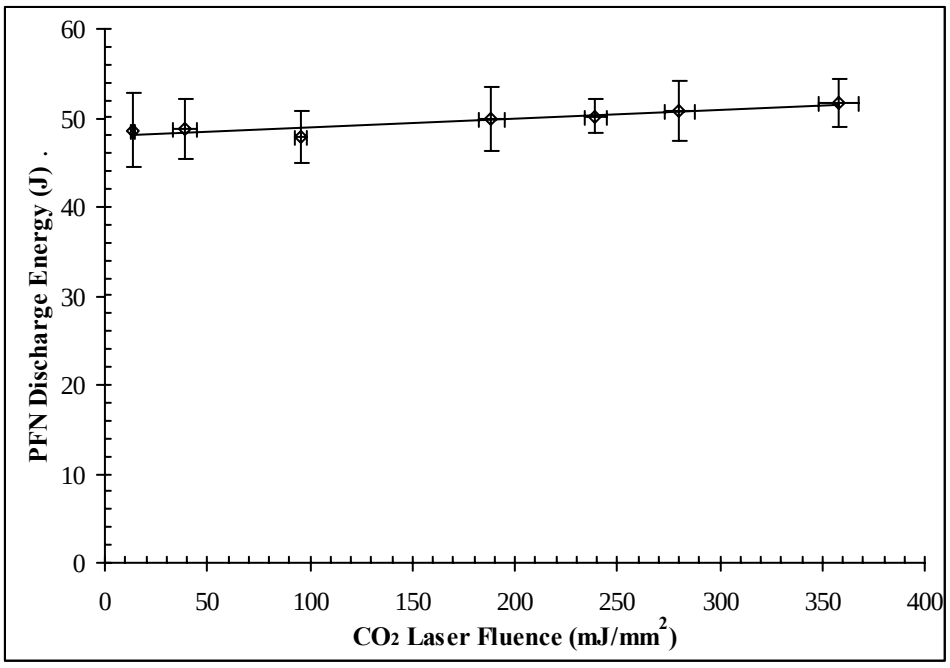

Figure 2.39. PFN discharge energy as a function of CO_2 laser fluence.

2.4.3. PFN Dependence on Ambient Pressure

This section describes the arc discharge through investigations of the current pulses generated during the plasma arc discharge with different argon and nitrogen atmosphere pressures of the vacuum chamber. The triggering CO_2 laser was operated at energy of 133.0 ± 2.9 mJ with a spot size of 0.8 mm^2 at the cathode, producing a laser fluence of 169.4 ± 3.7 mJ/mm^2. The single spatial mode with single longitudinal mode laser was utilized as the triggering laser to minimize the PFN non-discharges that could occur during the trial. The system was operated at varied ambient pressures, and a PFN capacitance of 39 mF at an initial voltage of 70 VDC.

The current pulses were produced with different ambient gas pressures in the range of 1 to 50 mTorr in both nitrogen and argon backgrounds. The characteristics of the current pulse discharge, V_f, $FWHM_I$, I_P, and E_C, were significantly dependent on the ambient gas pressure as well as the type of gas used.

At higher pressures of argon and nitrogen, 12 to 50 mTorr, the values of V_f, $FWHM_I$, I_P, and E_C, become constant, as shown in Figures 2.40. through 2.43. The average constant values for the PFN characteristics are shown in Table 2.1. The characteristics change quickly for pressures 1 to 12 mTorr for both argon and nitrogen. The pulse duration is shorter for the plasma generated in argon ambient but the peak current is greater resulting in more total energy being imparted to the argon plasma system than the nitrogen plasma.

	V_f (V)	$FWHM_I$ (ms)	I_P (A)	E_C (J)
Argon	30.0 ± 0.8	2.3 ± 0.1	626.2 ± 14.4	64.4 ± 1.2
Nitrogen	45.5 ± 1.4	4.4 ± 0.3	212.2 ± 11.8	55.2 ± 2.4

Table 2.1. Average PFN characteristics for 12 to 50 mTorr of argon and nitrogen.

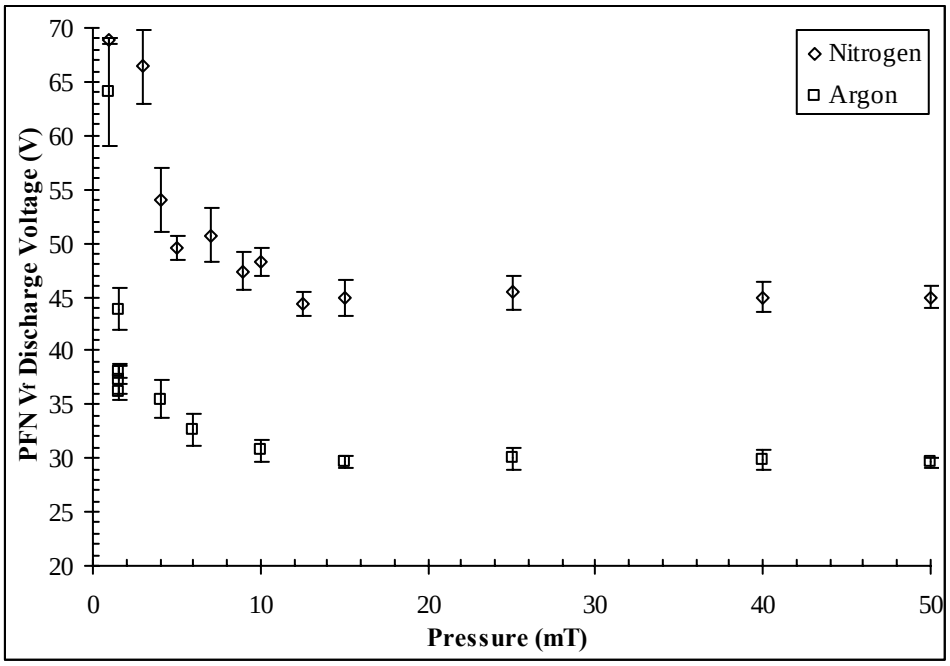

Figure 2.40. PFN final discharge voltages obtained for argon and nitrogen pressures.

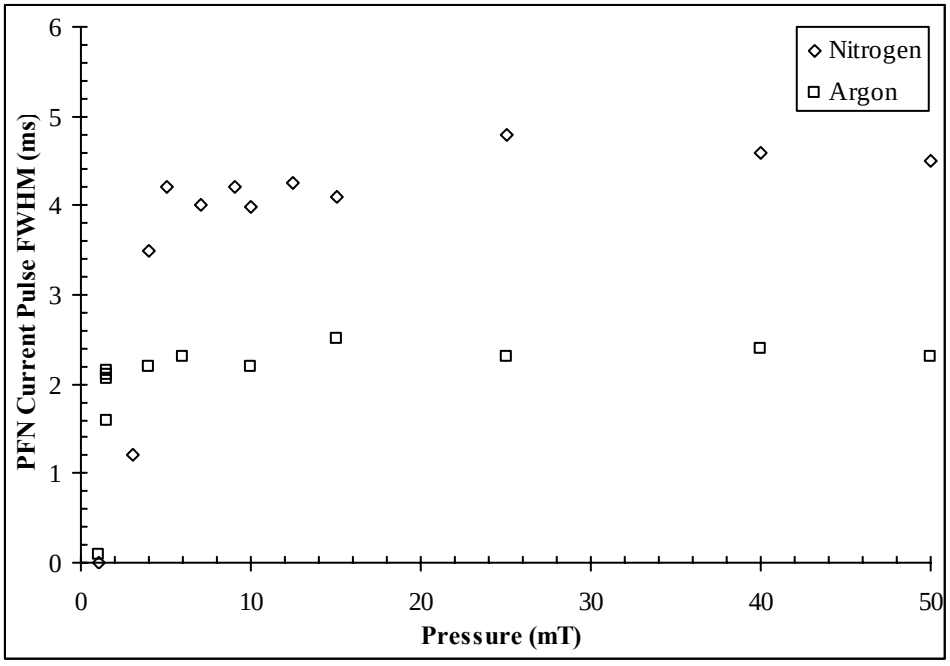

Figure 2.41. PFN current pulse FWHM obtained for different argon and nitrogen pressures.

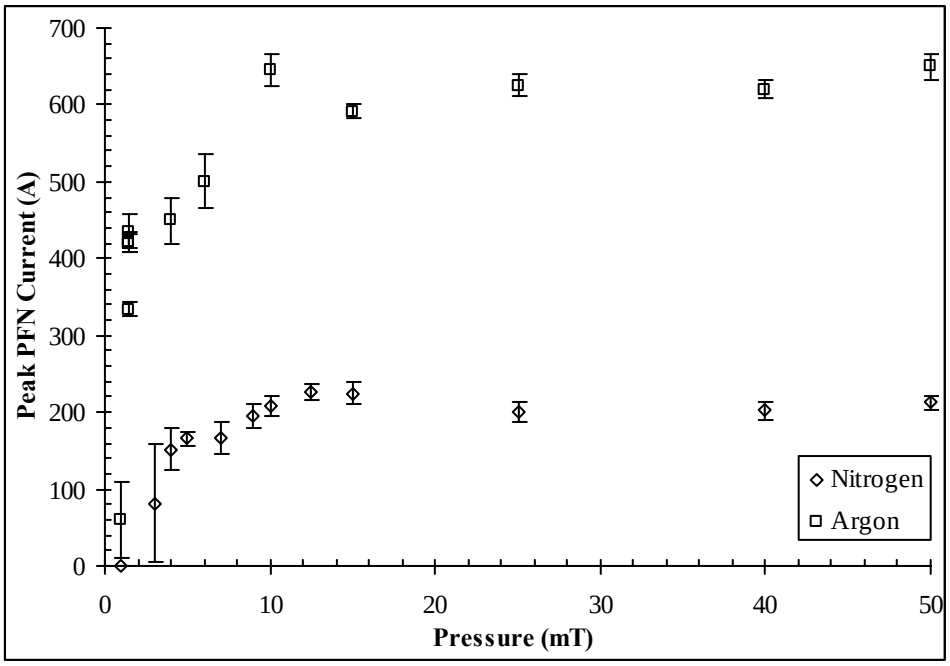

Figure 2.42. Calculated PFN peak currents for different argon and nitrogen pressures.

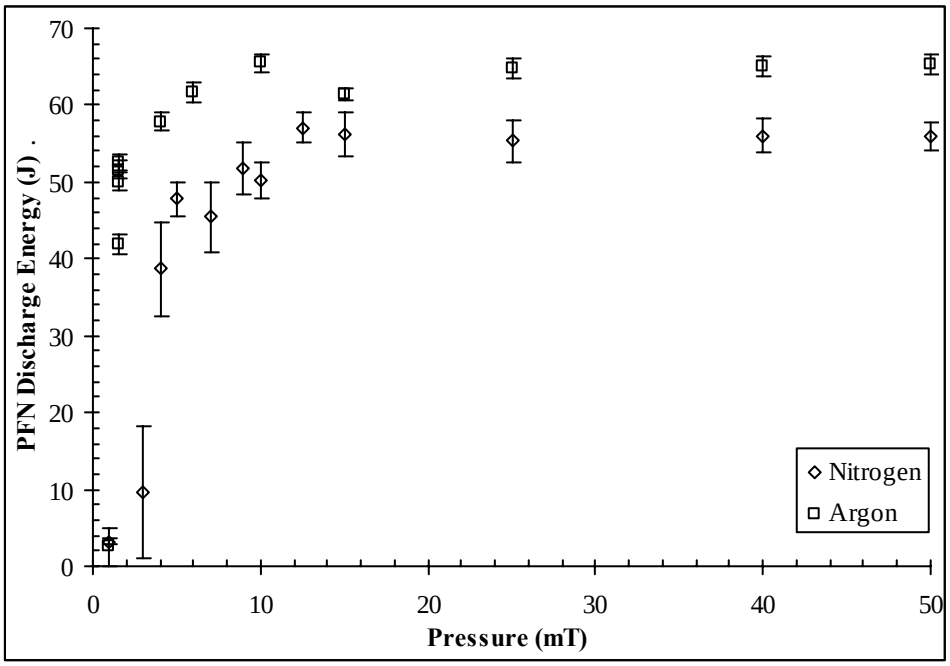

Figure 2.43. PFN discharge energy imparted to the plasma system for different argon and nitrogen pressures.

2.4.4. PFN Dependence on Network Grounding

This section describes the arc discharge through investigations of the current pulses generated during the plasma arc discharge with different arrangements provided for the electrical grounding of the PFN. Referring to PFN schematic diagram and system diagram in Figures 2.2. and 2.5., respectively, the PFN was varied from positive, negative, and floating ground. The triggering CO_2 laser was operated at an energy of 135.3 ± 7.3 mJ with a spot size of 0.8 mm^2 at the cathode, producing a laser fluence of 172.3 ± 9.3 mJ/mm^2. The single spatial mode with single longitudinal mode laser was utilized as the triggering laser to minimize the PFN non-discharges that could occur during the trial, as investigated in Chapter 2.2.4.2. The system was operated at nitrogen ambient pressures in the range of 10 to 35 mTorr where the PFN characteristics are linear as a function of ambient pressure as investigated in Chapter 2.4.3., and a PFN capacitance of 39 mF at an initial voltage of 70 VDC.

The characteristics of the current pulse discharge, V_f, $FWHM_I$, I_P, and E_C, were found to be independent of positive and no PFN grounding, as seen in Figure 2.44. through 2.47. However, the capacitors of the PFN would not discharge when triggered by the incident CO_2 laser when the PFN was negatively grounded.

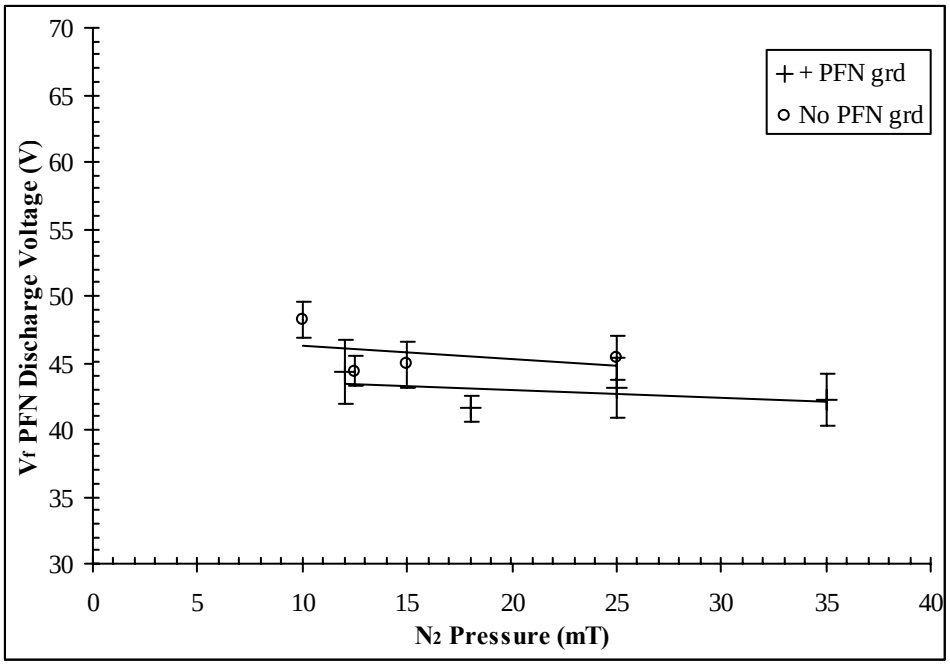

Figure 2.44. PFN final discharge voltage for different PFN ground options in different nitrogen pressures.

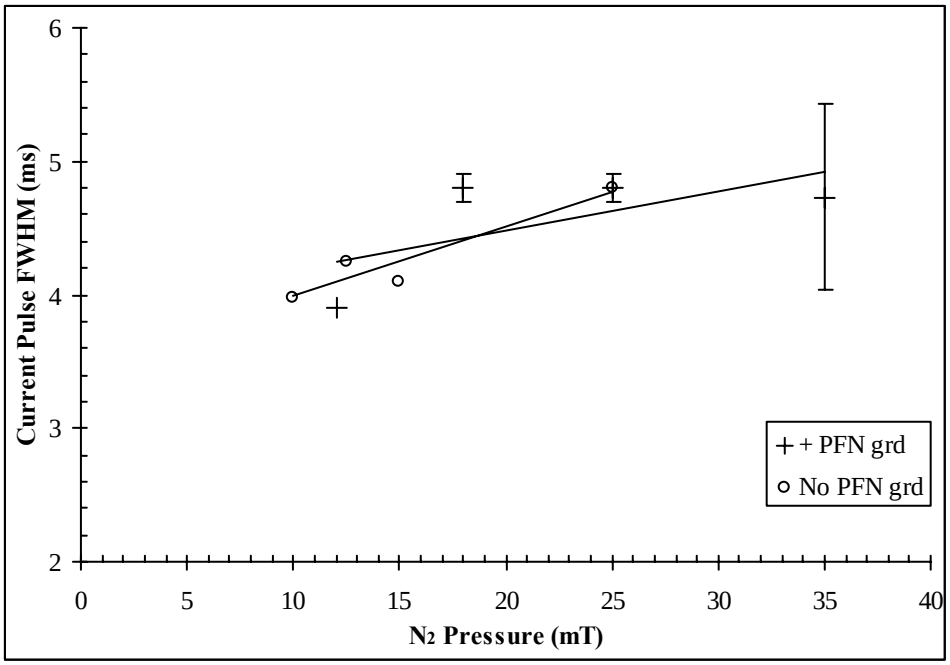

Figure 2.45. PFN current pulse FWHM obtained for different PFN ground options in different nitrogen pressures.

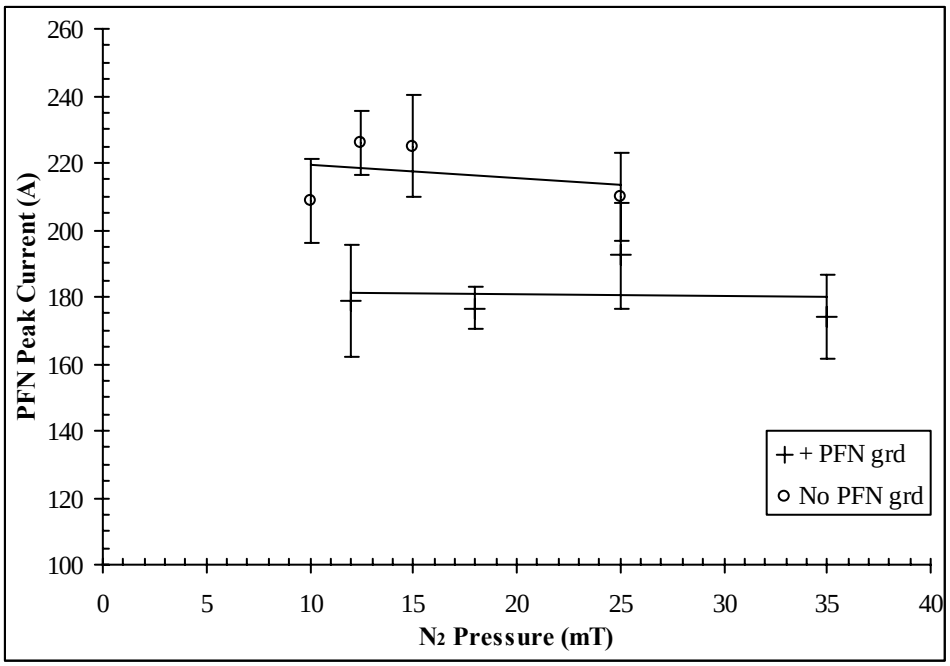

Figure 2.46. Calculated PFN peak current for different PFN ground options in different nitrogen pressures.

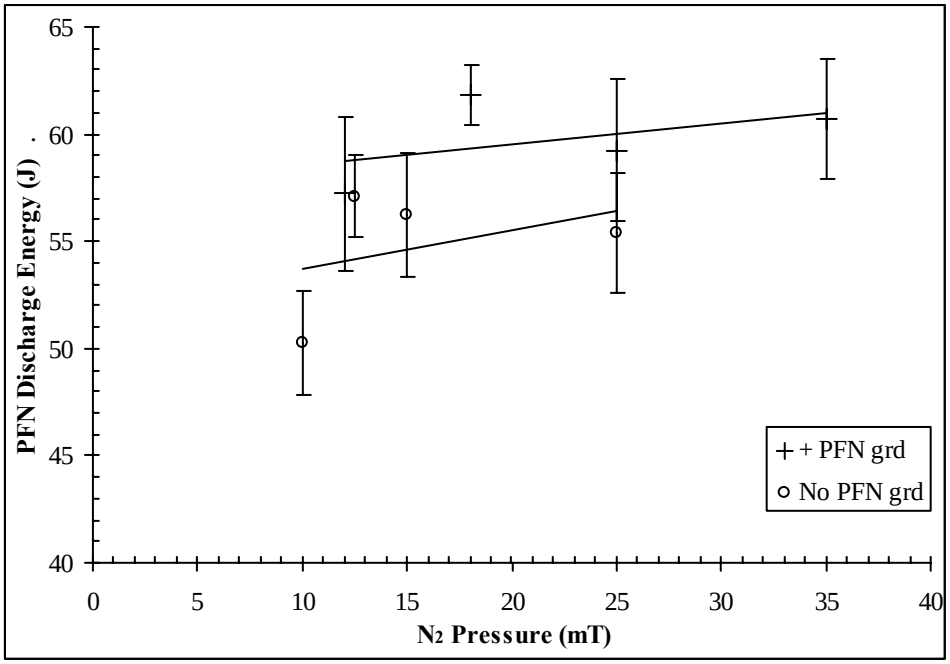

Figure 2.47. PFN discharge energy imparted to the plasma system for different PFN ground options in different nitrogen pressures.

2.4.5. PFN Dependence on Initial Voltage

This section describes the arc discharge through investigations of the current pulses generated during the plasma arc discharge with different initial voltages (V_i) applied to the capacitive stage of the PFN. The system was operated with argon and nitrogen atmospheres and an ambient pressure of 12.5 mTorr, and a PFN capacitance of 39 mF. The PFN initial voltage was varied from 70 VDC to 100 VDC.

It was observed that the characteristics of the current pulse discharge, V_f, $FWHM_I$, I_P, and E_C, are dependent on the PFN initial voltage. The current pulse discharge characteristics changed linearly for the argon atmosphere, while the characteristics changed non-linearly for the nitrogen atmosphere within this initial voltage range. For the nitrogen atmosphere the PFN discharged to an average of 20.6 V for initial voltages of 80 V and greater. During these conditions the plasma discharge would arc between the electrodes causing micro-discharges, not the distributed arc discharge that was desired. These micro-discharge arcs caused visible particles within the plasma, an undesirable effect which can result in large particulates in the deposited film. Due to the arcing of the nitrogen plasma discharge the total discharge energies are greater than those of the argon plasma, unlike the results seen in Section 2.4.3. for total discharge energy as a function of atmosphere pressure.

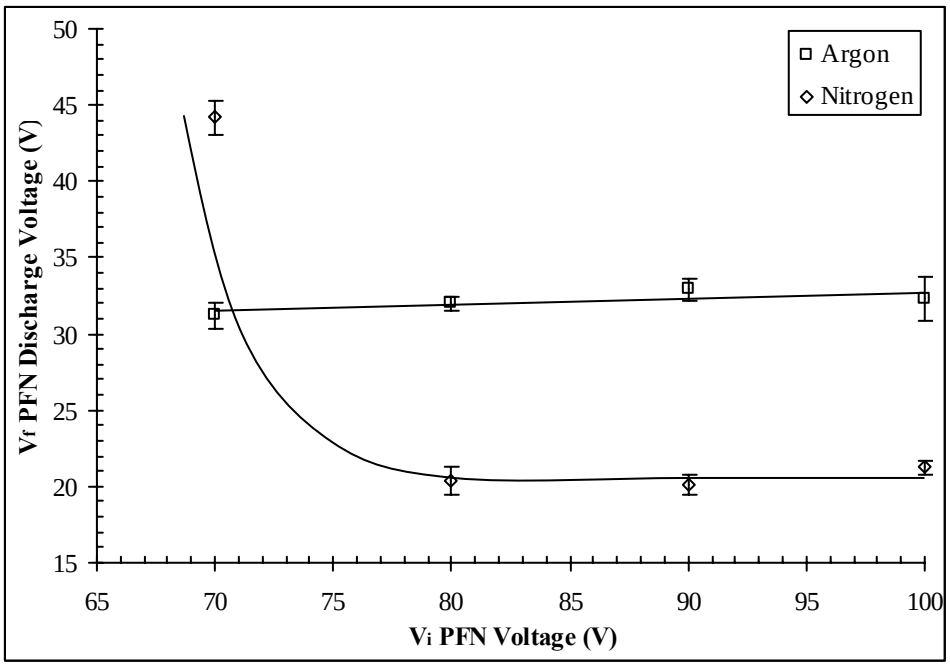

Figure 2.48. PFN final discharge voltage obtained at different PFN initial voltages for argon and nitrogen ambients.

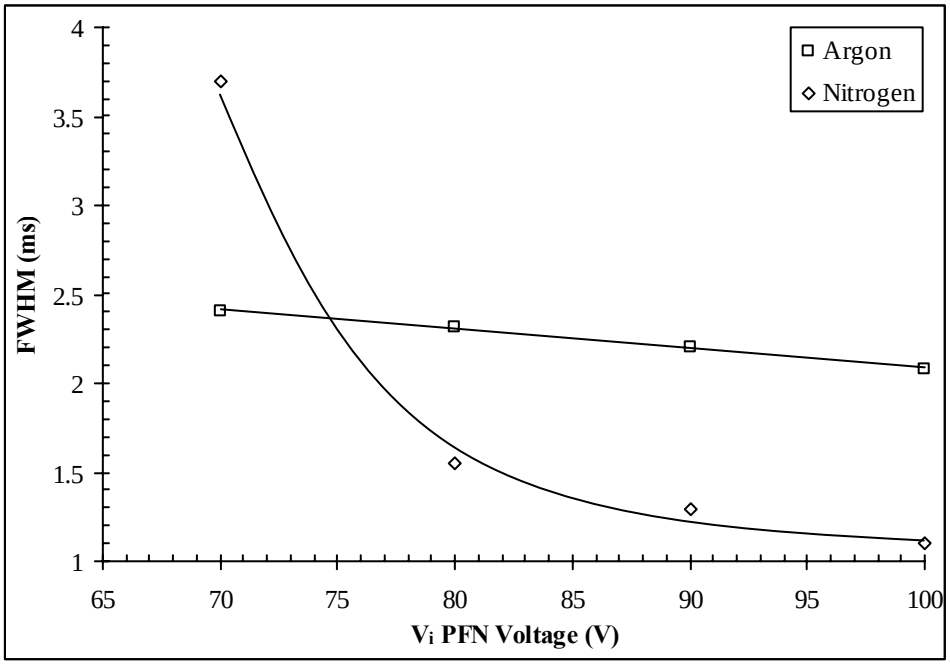

Figure 2.49. Current pulse FWHM obtained at different PFN initial voltages for argon and nitrogen ambients.

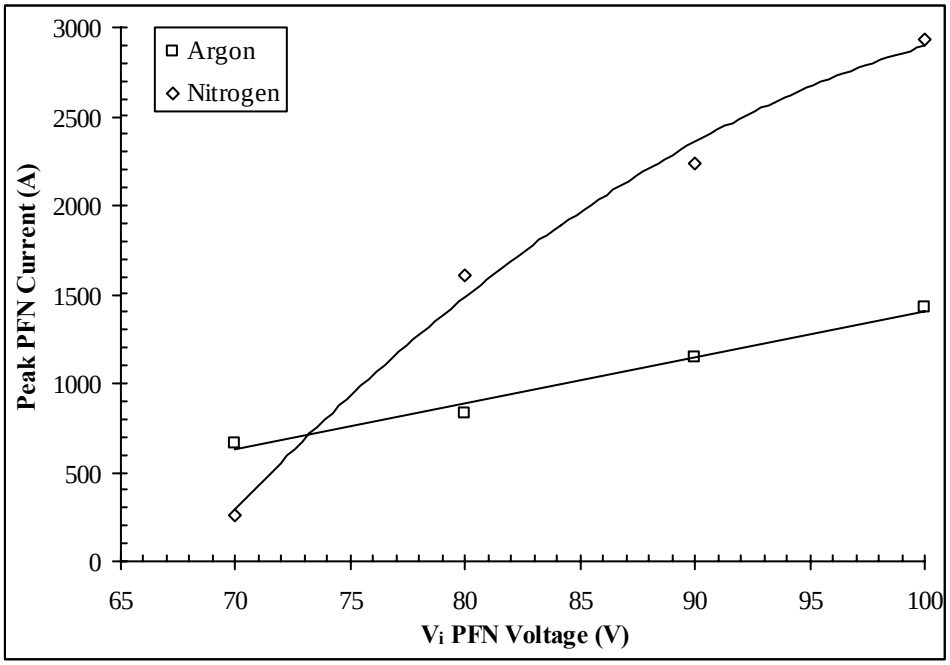

Figure 2.50. PFN peak currents calculated for different PFN initial voltages for argon and nitrogen ambients.

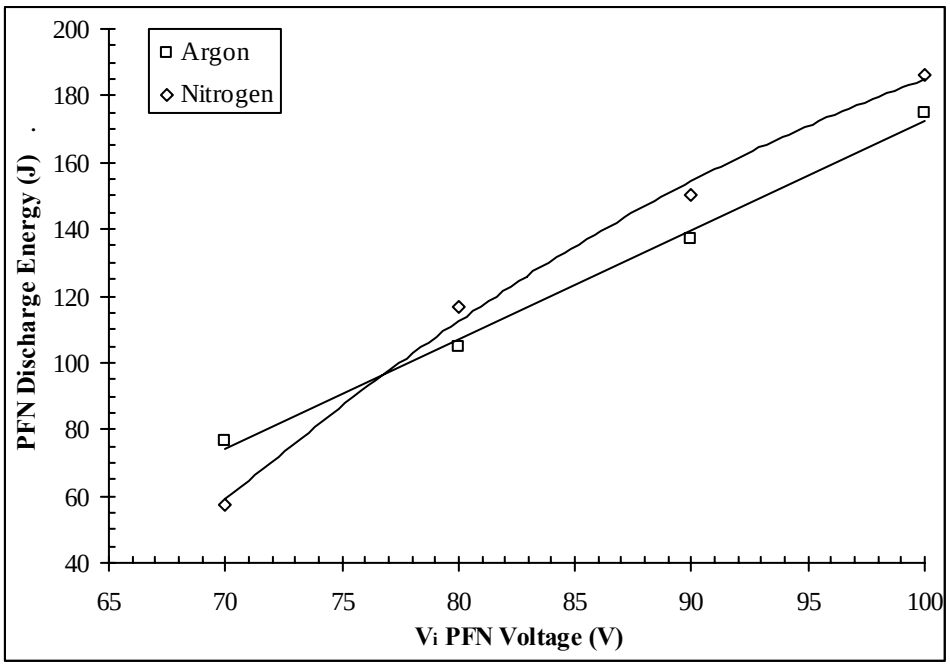

Figure 2.51. PFN discharge energy imparted to the plasma system for different PFN initial voltages for argon and nitrogen ambients.

2.4.6. PFN Dependence on Capacitance

This section describes the arc discharge through investigations of the current pulses generated during the plasma arc discharge with six different values for the capacitive stage of the PFN. The total PFN capacitance was varied using capacitors connected in parallel, as shown in Figure 2.2., to achieve values of 3.9mF, 7.8mF, 15.6mF, 23.4mF, 31.2mF, and 39 mF. The system was operated with argon and nitrogen gases at a constant ambient pressure of 15 mTorr. A voltage of 100 VDC was used as the PFN initial voltage.

The investigations found that in the presence of both the argon and nitrogen ambient gases, that as the capacitance was increased, the FWHM of the current pulse, peak current, and total discharge energy increased, as shown in Figure 2.53. through Figure 2.55. The PFN final discharge voltage decreased with increasing capacitance, as shown in Figure 2.52.

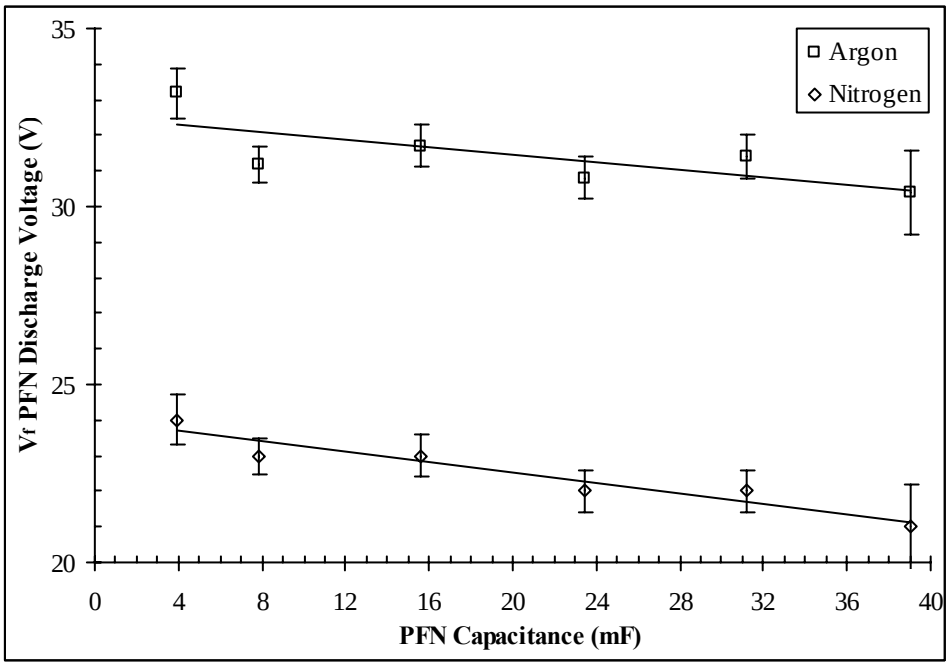

Figure 2.52. PFN final discharge voltage obtained for different PFN capacitances for argon and nitrogen ambients.

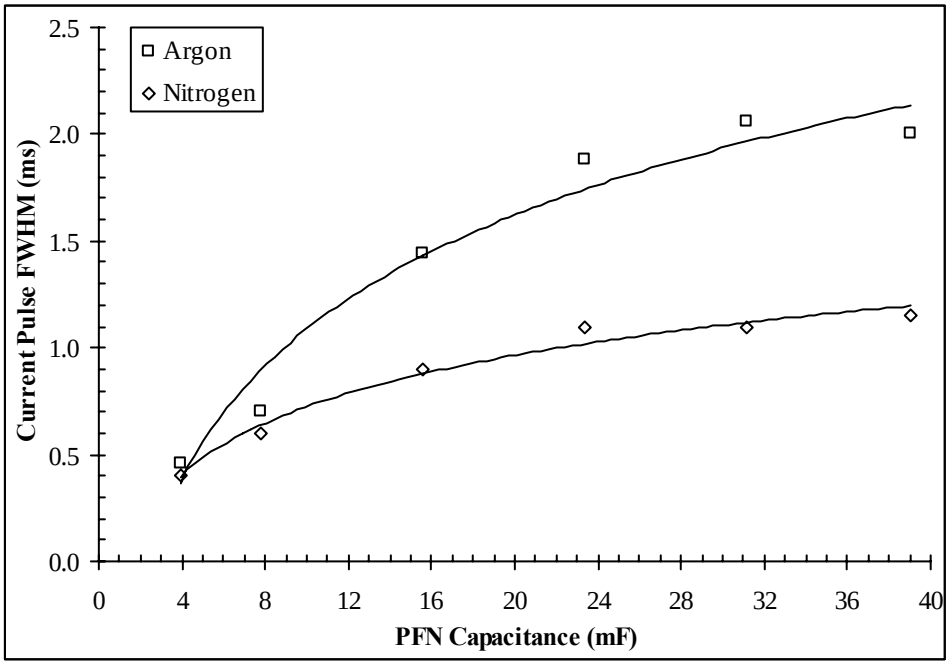

Figure 2.53. Current pulse FWHM obtained for different PFN capacitances for argon and nitrogen ambients.

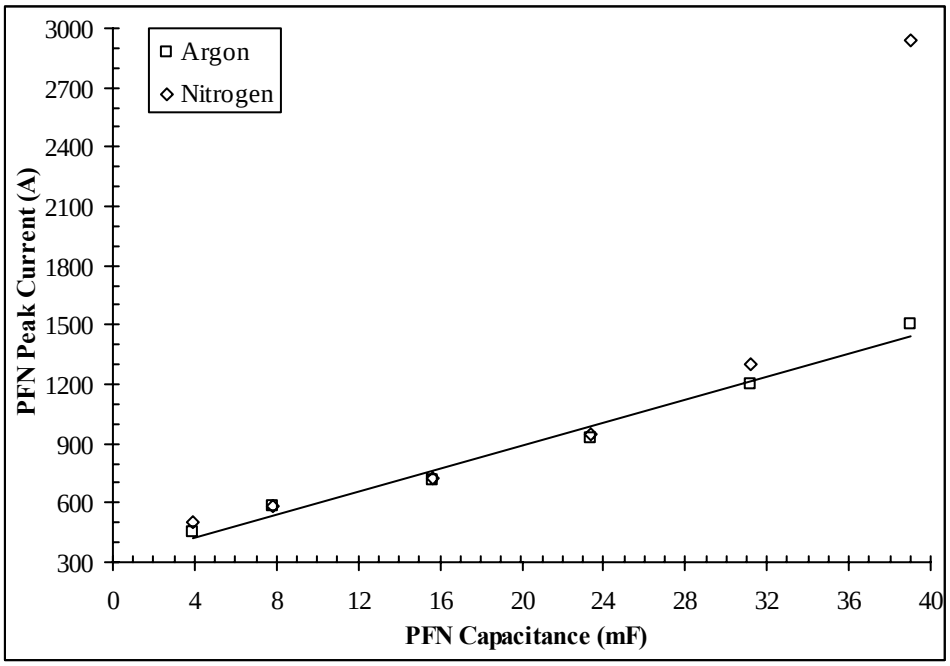

Figure 2.54. PFN peak currents calculated for different PFN capacitances for argon and nitrogen ambients.

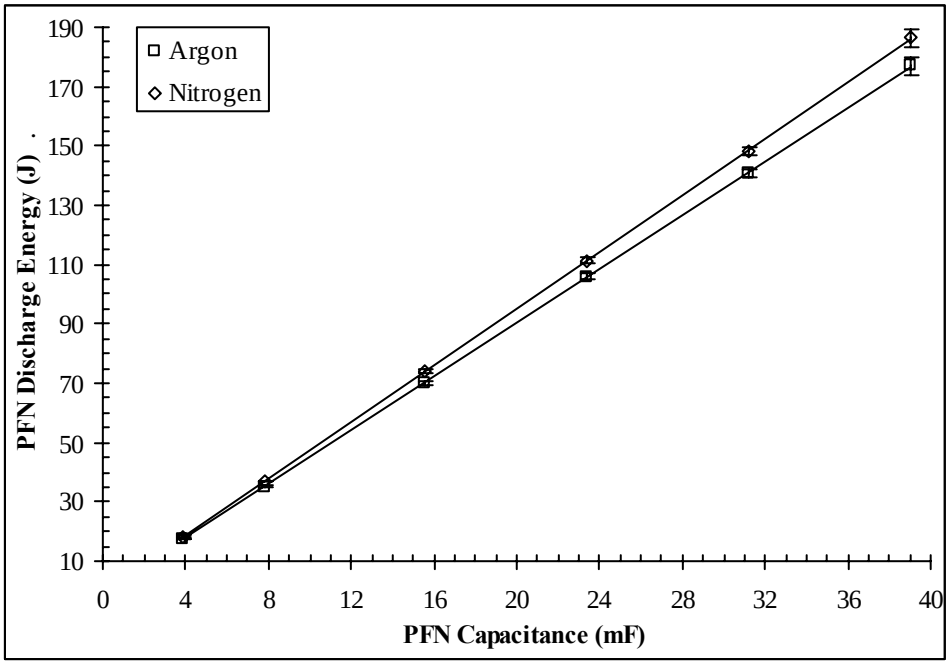

Figure 2.55. PFN discharge energy imparted to the plasma system for different PFN capacitances for argon and nitrogen ambients.

2.4.7. PFN Dependence on Inductance

This section describes the arc discharge through investigations of the current pulses generated during the plasma arc discharge with seven different values for the inductor stage of the PFN. The PFN inductor was varied using inductors in series which totaled 10 μH, 53.2 μH, 172 μH, 770 μH, 1180 μH, 2530 μH, and 5000 μH, as shown in Figure 2.2. The system was operated with argon gas at a constant ambient pressure of 15mTorr. PFN initial voltages of 70 VDC and 100 VDC were investigated, and the PFN capacitance was 39mF.

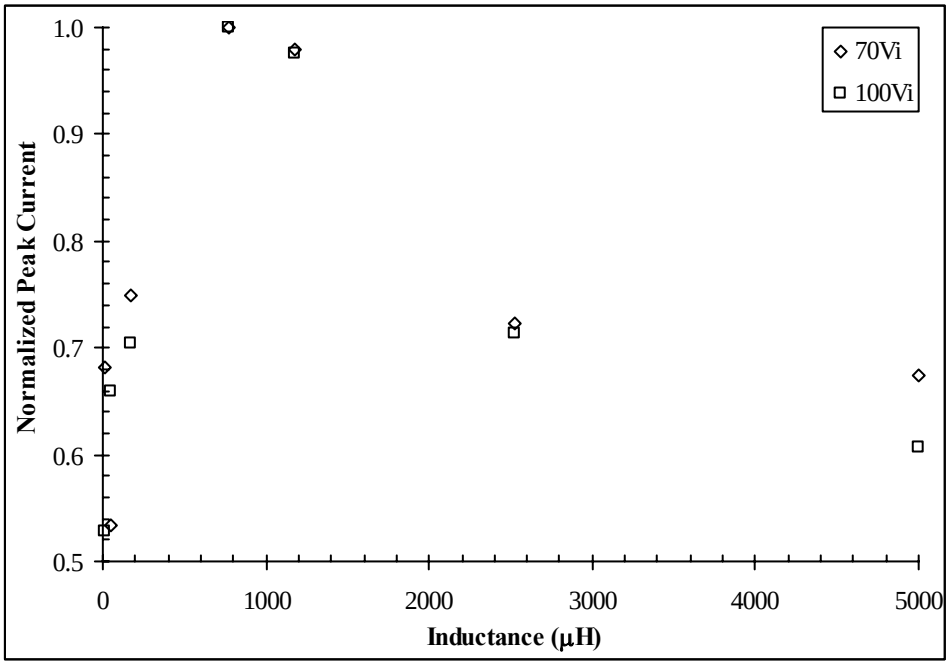

Figure 2.56. Normalized PFN peak current calculated for different PFN inductors for PFN initial voltages of 70V and 100V.

For both PFN initial voltages of 70 VDC and 100 VDC a peak in the peak current occurred with the 770 μH inductor, as shown in Figure 2.56. The PFN peak currents were normalized in order to compare the currents produced by the 70 VDC and 100 VDC

conditions. The current reached the maximum value when the frequency of the applied voltage matched the natural oscillator frequency, or resonant frequency, ω_o. At the resonant frequency of the plasma discharge system the current through the circuit is in phase with the driving voltage. The peak current occurred when the impedance of the system was at its lowest.

2.4.8. Summary

In summary, the discharge characteristics of the PFN are affected by multiple variables. The characteristics typically monitored to describe the discharge of the PFN are the PFN final discharge voltage (V_f), the current pulse $FWHM_I$, the peak discharge current (I_p), and the total discharge energy (E_C). The fluence of the triggering CO_2 laser incident on the cathode does not significantly affect the PFN characteristics. The type and pressure of the ambient gas does affect the PFN discharge. At pressures lower than 12 mtorr the discharge changes significantly, but at pressures greater than 12 mtorr the characteristics of the PFN discharge remain relatively constant even to pressures of a few hundred mtorr. The PFN discharge is dependent on the initial voltage and capacitance of the PFN and the gas type. For nitrogen, non-distributed arcing in the form of micro-discharges occurred for initial PFN voltages greater than 70 VDC. These micro-discharges caused visible macro-particles in the plume, an undesirable effect that a distributed arc is to minimize. The total capacitance of the PFN allows high discharge energies to be achieved but caused micro-discharges when nitrogen was used as the ambient. The value of the inductor stage in the PFN created a maximum in the discharge current, and therefore total discharge energy, when an inductor of 770 μH was used.

CHAPTER 3. LASER-TRIGGERED HOLLOW-ELECTRODE PULSED PLASMA FLIM DEPOSITION: MATERIALS AND FILM GROWTH

This chapter serves to characterize the thin films deposited by the laser-triggered hollow-electrode pulsed plasma technique. The source and composition of the deposited material is investigated including characterization by deposition rate and surface morphology. Also, the effects of an applied magnetic field to the plasma and optical diagnostics of the discharge are examined.

3.1. Source of Deposited Material

This section describes the source of the deposited material, as from the rod-electrode or the hollow-electrode. Determining the origin of the material should lead to the mechanism of the vaporization, electron or ion bombardment. The electrode materials were varied and mixed and the deposited films were examined by energy dispersive X-ray spectroscopy (EDS) to determine the composition of the resulting films.

EDS is a standard procedure for identifying and quantifying the elemental composition of sample volumes as small as a few cubic micrometers. Characteristic X-rays are produced when a material is bombarded with electrons in an electron beam instrument, such as a scanning electron microscope (SEM). As the electron beam of the SEM is scanned across the sample surface, it generates X-ray fluorescence from the atoms in its path. Detection of these x-rays is accomplished by an energy dispersive

spectrometer, a solid state device that discriminates among X-ray energies. When an X-ray photon hits the detector, it creates electron-hole pairs that drift due to the high voltage in the detector. The electric charge is collected, and is proportional to the energy of the photon. It is thus possible to determine the energy spectrum. Electronic noise is reduced by cooling the detector with liquid nitrogen. The energy of each X-ray photon is characteristic of the element which produced it. The EDS microanalysis system collects the X-rays, sorts by polarization, plots them by energy, and automatically identifies and labels the elements responsible for the peaks in this energy distribution. Most elements are detected at concentrations of ~ 0.1%. A reference for the electron binding energies of the elements argon, carbon, copper, nitrogen, oxygen, silicon, and titanium is shown in Table 3.1. These are the dominant elements that are expected to be found in the deposited films.

3.1.1. Experimental Setup

The initial experiments were conducted using the hollow-cathode configuration, as shown in Figures 2.4. and 2.5. The PFN was operated at an initial voltage of 100V with an inductance of 770 μH and a total capacitance of 39 mF. The vacuum chamber was evacuated and back filled with nitrogen to a pressure of 12.5 millitorr. The triggering CO_2 laser was operated at 1Hz and a fluence of 176.3 mJ/mm^2 ± 3.2 mJ/mm^2 using the single spatial mode with single longitudinal mode laser.

Two variations of the hollow-cathode configuration were used; one with a carbon hollow-cathode and copper rod-anode, and the other with a copper hollow-cathode and carbon rod-anode. After the deposited films are characterized using EDS the source of the deposited material can be determined.

Element	Label	Orbital	Energy (keV)
Ar	K	1s	3.2059
	L_I	2s	0.3262
	L_{II}	$2p_{1/2}$	0.2506
	L_{III}	$2p_{3/2}$	0.2484
	M_I	3s	0.0293
	M_{II}	$3p_{1/2}$	0.0159
	M_{III}	$3p_{3/2}$	0.0157
C	K	1s	0.2842
Cu	K	1s	8.979
	L_I	2s	1.0967
	L_{II}	$2p_{1/2}$	0.9523
	L_{III}	$2p_{3/2}$	0.9327
	M_I	3s	0.1225
	M_{II}	$3p_{1/2}$	0.0773
	M_{III}	$3p_{3/2}$	0.0751
N	K	1s	0.4099
	L_I	2s	0.0373
O	K	1s	0.5431
	L_I	2s	0.0416
Si	K	1s	1.839
	L_I	2s	0.1497
	L_{II}	$2p_{1/2}$	0.0998
	L_{III}	$2p_{3/2}$	0.0992
Ti	K	1s	4.966
	L_I	2s	0.5609
	L_{II}	$2p_{1/2}$	0.4602
	L_{III}	$2p_{3/2}$	0.4538
	M_I	3s	0.0587
	M_{II}	$3p_{1/2}$	0.0326
	M_{III}	$3p_{3/2}$	0.0326

Table 3.1. Electron binding energies reference for the elements argon, carbon, copper, nitrogen, oxygen, silicon, and titanium.

3.1.2. Composition of the Deposited Material

Films were deposited using an average total PFN discharge energy of 105.8 ± 14.1 J. The resulting film thickness for the carbon hollow-cathode and copper rod-anode configuration was 2400 Å, and film thickness for the copper hollow-cathode and carbon rod-anode configuration was 3900 Å.

An acceleration voltage of 4 kV was used to examine the films because the thicknesses are relatively thin for EDS analysis. If the acceleration voltage is too high and a signal from the substrate is detected then secondary emission can cause the film composition percentages to be artificially high. The two films were examined by EDS and the composition spectrum for the carbon hollow-cathode and copper rod-anode configuration is shown in Figure 3.1. The spectrum shows a predominant peak at 0.28 keV, corresponding to the carbon K 1s orbital, and a minor peak at 0.99 keV, corresponding to the copper L_I 2s through L_{III} $2p_{3/2}$ orbital, as shown in Table 2.2. The EDS quantification of the film shows 62.15% of carbon and only 1.02% of copper by atomic weight, as shown in Table 3.2. The significant material source for this electrode configuration is from the carbon hollow-cathode.

The composition spectrum for the copper hollow-cathode and carbon rod-anode configuration is shown in Figure 3.2. The spectrum shows a predominant peak at 0.96 keV, corresponding to the copper L_I 2s through L_{III} $2p_{3/2}$ orbital, and a minor peak at 0.27 keV, corresponding to the carbon K 1s orbital, as shown in Table 3.1. The EDS quantification of the film shows 62.55% of copper and 25.52% of carbon by atomic weight, as shown in Table 2.4. The significant material source for this electrode configuration is from the copper hollow cathode.

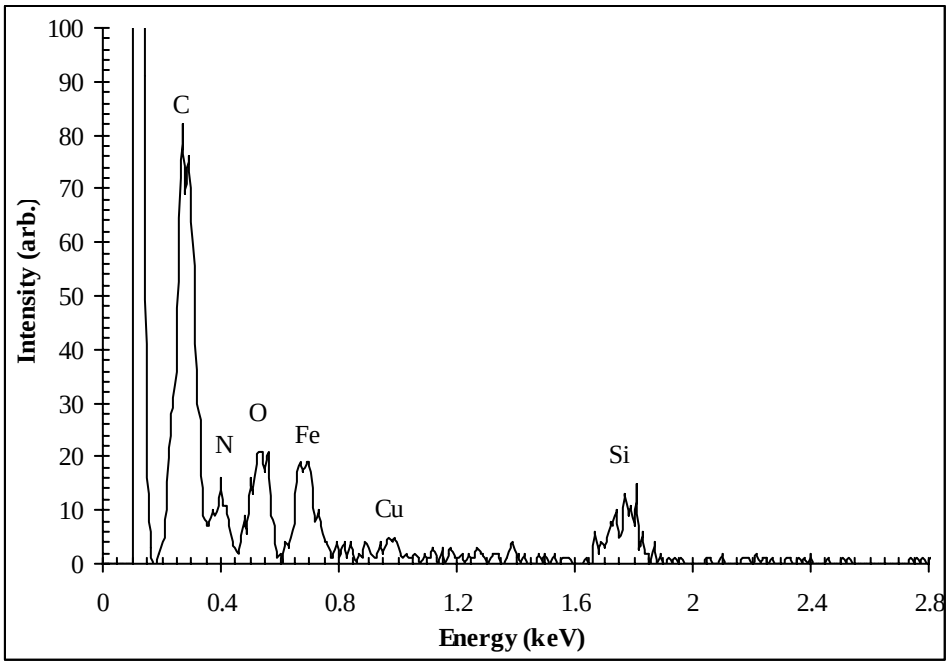

Figure 3.1. EDS composition spectrum of a film deposited with the laser triggered, carbon hollow-cathode system.

Element	Wt %	At %
C K	41.37	62.15
N K	8.86	11.41
O K	8.14	9.19
Fe L	25.71	8.31
Cu L	3.59	1.02
Si K	12.33	7.92
Total	100.00	100.00

Table 3.2. EDS quantification of a film deposited by a carbon hollow-cathode system.

The source of the material deposited in the thin films was found to have originated predominantly from the cathode, although there exists cross contamination of material from the anode. The significant mechanism for the removal of material from the electrodes can be determined to be by ions sputtering the cathode and not electrode bombardment of the anode. At this energy level the rod-anode becomes red hot due to the

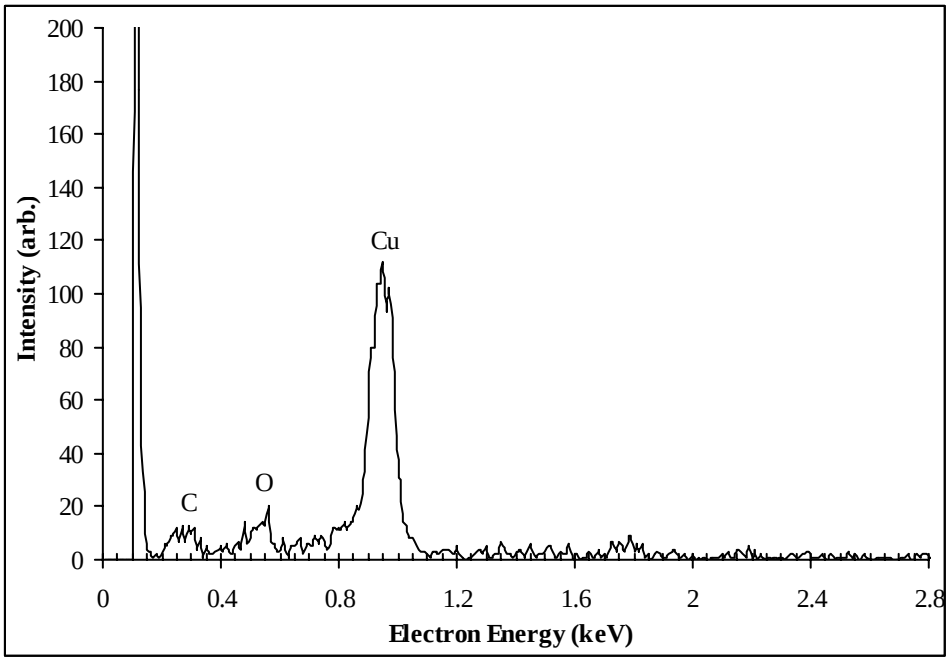

Figure 3.2. EDS composition spectrum of a film deposited with laser triggered, copper hollow-cathode system.

Element	Wt %	At %
C K	6.85	25.52
O K	4.27	11.94
Cu L	88.87	62.55
Total	99.99	100.01

Table 3.3. EDS quantification of a film deposited by a copper hollow-cathode system.

electron bombardment. The film deposited using the hollow-anode configuration was much thicker for the same number of pulses because of the differences in the physical properties of the carbon and copper electrodes. The melting point of copper is much lower than that of carbon, and it can be sputtered more effectively.

3.2. Characterization of the Thin Films Deposited

In this section the details of the deposition and characterization of carbon thin films deposited by hollow-electrode transient plasma discharge are discussed. The goal is to investigate the process's ability to produce large area films with a high rate of deposition and compare the results of the films deposited in the presence of argon and nitrogen as the ambient gas. Large area film deposition was defined as complete coverage of a 3 inch diameter silicon wafer, as compared to the coverage achieved by single laser PLD. The deposition rate was compared to single laser PLD also, with a goal of 12 to 18 Å/pulse. Films deposited using hollow-cathode and hollow-anode configurations were compared as well. SEM micrographs of the films deposited are also presented as part of the film morphology studies.

3.2.1. Thin Film Preparation

In order to compare the deposition rate of the evaporated materials and the large area uniformity of the films grown in argon and nitrogen plasmas, the films were grown on substrates of silicon chips 1 cm^2, or larger, for on-axis film thickness measurements, and then on 3-inch diameter silicon wafers for radial film thickness measurements using both types of hollow-electrode configurations, as shown in Figures 2.5. and 2.7. An aluminum block attached to a rod made of the same material was used as the substrate holder.

Silicon substrates with (100) orientation were first cleaned using the standard cleaning procedure: 15 minutes of ultrasonic agitation in acetone followed by 15 minutes of ultrasonic agitation in methanol. The wafers were then rinsed with de-ionized water and dried with a flow of compressed nitrogen. The cleaned substrate was then fixed to the

front surface of the substrate holder with a cleaned stainless steel sheet acting as a mask and fitted inside the deposition chamber such that the substrate was positioned symmetrically in front of the hollow electrode with the line of the mask perpendicular to the center line of the hollow electrode (see Figures 2.4. and 2.6.). The substrate to electrode distance was kept at 6 centimeters.

The conditions for the on-axis film thickness trials were that the PFN initial voltage was set at 100 VDC and the PFN capacitance was varied to control the PFN total discharge energy, using 3.9 mF, 7.8 mF, 15.6 mF, 23.4 mF, 31.2 mF, and 39 mF capacitors. The background gas pressure was set at 15 mTorr for each gas type. The triggering CO_2 laser was operated at 1 Hz. The conditions for the radial film thickness trials were the same as the on-axis trials but the PFN capacitance was set at 31.2 mF. The substrate was protected behind a shutter during the first minute of discharges to ensure the process was operating properly. The shutter was then moved away to begin the deposition on the substrate and was carried out for a set number of pulses at 1 Hz.

3.2.2. Film Thickness Measurements

The on-axis and radial film thickness measurements of the films deposited by argon and nitrogen plasmas for the hollow-cathode and hollow-anode configurations were obtained using a surface texture profilometer (Dektak 3030 ST). The step height produced by the removable mask is measured by a stylus in contact with, and gently dragging along, the surface of the substrate. The on-axis deposition rate, Δd, was then calculated by dividing the on-axis film thickness by the total number of pulses discharged during the trial.

The results for the on-axis film thickness depositions for varied PFN discharge energies produced energies in the range of 15 J to 187 J for both electrode configurations and gases. An example of the film thickness per pulse is shown in Figure 3.3. for an argon ambient and the hollow-cathode configuration. For each of the combinations of gas and electrode configurations, the same characteristics were found;

1. below a certain PFN discharge energy there was no deposition of material,
2. there is an upper limit to the discharge energy where the discharge became erratic forming micro-discharges causing a wide range of deposition rates, and
3. in the stable region of the discharge energy, the deposition rate is fairly linear.

For the argon ambient and the hollow-cathode configuration, there was no deposition of material below a discharge energy of approximately 70 J, the upper limit was 175.0 ± 2.6 J producing a wide range of deposition rates with an average of 1.5 ± 0.5 Å/pulse. The rate of change is given by the slope of the linear region, in terms of the deposition rate per discharge energy, $\Delta d/E_C$, in units of (Å/pulse)/J. The equation of the trend line for the linear region was found to be;

$$y = 0.0031x - 0.2016 \qquad [3.1]$$

then,

$$\left(\frac{\Delta d}{E_C}\right)_{\text{arg}\,on-cathode} = 0.0031 \qquad [3.2]$$

The statistics for the other three configurations are given in Table 3.1. As can be seen, the average minimum discharge energy where deposition did not occur was 61 ± 5 J. The maximum discharge energy that could be achieved is consistent between the gas types and electrode configurations, at 179 ± 4 J. The maximum discharge energy for the nitrogen ambient is slightly higher than that of argon; however, it is not significantly

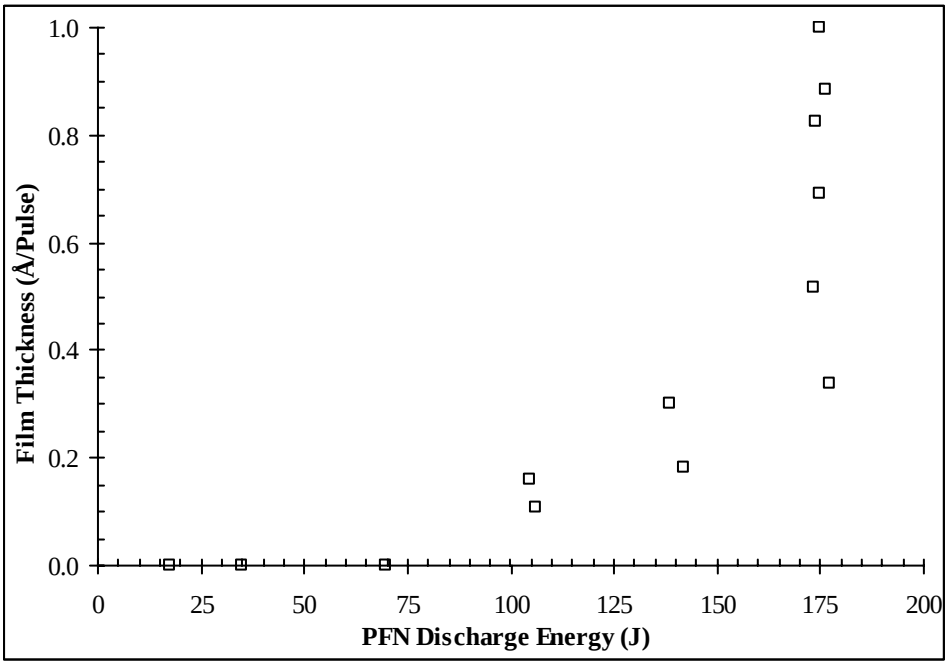

Figure 3.3. The on-axis carbon film thickness measurements per pulse obtained for different PFN total discharge energies deposited in argon ambient using the hollow-cathode configuration.

Gas	Electrode Configuration	Saturation Energy (J)	Saturation Deposition Rate (Å/pulse)	Minimum Energy (J)	Equation	$\Delta d/E_C$ (Å/pulse)/J
Ar	Hollow-cathode	175.0 ± 2.6	1.5 ± 0.5	65.0	y=0.0031x-0.2016	0.0031
N	Hollow-cathode	181.3 ± 11.7	9.6 ± 4.8	55.9	y=0.0147x-0.8221	0.0147
Ar	Hollow-anode	175.1 ± 2.8	0.7 ± 0.3	65.7	y=0.0063x-0.4141	0.0063
N	Hollow-anode	182.8 ± 10.9	10.7 ± 4.1	59.0	y=0.0307x-1.801	0.0307

Table 3.4. The statistics for on-axis film thickness per pulse using various gas and electrode configurations.

different due to the larger standard deviation of the discharge energy produced with the nitrogen plasma. The rate of change given by the slope of the linear region, $\Delta d/E_C$, does depend on the gas type and electrode configuration. The on-axis deposition rate to discharge energy ratio is lowest for the argon ambient hollow-cathode, and highest for the nitrogen ambient hollow-anode configuration. For the hollow-cathode configuration the $\Delta d/E_C$ ratio of the nitrogen to argon ambient is;

$$\frac{\left(\frac{\Delta d}{E_C}\right)_{N-cathode}}{\left(\frac{\Delta d}{E_C}\right)_{Ar-cathode}} = \frac{0.0147}{0.0031} = 4.74 \qquad [3.3]$$

and for the hollow-anode configuration the $\Delta d/E_C$ ratio of the nitrogen to argon ambient is;

$$\frac{\left(\frac{\Delta d}{E_C}\right)_{N-anode}}{\left(\frac{\Delta d}{E_C}\right)_{Ar-anode}} = \frac{0.0307}{0.0063} = 4.87 \qquad [3.4]$$

Therefore, the deposition rate per discharge energy between the two types of electrode configurations is similar and the nitrogen plasma rate is approximately 4.8 times greater than that of the argon plasma.

For the argon ambient the $\Delta d/E_C$ ratio of the hollow-anode to hollow-cathode configurations is;

$$\frac{\left(\frac{\Delta d}{E_C}\right)_{Ar-anode}}{\left(\frac{\Delta d}{E_C}\right)_{Ar-cathode}} = \frac{0.0063}{0.0031} = 2.03 \qquad [3.5]$$

For the nitrogen ambient the $\Delta d/E_C$ ratio of the hollow-anode to hollow-cathode configurations is;

$$\frac{\left(\frac{\Delta d}{E_C}\right)_{N-anode}}{\left(\frac{\Delta d}{E_C}\right)_{N-cathode}} = \frac{0.0307}{0.0147} = 2.09 \qquad [3.6]$$

Therefore, the deposition rate per discharge energy between the two types of ambient gas is similar and the hollow-anode electrode configuration rate is approximately 2 times greater than that of the hollow-cathode electrode configuration.

The geometry of the hollow-electrode discharge head is as shown in Section 2.1.1. and Figure 2.1. The inside diameter of the hollow-electrode is 11.7 mm and 7.5 mm of the length is exposed to the rod-electrode. The hollow-electrode area that is exposed is:

$$A_{hollow} = \left(2\pi R_{hollow}\right) \cdot \ell_{hollow} = 275.7 mm^2 \qquad [3.7]$$

The diameter of the rod-electrode is 6.25 mm and 7.5 mm of the length is exposed to the inside of the hollow-electrode. The rod-electrode area that is exposed is:

$$A_{rod} = \left(2\pi R_{rod}\right) \cdot \ell_{rod} = 147.3 mm^2 \qquad [3.8]$$

The ratio of the hollow-electrode to rod-electrode exposed area is;

$$\frac{A_{hollow}}{A_{rod}} = 1.9 \qquad [3.9]$$

So, the hollow-electrode area is approximately twice the area of the rod-electrode. The electrode area ratio is similar to the deposition rate per discharge energy, as shown in equations 3.5 and 3.6. The deposition rates that were achieved are related to the geometry of the electrodes. Assuming that the discharge energy is evenly distributed over the exposed area of the electrode, the energy of the plasma ions that strike the cathode would have twice the density for the hollow-anode configuration as for the hollow-cathode configuration. This lends support to the results given in equations 3.5 and 3.6, where for either gas type, the deposition rate per discharge energy was approximately doubled when the rod-electrode was the cathode being bombarded by the positively charged plasma ions. When the discharge energy reached the upper limit and non-distributed

arcing was observed in the form of micro-discharges, the energy density would not be evenly distributed over the surface of the electrode. Instead, the discharge would form multiple micro-discharge arcs increasing the energy density to individual locations and cause greater deposition rates. These multiple micro-discharges would also be described by the large variation in the deposition rates that occurred when the energy reached approximately 179 J, as shown in Table 3.1.

The radial film thickness scans were performed in 2mm steps along two perpendicular axes. Defining the (100) direction as the x-axis, the film thickness measurements were carried out along both the x-axis and y-axis. The thickness measurements were normalized so the profiles could be compared. Figure 3.4. shows the comparison of the x-axis and y-axis film thickness profiles of the film deposited in an argon ambient and using the hollow-cathode configuration. The profiles are very similar displaying the symmetry of the deposition. The other deposition combinations of gas type and electrode configurations had the same x-axis to y-axis symmetry. The comparison of the x-axis and y-axis film thickness profiles for a carbon film deposited by single laser UV PLD in vacuum is shown in Figure 3.5. The profiles are not symmetrical because of the non-symmetrical shape of the laser spot.

Figures 3.6 and 3.7 show the x-axis profile comparison of the films deposited with the hollow-cathode and hollow-anode electrode configurations, respectively, and in argon and nitrogen ambient. In both cases of electrode configurations, the films deposited with the nitrogen plasma are more forward-directed than that of the argon plasma. Forward-directed depositions have higher on-axis thicknesses as compared to distances further from the center. The films deposited in argon have a flatter or more even

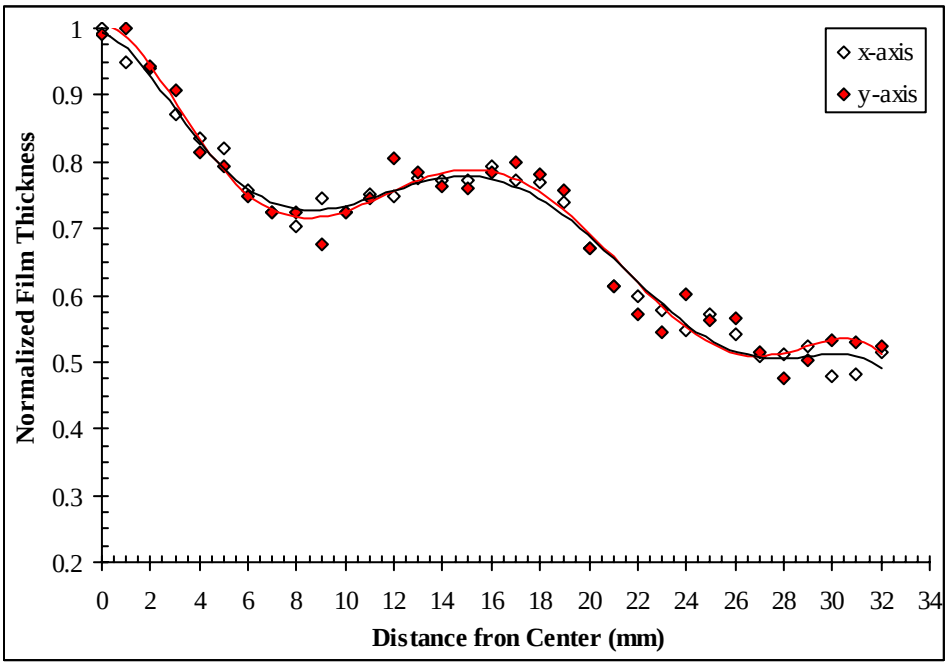

Figure 3.4. Normalized film thickness x-axis and y-axis radial profiles of a carbon film deposited in argon using the hollow-cathode configuration.

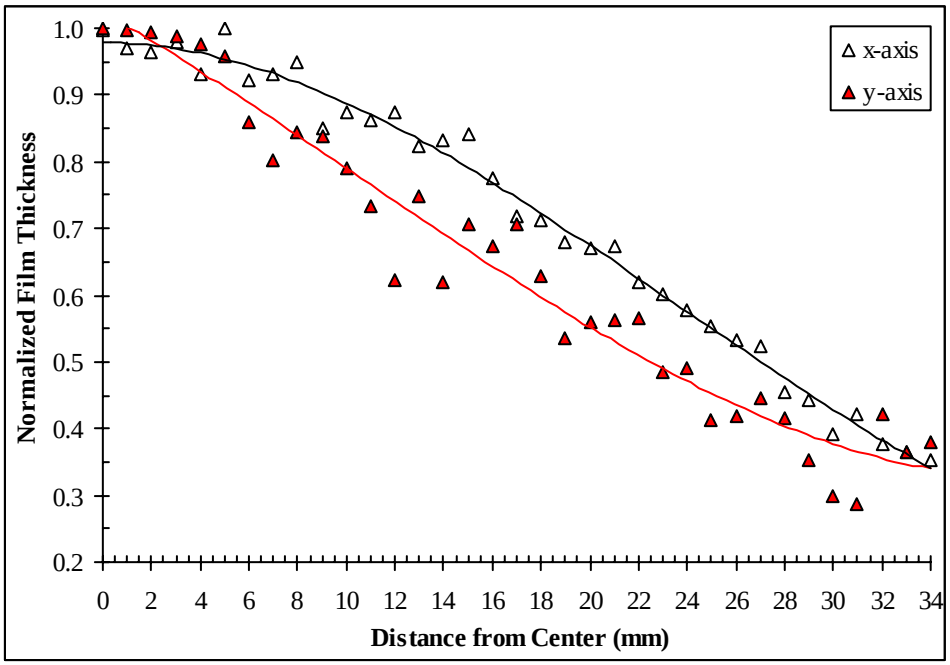

Figure 3.5. Normalized film thickness x-axis radial profiles for a carbon film deposited in vacuum using PLD.

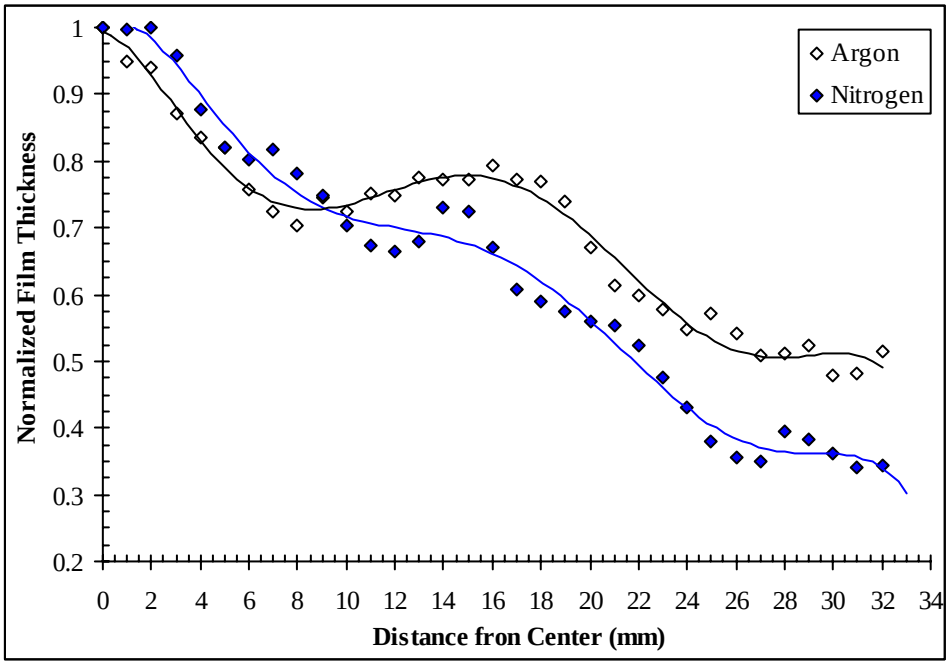

Figure 3.6. Normalized film thickness x-axis radial profiles of carbon films deposited in argon and nitrogen using the hollow-cathode configuration.

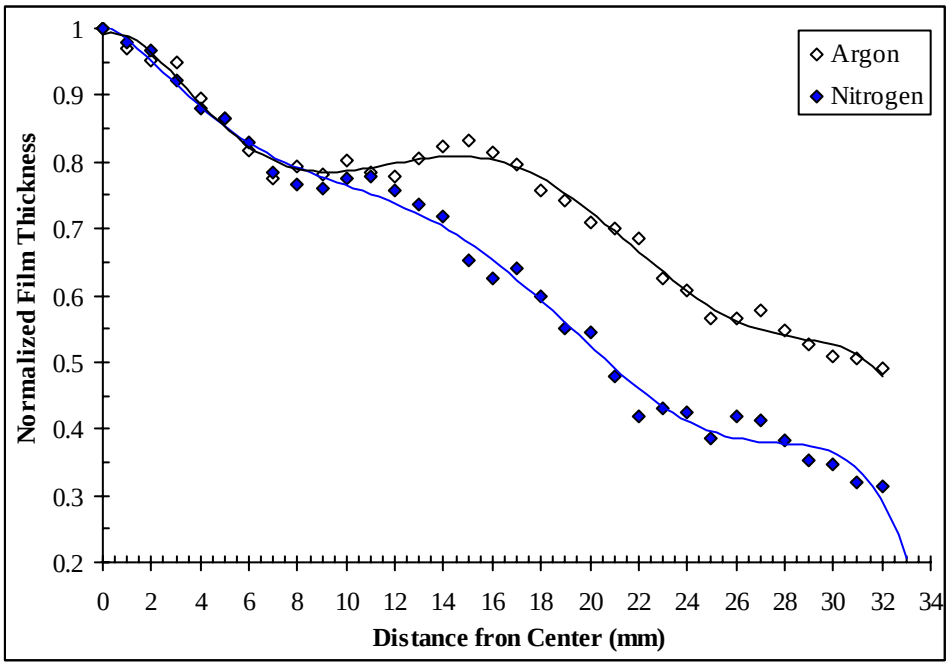

Figure 3.7. Normalized film thickness x-axis radial profiles of carbon films deposited in argon and nitrogen using the hollow-anode configuration.

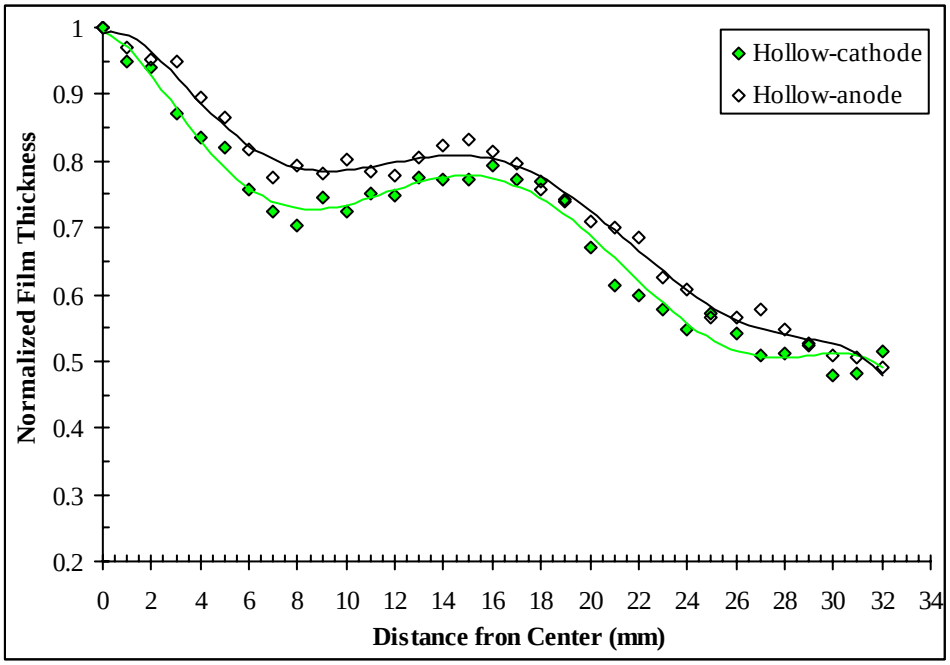

Figure 3.8. Normalized film thickness x-axis radial profiles of carbon films deposited in argon using hollow-cathode and hollow-anode configurations.

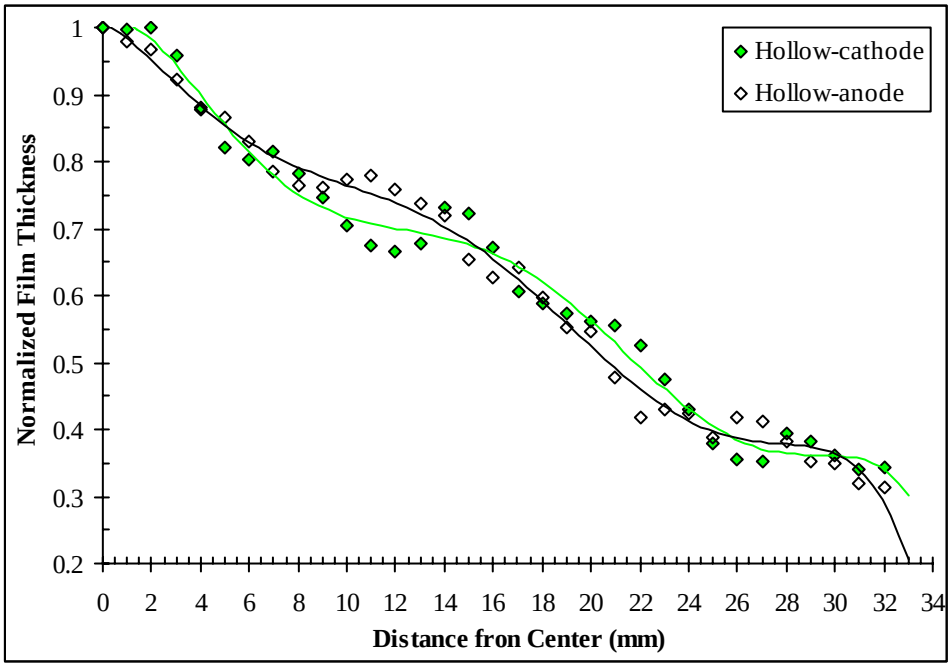

Figure 3.9. Normalized film thickness x-axis radial profiles of carbon films deposited in nitrogen using the hollow-cathode and hollow-anode configurations.

radial profile as compared to the films deposited in nitrogen which are thicker in the center or thinner at distances further from the center of deposition.

Figures 3.8 and 3.9 show the x-axis profile comparison of the films deposited with the argon and nitrogen plasmas, respectively, and by the hollow-cathode and hollow-anode electrode configurations. In either case of the plasma type, the films deposited have similar profiles regardless of the electrode configuration.

In all cases, the coverage of an entire 3-inch wafer was achieved, confirming the capability of large area deposition by this method. Films deposited in argon appeared to be more uniform than corresponding films deposited in nitrogen. The 'humps' that appear in the depositions may be due to the geometry of the discharge head, causing multiple expansion components.

3.2.3. Scanning Electron Microscopy of the Thin Films

Scanning electron microscopy (SEM) examines structure by bombarding the specimen with a scanning beam of electrons and then collecting slow moving secondary electrons that the specimen generates. These are collected, amplified, and displayed on a computer monitor. SEM is typically used to examine the external structure of objects that are as varied as biological specimens, rocks, metals, ceramics and almost anything that can be observed in a traditional light microscope. The SEM has a large depth of field, which allows a large amount of the sample to be in focus at one time. The SEM also produces images of high resolution, which means that closely spaced features can be examined at a high magnification. Preparation of the samples is relatively easy since most SEMs only require the sample to be conductive. The combination of higher magnification, larger depth of focus, greater resolution, and ease of sample observation

makes the SEM one of the most heavily used instruments in morphological materials research.

Based on the previous data, the thickness characteristics of the deposited films do not depend on the type of electrode configuration presented here. It was considered more desirable to have the source material originate from the rod electrode, so the hollow-anode electrode configuration will be used to investigate the surface morphology of the deposited films. The SEM micrographs presented in Figures 3.10 and 3.11 show films deposited using the argon plasma at 104.4 J and 141.9 J respectively. Figures 3.12 and 3.13 show the films deposited using the nitrogen plasma at 107.8 J and 148.4 J, respectively. All of the films contain a low density of irregularly shaped particles and micro-droplets throughout the film surface area, which are 0.5 μm and larger. Micro-particles smaller than 0.5 μm were scarcely found. A low population of large 'flake' particles several microns in size were found which may be due to material build-up on the electrodes which eventually flake off and become deposited on the substrate. The films deposited at higher discharge energies in the nitrogen ambient have a higher particle density than comparable films deposited in argon, as seen in Figure 3.13. Visible particles were observed in the nitrogen plasmas during deposition, possibly due to a film forming on the inside of the hollow-electrode and then flaking off during the deposition.

These were films deposited unaided by shielding and filters. Some of the micro-particles may be eliminated from the deposited film through the use of geometry modifications, shielding being incorporated into the electrodes, and magnetic filtering.

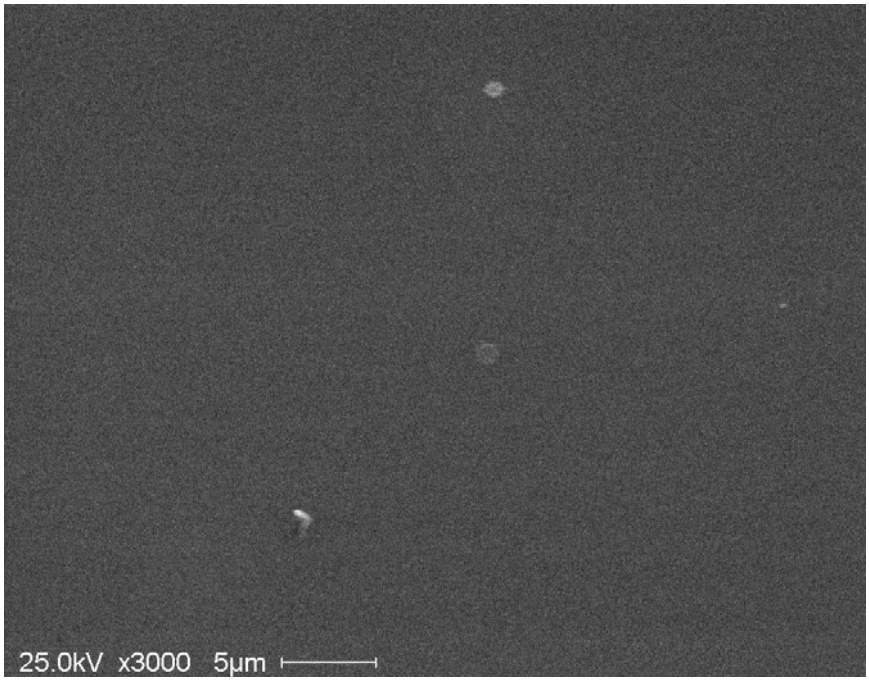

Figure 3.10. SEM micrograph of a carbon film deposited in argon with the hollow-anode configuration at 104.4 J discharge energy.

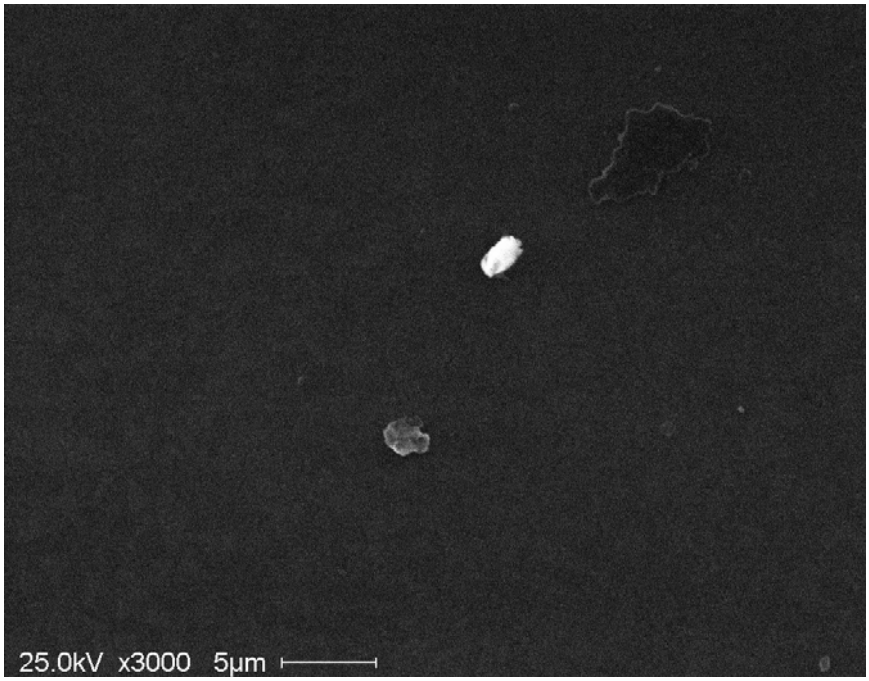

Figure 3.11. SEM micrograph of a carbon film deposited in argon with the hollow-anode configuration at 141.9 J discharge energy.

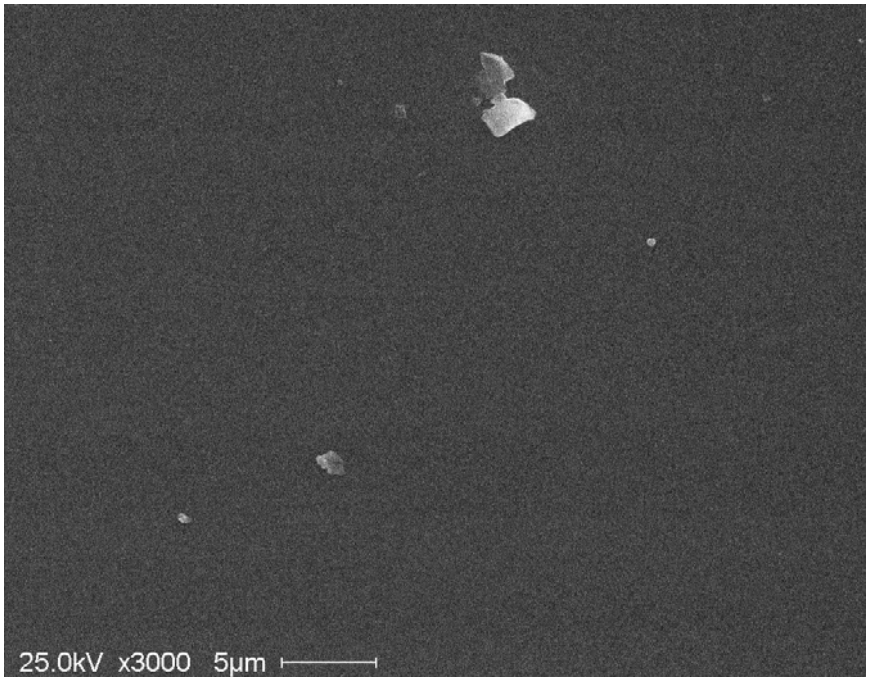

Figure 3.12. SEM micrograph of a carbon film deposited in nitrogen with the hollow-anode configuration at 107.8 J discharge energy.

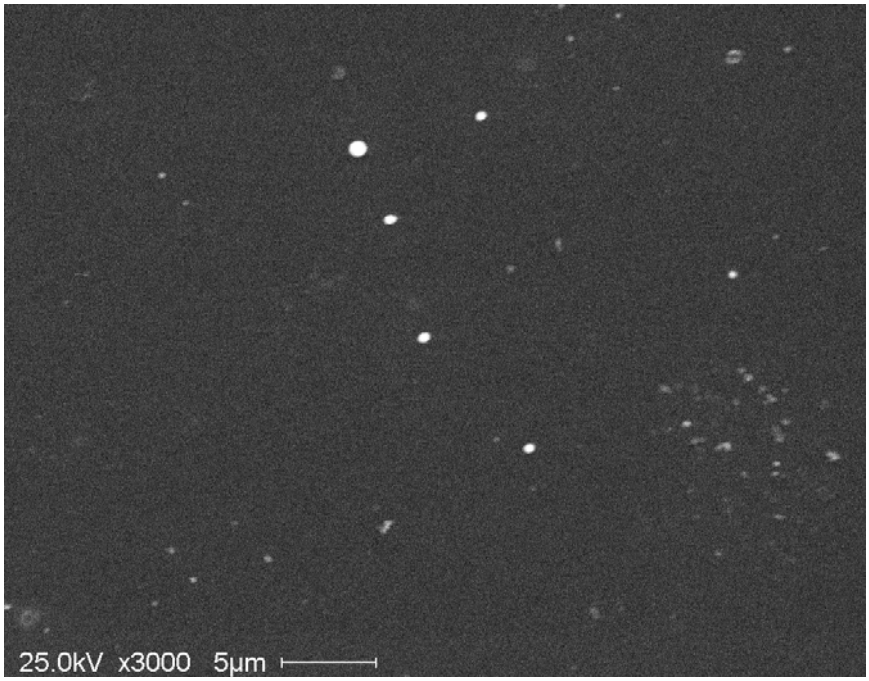

Figure 3.13. SEM micrograph of a carbon film deposited with the hollow-anode configuration at 148.4 J discharge energy.

3.3. Effect of Magnetic Field on the Film Growth

Magnetic guiding of the generated plasma was investigated to minimize deposition on the inside of the hollow electrode wall. A solenoid arrangement was used to generate axial and radial components of a magnetic field on the inside of the hollow electrode. The solenoid arrangement is shown in Figure 3.14 and 3.15, and the discharge region of the electrodes is centered inside the coil. Initial investigations found that the solenoid in close proximity to the discharge head retained heat due to the discharge in the region and lead to damage of the discharge head and solenoid. A solenoid was developed which was encased in glass and Teflon and was then resistant to heat damage. The solenoid had dimensions of inside diameter of 4.1 cm, length of 2.4 cm, and 266 turns.

Laser 3, the single spatial mode with single longitudinal mode CO_2 laser as described in Section 2.4.2 and Section 2.3.3, was operated at 143.1 ± 18.2 mJ at 1 Hz. The PFN was 31.2 mF, V_i was 100V. The average PFN discharge voltage was 31.9 ± 1.9 V, the average current pulse FWHM was 2.1 ± 0.1 ms, the average peak current was 1197.1 ± 45.6 A, and the average PFN discharge energy was 140.12 ± 2.4 J. The four PFN discharge parameters were each linear and not significantly different throughout the range of magnetic field strengths investigated.

The effect of the magnetic field on the film growth was investigated. Magnetic field strengths in the range of 0 – 18.4 mTesla were used. The hollow-anode discharge head was utilized for this investigation to facilitate the focusing of the CO_2 triggering laser beam onto the exposed cathode rod. The hollow electrode is obstructed for laser triggering by the solenoid when using the hollow cathode discharge head.

The on-axis film thickness was measured at a range of magnetic field strengths, shown in Figure 3.16. The average film thickness was measured to be 0.53 ± 0.9 Å/shot,

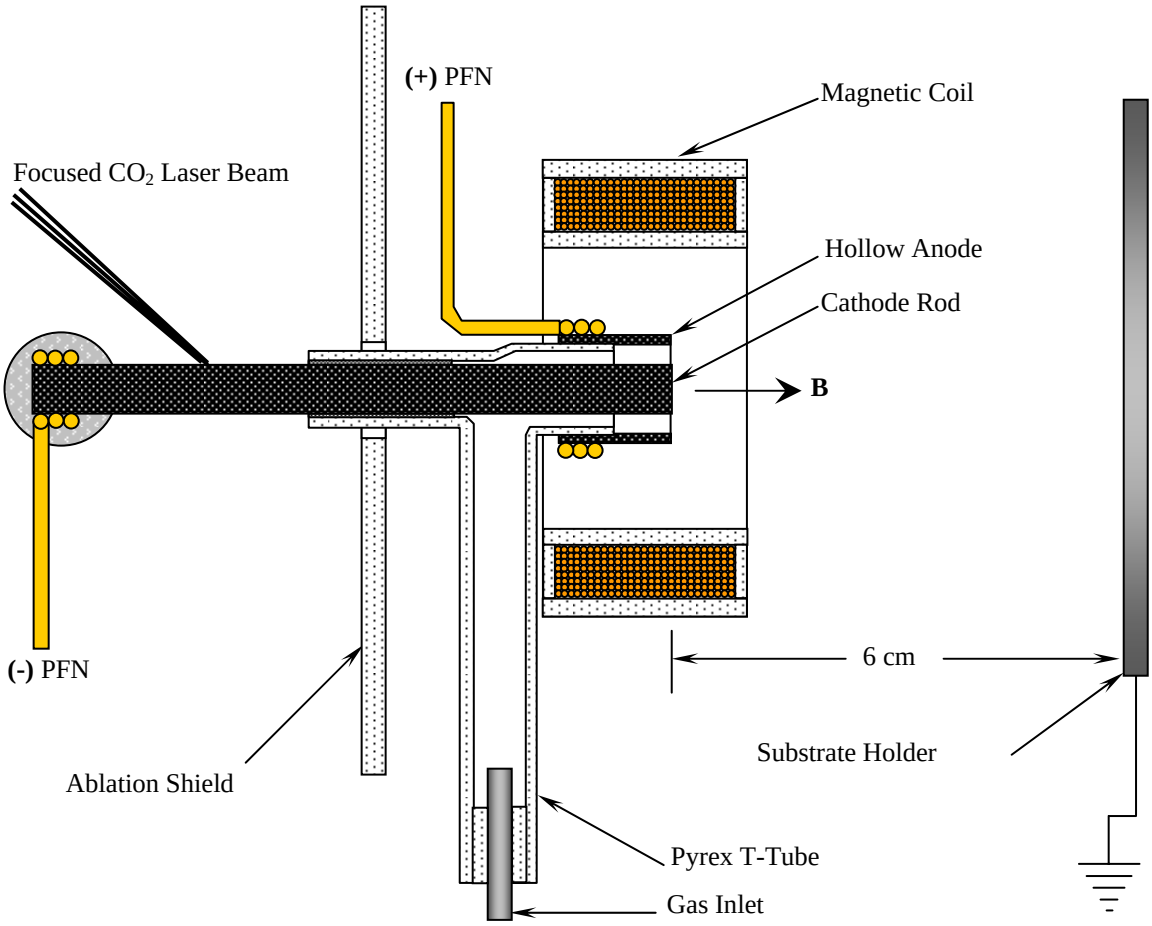

Figure 3.14. Cross-sectional view of the hollow anode discharge head with magnetic solenoid.

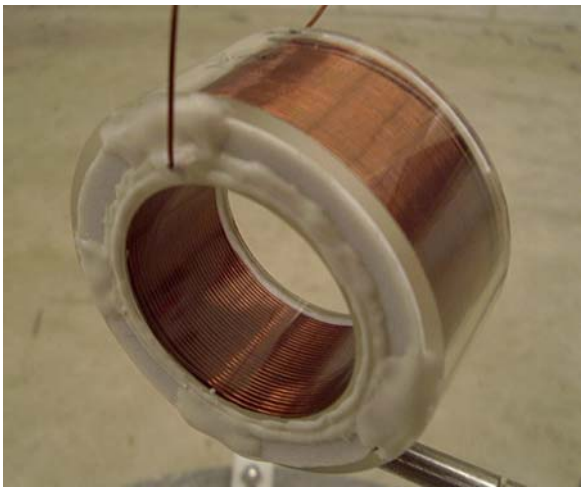

Figure 3.15. Picture of magnetic solenoid.

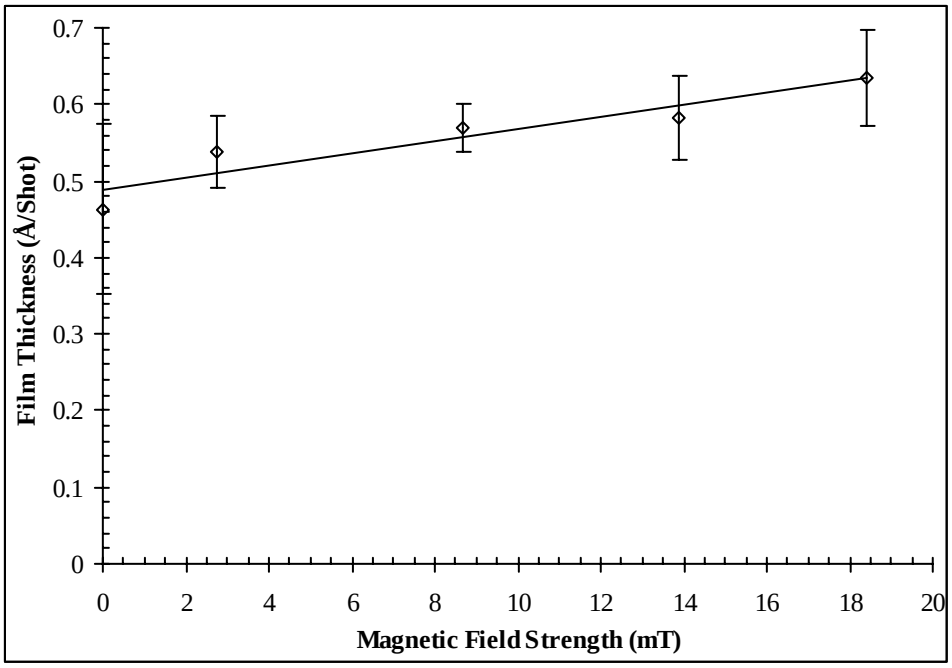

Figure 3.16. On-axis film thickness per pulse obtained for different magnetic field strengths.

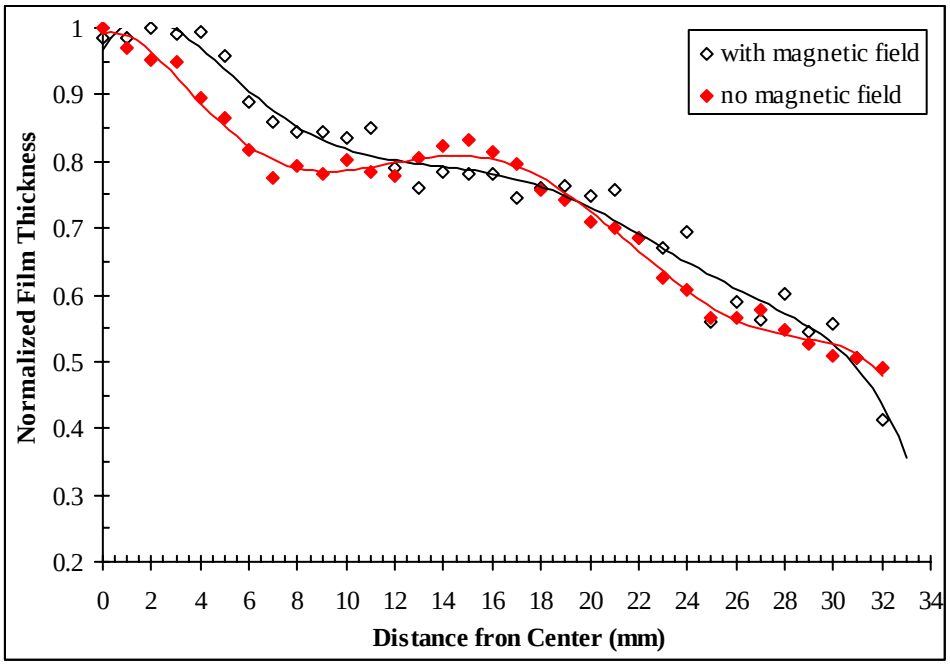

Figure 3.17. Normalized radial film thickness with a 18.4 mT magnetic field and without a magnetic field applied.

and there was a slight increase in film thickness as the magnetic field strength increased but was not significantly different. A magnetic field strength in the range investigated did not have a significant effect on the on-axis film thickness.

The film thickness radial profile was investigated. Films were deposited with an 18.4 millitesla magnetic field applied and without. The film thickness was normalized and compared in Figure 3.17. There was a slight dampening of the ‘humps’ found in the film profile, but not a significant change toward a more forward directed film as anticipated.

3.4. Optical Diagnostics - ICCD

An intensified charged-coupled device (ICCD) was used for imaging of the transient plume. Two-dimensional imaging of plumes is a very important diagnostic technique. Because ICCD systems are electronically gated, they can be very accurately timed relative to the discharge plume, on the order of nanoseconds. This provides a very short shutter speed as well as very accurate post laser trigger timing method. These images are extremely useful in analyzing plume propagation and dynamics, especially plume propagation into background gases [44]. Notch filters can be placed in front of the ICCD to allow two-dimensional imaging of a single wavelength.

3.4.1. Experimental Setup

The ICCD imaging system for this experiment was a Princeton Instruments (Roper Scientific) ICCD Camera (384x576 pixels), PG-200 Pulse Generator, and ST-138 Detector Controller. WinView32 software was used to run the system. The gate width for the ICCD was set to 10 ms, each image was 25 accumulations to reduce pulse to pulse

variation. For each image, a new background was saved, and each image includes background subtraction. The imaging lens was an 18.5 cm focal length plano-convex lens with an 11.9 cm diameter. Attenuation using neutral density filters was placed in front of the detector as needed. A 426 nm notch filter was placed in front of the ICCD array in order to image only the plume from C^+ which has a corresponding 426 nm emission.

ICCD imaging of plumes involves imaging a plume with a lens onto the ICCD array of the camera. The entire plume image must fit onto the ICCD array. Since a plume can be many centimeters long, and an ICCD array is roughly 0.8 cm tall by 1.25 cm wide, imaging usually involves demagnification. Object distance, image distance, and focal length must be chosen to accommodate this requirement. Since the plume is a three-dimensional object without sharp boundaries, optical alignment of the system is achieved by focusing a two-dimensional object with sharp boundaries; a backlit cutout pattern in an opaque card was used. Figure 3.18 shows the ICCD image of the focusing card, the evenly spaced cutout slits are 1 mm wide, 1 cm high, and are 1 cm apart in order to visualize how much of the plume will be imaged onto the ICCD array. The focusing card was positioned between the front of the magnetic coil and the face of the substrate holder. The two-dimensional object is placed along the plane where the center of the plume is

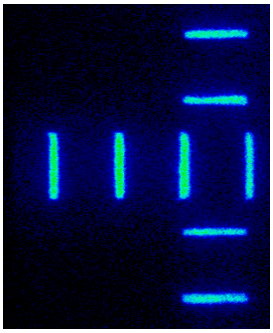

Figure 3.18. ICCD image of the backlit scale marker focusing card.

expected. Once focused onto this plane, the ICCD system will then be focused onto the The two-dimensional object is placed along the plane where the center of the plume is center plane of the plume.

The PFN was operated at 100 VDC initial voltage, 31.3 mF capacitance. The ambient gas was argon and the pressure was maintained at 15 mTorr. The hollow-anode configuration was used so the system could be triggered by striking the rod-cathode. Trials were conducted with and without the magnetic field to investigate the effect of the magnetic field on the plume.

3.4.2. Results

The system was operated without the magnetic field but with the magnetic coil in place, the time delay was stepped from 0 to 24 ms with respect to the triggering by the CO_2 laser. Figure 3.19 and 3.20 shows ICCD images of the plume at different time delays without the magnetic field applied. The different colors are representations of different intensity ranges. From lowest to highest intensity the colors are black, blue, green, yellow, red and white. All the ICCD images shown in Figures 3.19 through 3.21 have been normalized to the highest intensity obtained in order that the images can be compared to one another. Figure 3.21 shows ICCD images of the plume, while the system was operated in the presence of a magnetic field of 18.4 mTesla. The intensity at various on-axis positions at different time delays is shown in Figure 3.23 and 3.24 for operation without and with the magnetic field, respectively. The on-axis positions were 2.5 cm, 3 cm, 4 cm, and 5 cm from the front of the discharge head. An average current pulse of the two trials is shown in Figure 3.22. It was observed that the shape of the current pulse and the ICCD intensities in Figures 3.23 and 3.24 are similar. The on-axis

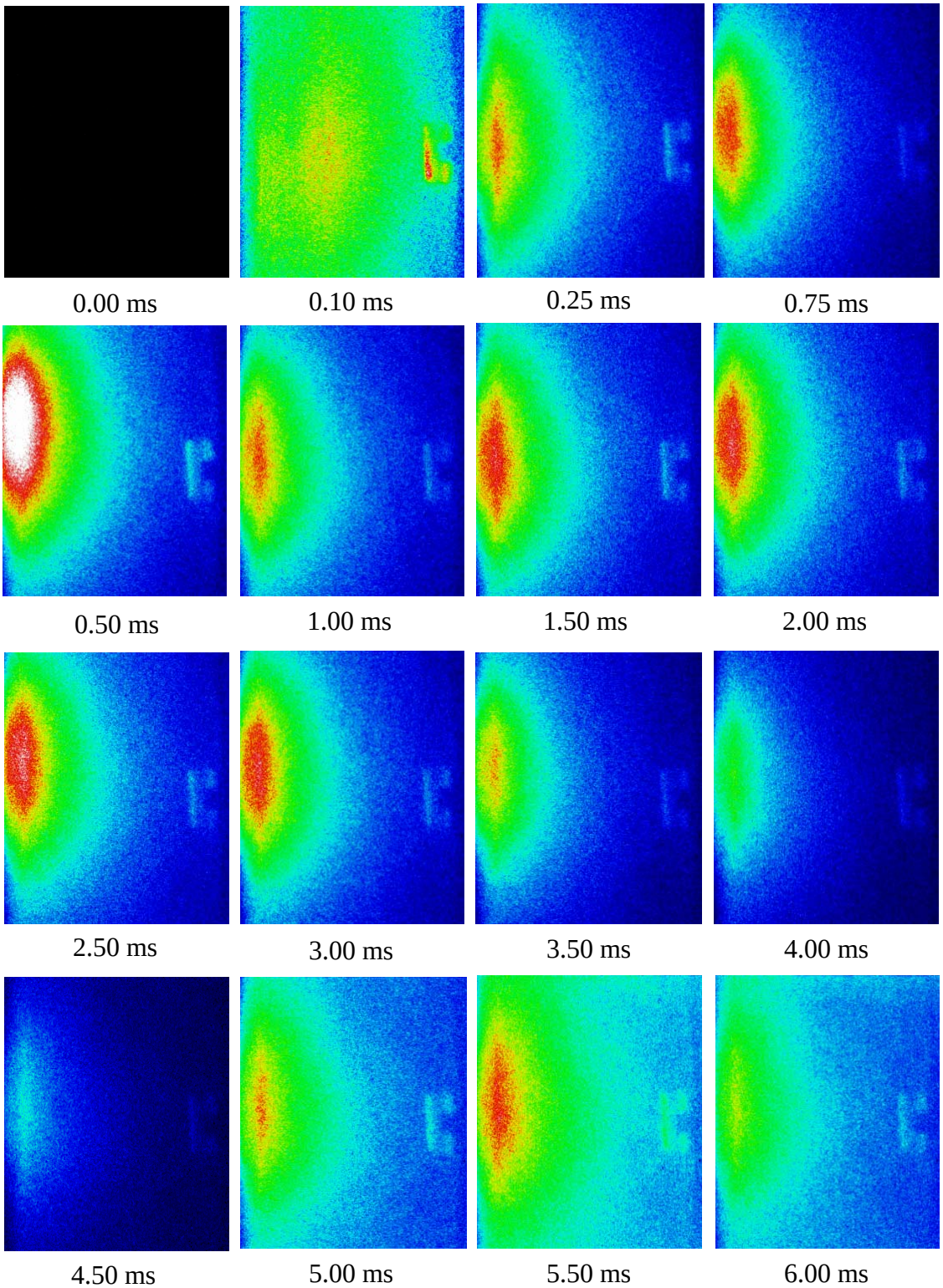

Figure 3.19. ICCD images of the plume without an applied magnetic field at various delays from 0 to 6.00 ms.

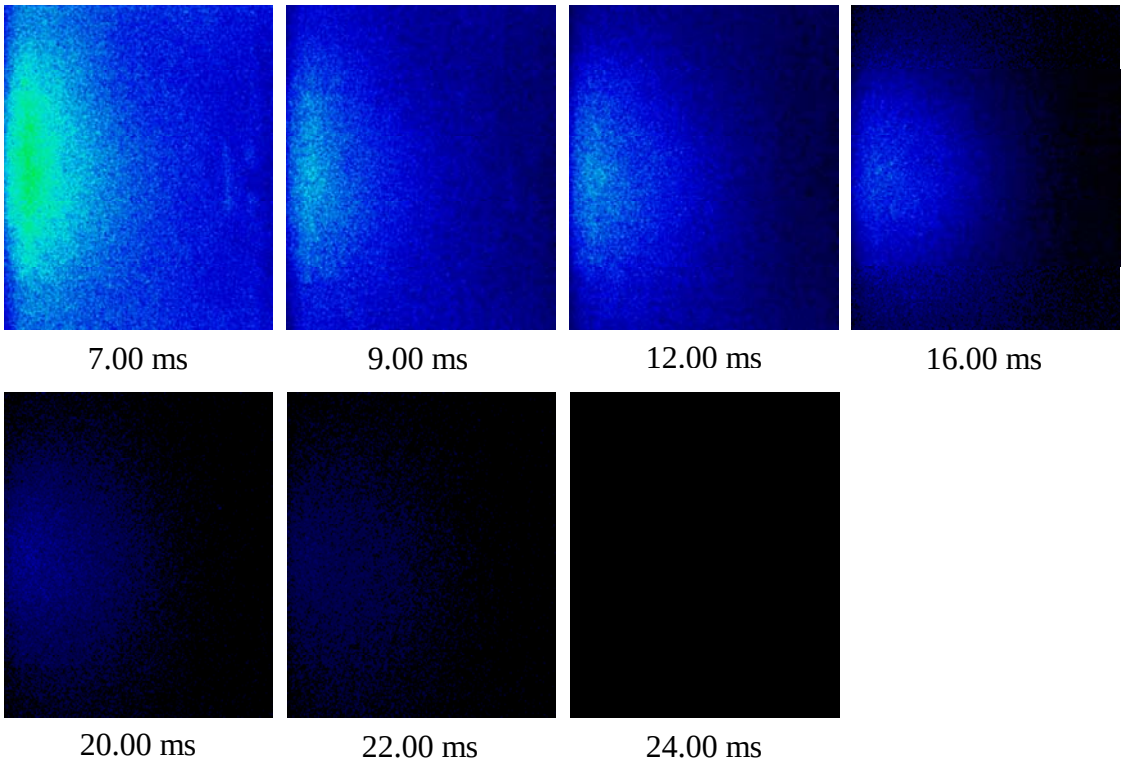

Figure 3.20. ICCD images of the plume without an applied magnetic field at various delays from 7.00 to 24.00 ms.

intensity with the magnetic field applied is suppressed as compared to the intensity without the magnetic field. The current pulse peaked at 0.16 ms, however, the intensity peak occurred at 0.75 ms for both cases. The emission was observable for 22 to 24 ms even though the current pulse ended at 4 ms. The average intensity of the discharge at various positions is shown in Figure 3.25.

The plume emission intensity slightly increases again after approximately 4 ms, as seen in Figures 3.19, and Figure 3.21, for both conditions with and without the applied magnetic field, respectively. The averaged current pulse, seen in Figure 3.22, becomes negative at approximately 3.75 ms reversing the direction of the electron flow between the electrodes. An example of the negative portion of the current pulse can be seen in the under damped and critically damped portions of the voltage signal for a single PFN

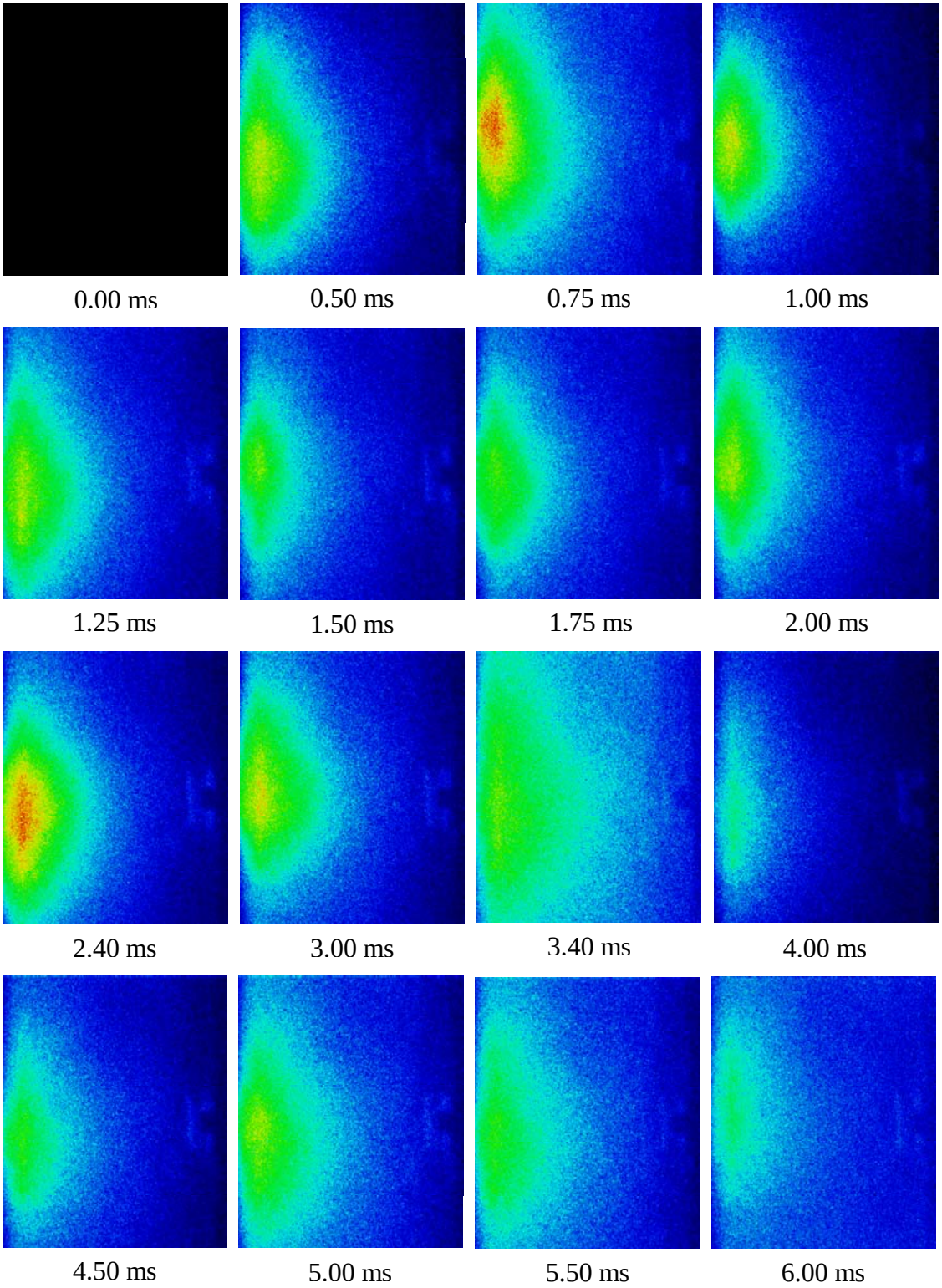

Figure 3.21. ICCD images of the plume with an applied magnetic field at various delays from 0 to 6.00 ms.

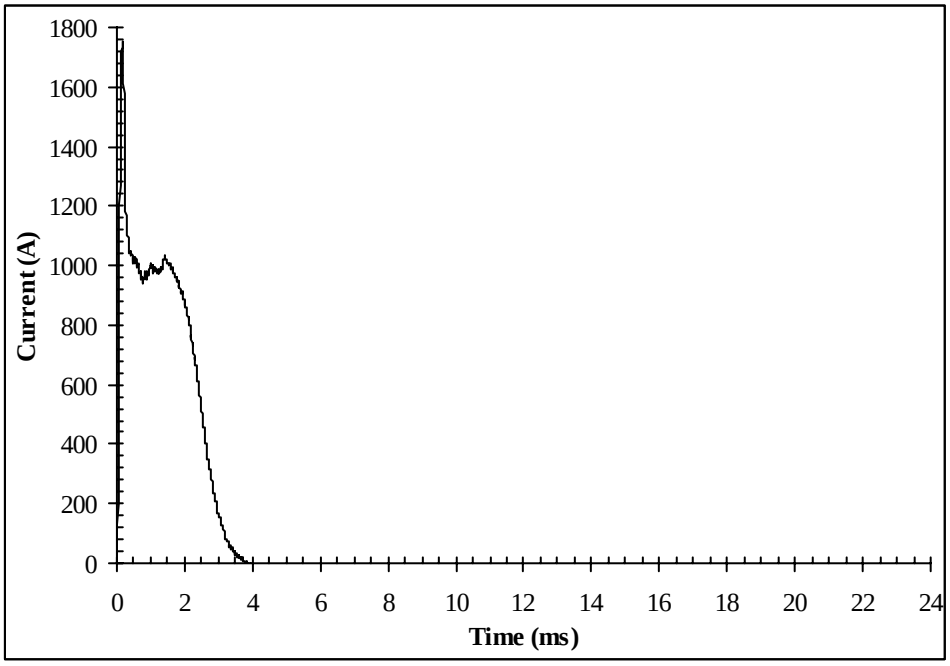

Figure 3.22. Current pulse used during imaging of the plume with and without an applied magnetic field.

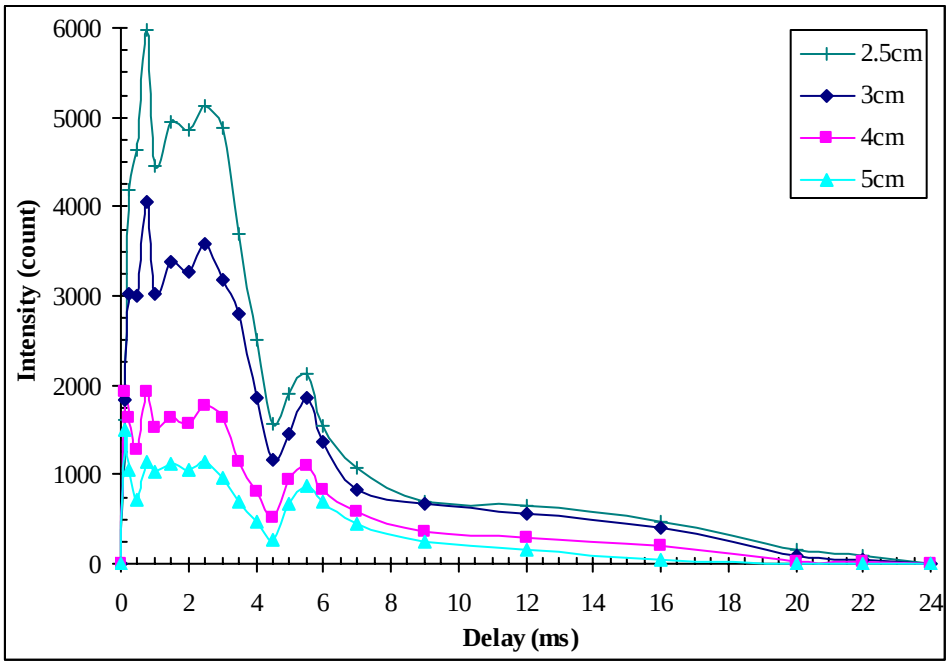

Figure 3.23. On-axis intensity of the plume as a function of the delay at 2.5, 3, 4 and 5cm from the rod tip without an applied magnetic field.

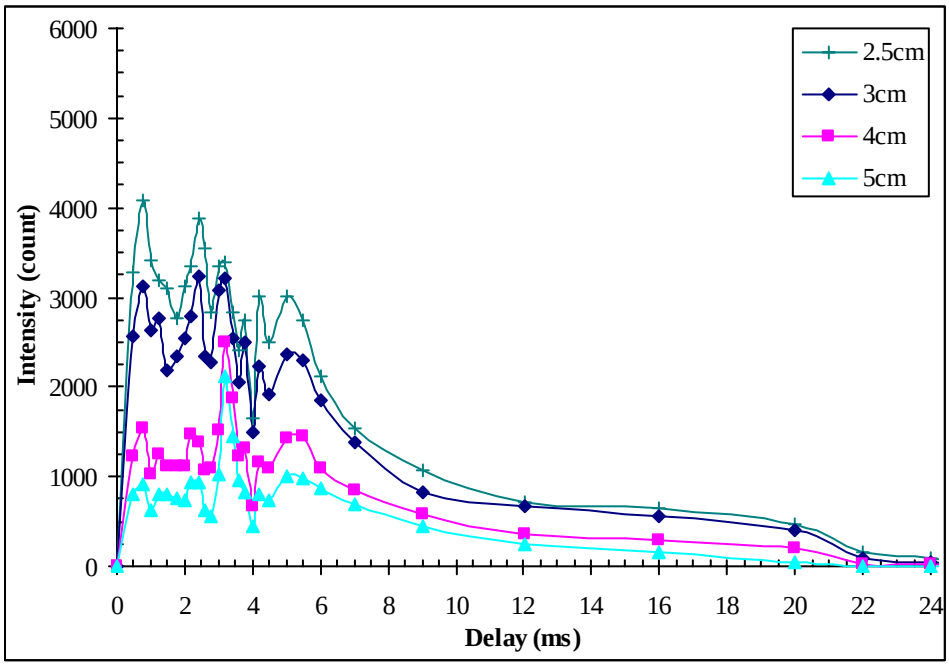

Figure 3.24. On-axis intensity of the plume as a function of the delay at 2.5, 3, 4 and 5cm from the rod tip with an applied magnetic field.

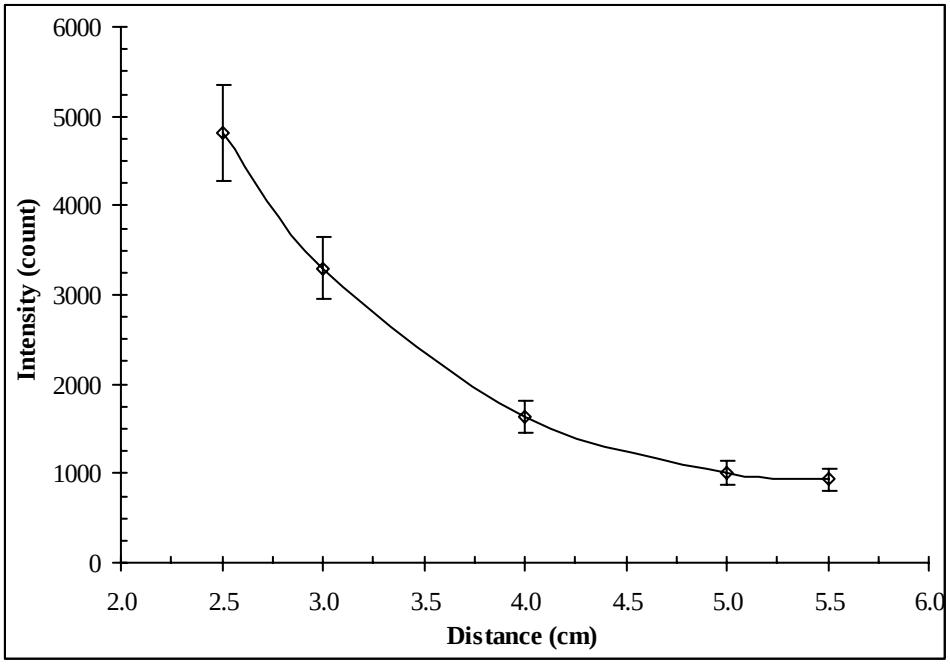

Figure 3.25. Average on-axis intensity as a function of distance.

discharge as shown in Figure 2.29, and in an average voltage signal shown in Figure 2.30. The increase in intensity and slow decrease is can be seen by the on-axis intensity of the plume, as shown in Figures 3.23 and 3.24. This measured intensity is the contribution of the electron broadband emission, “white light”, which also passes through the 426 nm filter.

CHAPTER 4. HIGH VOLTAGE TRIGGERED HOLLOW-ELECTRODE TRANSIENT PLASMA DISCHARGE SYSTEM FOR THIN FILM GROWTH

This chapter serves as a description of the experimental apparatus and the mechanism of the high voltage triggered hollow electrode transient plasma process. The motivation for the project is discussed in detail through an investigation of characterization of the glow discharge, and deposited thin films. A dual titanium-carbon plasma system was also investigated for the feasibility of a multi-component deposition system.

4.1. System Description

This section of the chapter serves as a detailed description of the components of the experimental apparatus. The high-voltage hollow electrode transient plasma discharge system consists of a discharge head, a pulse forming network, a glow discharge system and a vacuum chamber. The triggering CO_2 laser used previously has been eliminated to simplify the system and the triggering system was achieved by the use of a glow discharge system.

4.1.1. Hollow-Electrode Discharge Head

A positively biased, high voltage (0-1000 VDC), low current (200 mA), hollow electrode 3 centimeters in diameter is placed coaxial to the hollow-electrode in order to

ionize the background gas in the region of the discharge electrodes. See Figure 4.1 for the cross-sectional detail of a high voltage hollow-electrode discharge head. The ionized gas between the positive glow ring electrode and the grounded electrode of the discharge head gives rise to a high electron density in the vicinity of the hollow-electrode to aid in the discharge of the PFN.

A cross-sectional detailed diagram of the high voltage hollow-electrode discharge head is shown in Figure 4.1. The construction is very similar to the hollow-electrode discharge head presented in Chapter2. The main exception is that the pre-ionizing ring electrode is eliminated and replaced with a cylindrical glow ring electrode. A ceramic T-tube was constructed to be used as an electrically insulating support for the electrodes and a delivery path for flowing gas between the electrodes of the discharge head at a pre-determined flow rate. The T-tube material was changed from Pyrex to ceramic to withstand the elevated temperatures achieved with this deposition method. The hollow-electrode and rod-electrode of the discharge head are both made of conductive materials. The dimensions of the hollow-electrode are 14.2 mm outside diameter, 11.7 mm inside diameter and 14.8 mm in length. This electrode is firmly pressure fitted to the outside of the ceramic T-tube allowing 7.5 mm of the inside length exposed to the rode electrode. The dimensions of the rod-electrode are 6.25 mm in diameter and approximately 9 cm in length. This electrode is firmly pressure fitted with a Teflon bushing to the inside of the ceramic T-tube to be coaxial to the hollow-electrode allowing 4 mm of the rod length exposed to the inside of the hollow-electrode. The Teflon bushing is located far enough from the high temperature region to still provide support without heat damage. Electrical leads required thermal and electrical insulation to minimize arcing during the discharge.

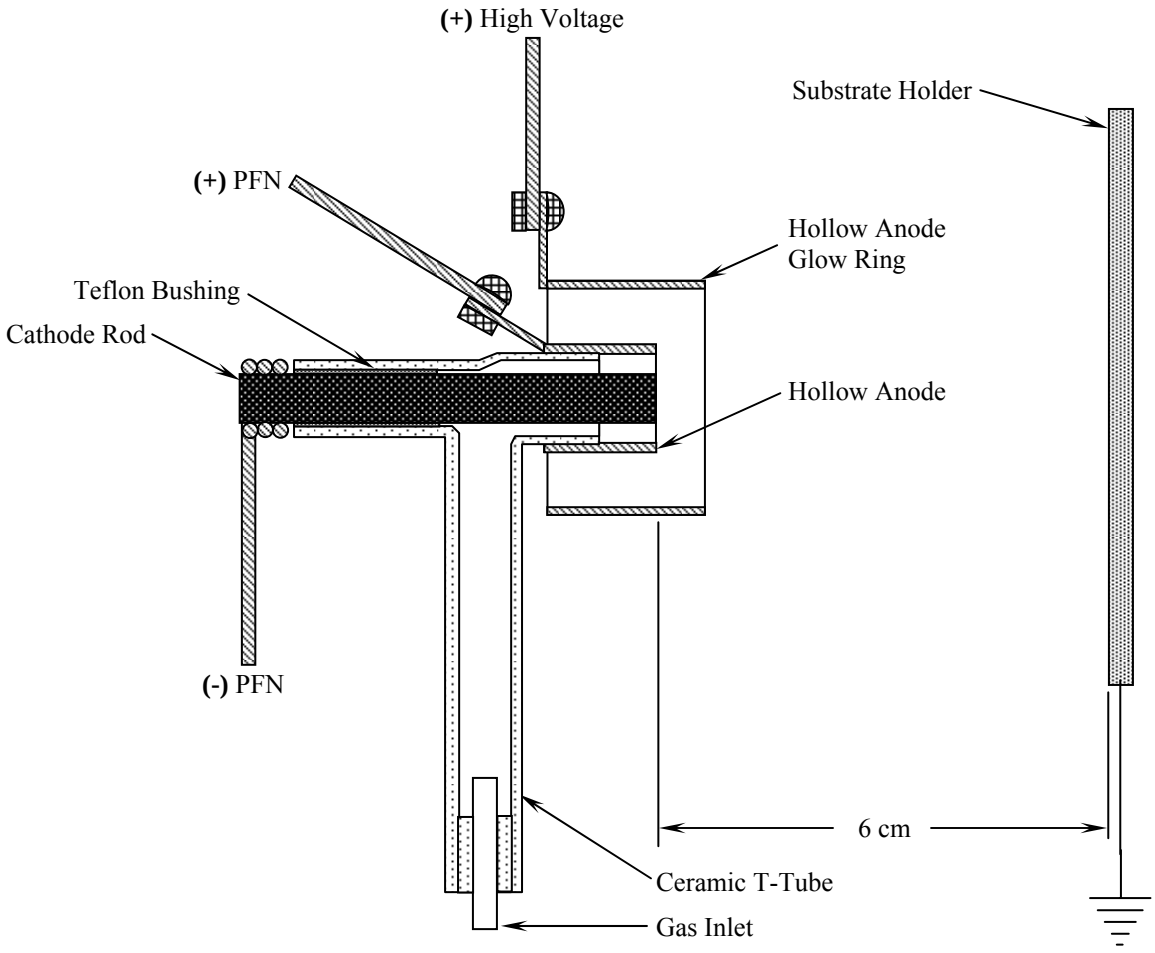

Figure 4.1. Cross-sectional detail of a high voltage hollow-electrode discharge head.

A positively biased, high voltage (0-1000 VDC), low current (200 mA), hollow electrode is placed coaxial and centered to the hollow-electrode in order to ionize the background gas in the region of the discharge electrodes. The dimensions of the cylindrical glow ring electrode are 31.1 mm outside diameter, 28.8 cm inside diameter, and 21.9 cm in length. The glow ring electrode is constructed of copper. This glow ring electrode is provided in order to ionize the background gas causing a luminous glow discharge. The geometry of the discharge head produces a capacitive effect and the

charging and discharge of this capacitive head is used to trigger the PFN discharge. The ionized gas between the positive ring electrode and ground gives rise to a high electron density. In a low-pressure glow discharge a negative space charge region with high electron density is formed near the negative electrode.

4.1.2. Discharge Network

The PFN is the same as the one described in Chapter 2. except that the discharge head electrodes are connected across the negatively grounded instead of the positively grounded PFN. The PFN capacitor bank is charged to the desired voltage by a low voltage, 0-150V, high current, 0-18A, DC power supply. An air cooled variable power resistor is in series with the power supply to limit the current in the circuit and control the charging time of the capacitor bank. The PFN shown in Figure 4.2. is used in the experiments reported here.

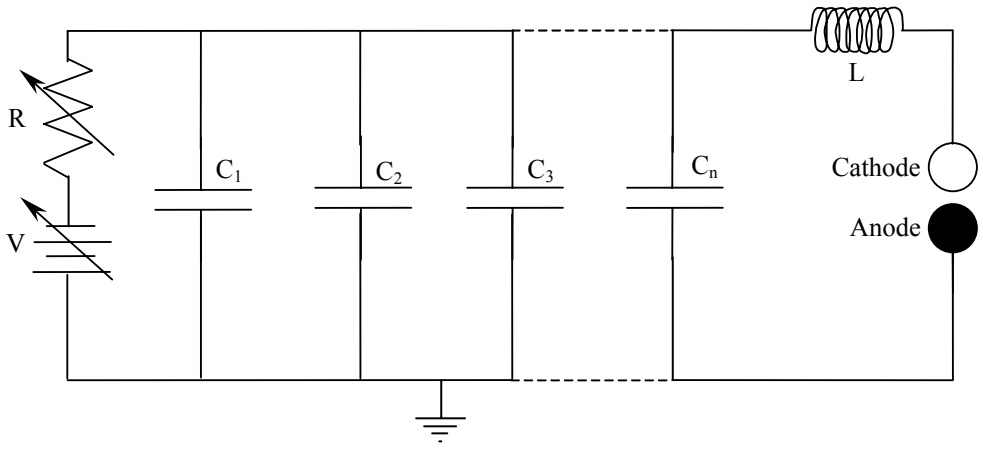

Figure 4.2. The pulse forming network used in the experiments.

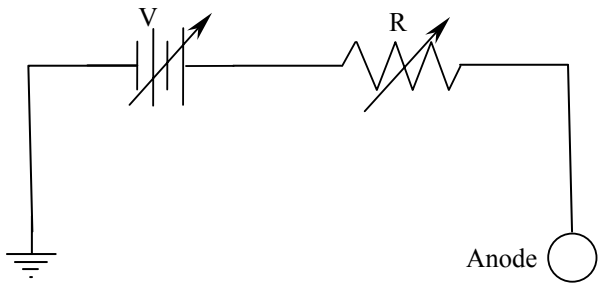

Figure 4.3. The glow discharge circuit used in the experiments.

The glow discharge circuit used in the experiments is shown in Figure 4.3. The variable DC power supply consisted of two Lambda Electronics Model 71, 0 – 500 VDC, 0 - 200 mA, power supplies connected in series, producing up to 1000 VDC at 200 mA. The variable resistor was a 10 kΩ, 0.122 A, Ohmite power rheostat to control the current delivered to the glow discharge.

4.2. Characterization of the Glow Discharge

In the high voltage hollow electrode plasma discharge system, a high voltage, 1000 VDC, positively charged cylindrical ring electrode is used to trigger the PFN discharge. In this section the dependence of the discharge system on circuit grounding as well as the repetition rate that is achievable by this layout is presented.

4.2.1. Experimental Setup

The current pulses generated during the plasma arc discharge, at an initial voltage, V_i, of 100 VDC, and a capacitance, C, of 39 mF were obtained using an inductive coil pickup. The inductor used was a commercial pickup coil with a 5 centimeter diameter

opening. The pickup coil was placed symmetrically around the wire connecting the positive side of the PFN to the anode of the discharge head. The pickup coil was then connected to a 1 GHz oscilloscope. The EMF generated due to the transient discharge was recorded on the oscilloscope in the form of a voltage signal as a function of time. A voltage signal for a single PFN discharge recorded at 15 mTorr of argon is shown in Figure 2.1. An averaged voltage signal for 16 PFN discharges was recorded for current pulse calculations, shown in Figure 2.2. The experimental setup for characterization of the PFN follows that described in section 2.4.1.

4.2.2. PFN Dependence on Network Grounding

This section describes dependence of grounding of the network on the PFN discharging. Observations of achieving a glow discharge and/or PFN discharge while varying the network grounding were performed. The network configuration in Figure 4.4., shows a positive PFN ground like that used for the Chapter 2. investigations, and a negative glow ring ground, with a common ground. The glow ring ionized the gas in the region inside the hollow-electrodes. However, the PFN did not discharge even up to pressures of 1300 mTorr. The laser triggered hollow-electrode system was operated with a positive PFN ground. The network configuration in Figure 4.5., shows a negative PFN ground and a negative glow ring ground, with a common ground. The glow ring ionized the gas in the region inside the hollow-electrodes, and the PFN discharged at 15 mTorr.

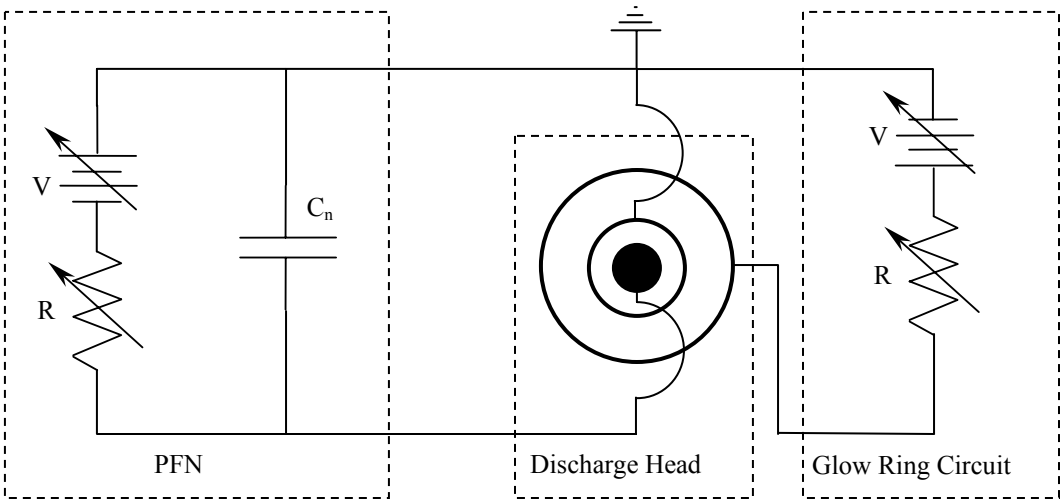

Figure 4.4. Schematic diagram of a positive grounded PFN.

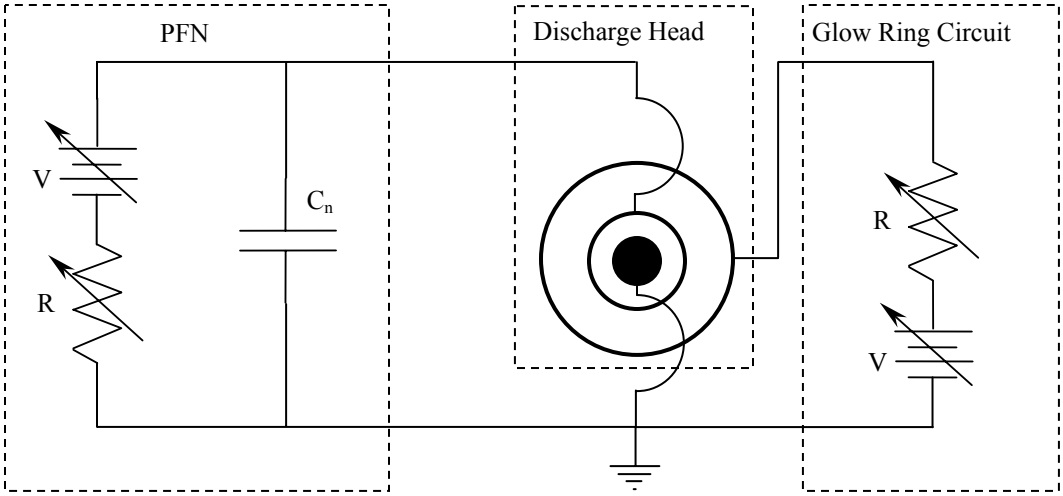

Figure 4.5. Schematic diagram of a negative grounded PFN.

4.2.3. PFN Dependence on Repetition Rate

This section describes the investigations of the repetition rates achievable by this system. First, the repetition rate produced by the glow discharge is examined without the PFN energized. The repetition rate is detected by a charge detection probe placed within

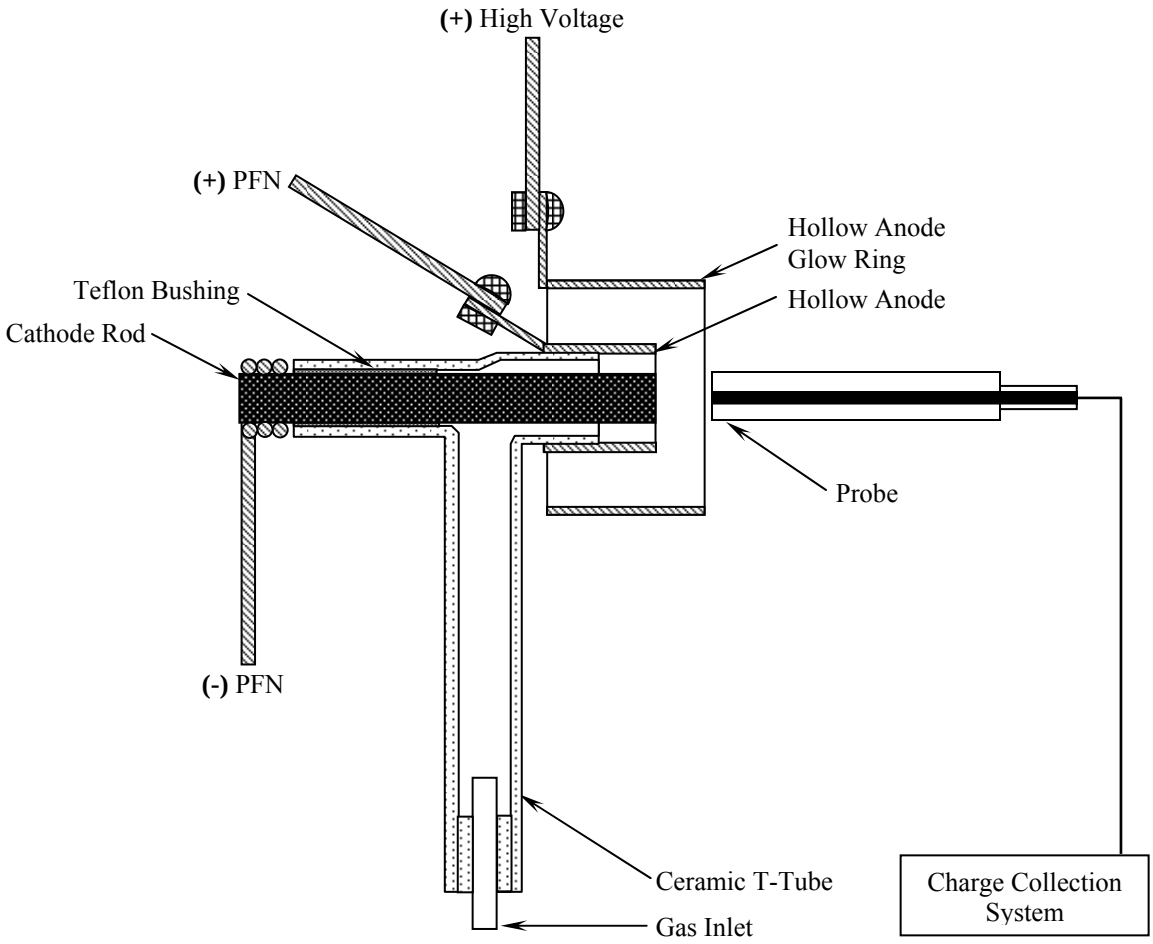

Figure 4.6. Schematic diagram of high voltage triggered discharge head and the charge collection system.

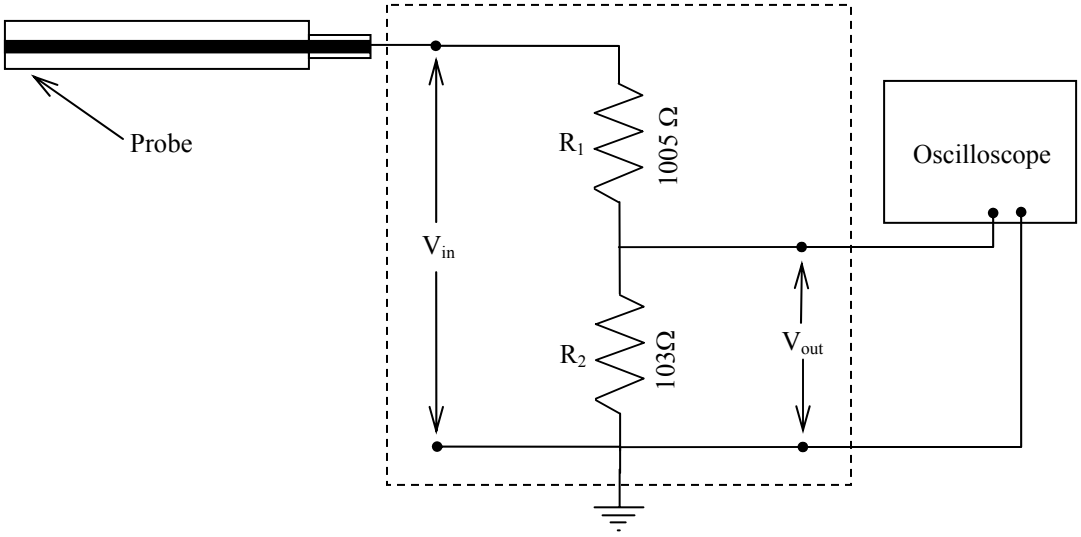

Figure 4.7. Schematic diagram of the charge collection system.

the vicinity of the glow discharge, as shown in Figure 4.6. The charge collection probe is connected to a voltage divider circuit to protect the oscilloscope, as shown in Figure 4.7. The circuit is set up such that

$$V_{out} = \frac{R_1}{R_1 + R_2} V_{in}$$
$$V_{out} = \frac{103\Omega}{1005\Omega + 103\Omega} V_{in} \qquad [4.1]$$
$$V_{out} = (0.093) V_{in}$$

Therefore, the voltage out to the oscilloscope is 9.3% of the voltage into the probe. The internal resistance of the oscilloscope between the signal and ground is 1 MΩ, so most of the current will flow through the voltage divider as required instead of the oscilloscope. The voltage to the glow ring is set at 1000 VDC and the current is varied from 12 to 100mA. The signal is detected by the oscilloscope which records the frequency of the glow discharge. A sample of the signal detected is shown in Figure 4.8. The frequency of the glow discharge at different applied currents is shown in Figure 4.9. This is the repetition rate achieved by the glow ring without the PFN discharging. The frequency of the glow discharge ranges from 0.5 to 13 Hz under these conditions and is easily maintained.

The PFN is then energized and the frequency of the discharge network is determined. The current in the glow ring is adjusted as needed by varying the glow ring circuit resistance to maintain a constant repetition rate. The PFN total discharge energy is varied by changing the capacitance of the PFN using 4.8 mF, 6.0 mF, 7.2 mF, and 8.4 mF. The initial PFN voltage was set at 90 VDC. The PFN discharge energy range produced was 17 J to 30 J. The frequency achieved by the system was 1 Hz to 10 Hz. However, as the discharge head became heated from the plasma, the frequency was

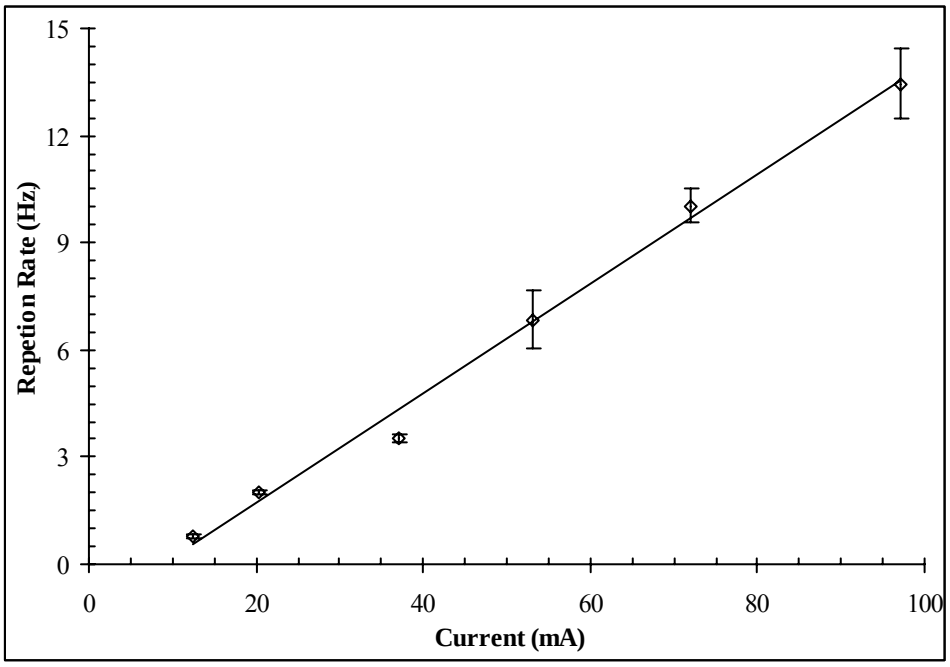

Figure 4.8. A sample of the signal recorded by the charge collection system.

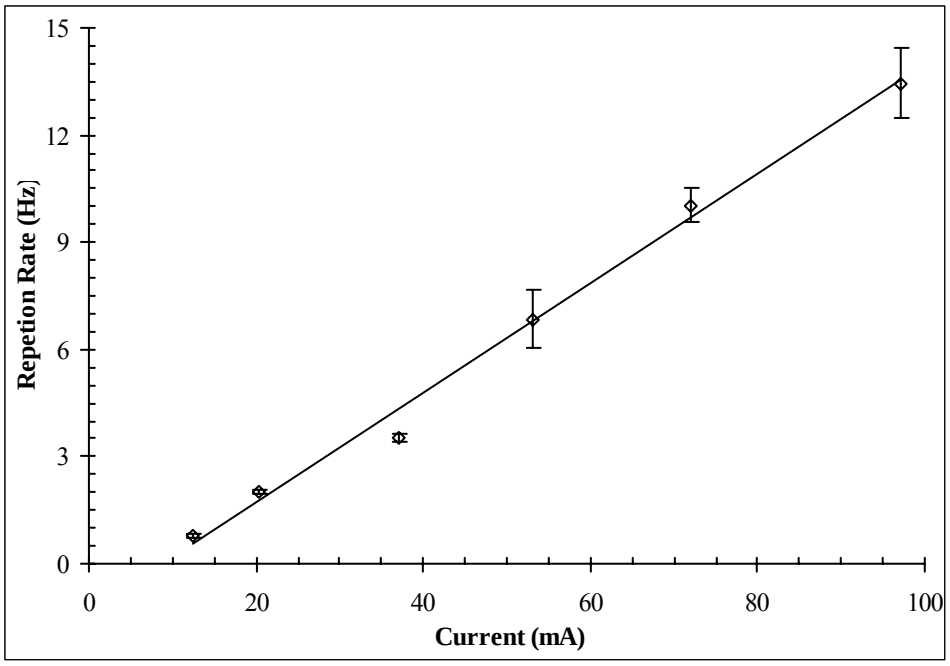

Figure 4.9. Repetition rate of the high voltage triggered system as a function of the current applied to the glow ring.

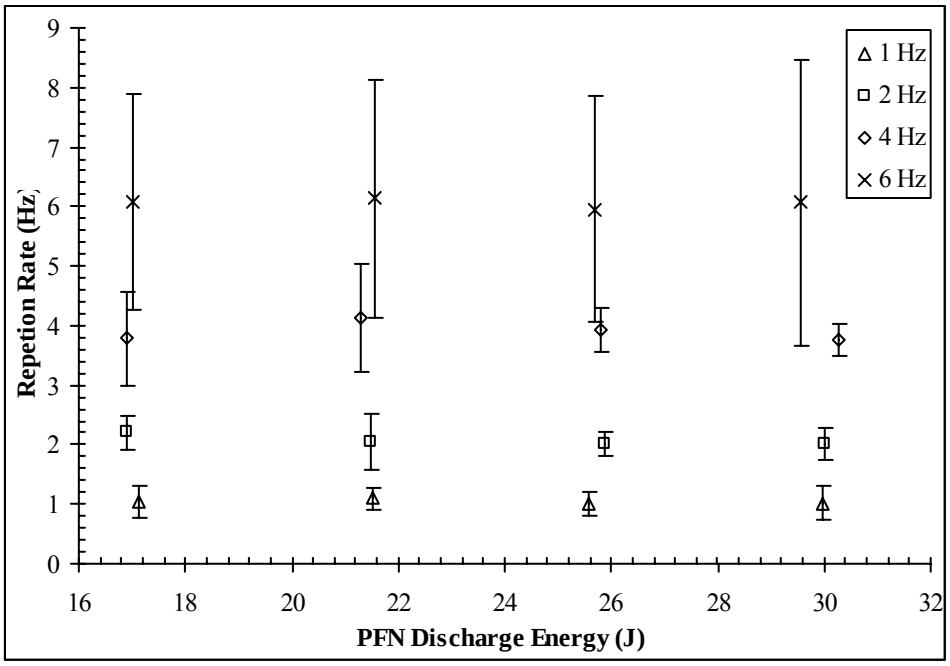

Figure 4.10. Repetition rate of the high voltage discharge system as a function of the PFN discharge energy.

difficult to maintain at high rates. Repetition rates of 1 Hz, 2 Hz, and 4 Hz are strongly, significantly different from each other, but rates higher than 4 Hz are not significantly different from 4 Hz, see Figure 4.10., so the maximum rate expected was set at 4 Hz. In order to maintain these rates the PFN resistance was required to be adjusted to allow the power supply to charge the PFN capacitor bank.

4.3. Characterization of the Thin Films Deposited

In this section the details of the deposition and characterization of carbon and titanium thin films deposited by the high-voltage triggered hollow-electrode transient plasma discharge are discussed. The goal is to investigate the process's ability to produce large area films with a high rate of deposition; especially for titanium since it was not

possible to achieve titanium deposition using the laser triggered hollow-electrode system. SEM micrographs of the films deposited are also presented as part of the film morphology studies.

4.3.1. Thin Film Preparation

Thin film preparation for these studies followed the same procedures discussed in Section 3.2.1. Argon was used as the background gas with a pressure of 15 mTorr. The PFN initial voltage was varied in the range of 90 VDC to 130 VDC, and the PFN capacitance was varied between 2.4 mF to 8.4 mF to achieved the desired PFN discharge energy. The substrate was protected behind a shutter during the first one minute of discharges. The shutter was then moved away to begin the deposition and was carried out for a set number of pulses at the desired repetition rate.

4.3.2. Film Thickness Measurements

Film thickness measurements were performed following the same procedure presented in Section 3.2.2. On-axis and radial film thickness measurements of the carbon and titanium films deposited by argon plasmas were obtained.

4.3.2.1. Carbon Film Thickness Measurements

An investigation of the dependence of carbon film deposition on the discharge repetition rate was performed. The PFN initial voltage was set at 130 VDC, and the PFN capacitance was set at 4.7 mF, to produce a PFN total discharge energy of 38.4 ± 1.6 J. The repetition rate was varied between 0.25 Hz to 4 Hz. The film deposition rate was

constant at an average of 2.9 ± 0.1 Å/pulse, as shown in Figure 4.11. Therefore, the carbon deposition rate is not dependent on the discharge repetition rate under these conditions.

The deposition rate of carbon films was then investigated as a function of the PFN discharge energy. The PFN initial voltage was varied between 120 VDC to 130 VDC, and the PFN capacitance was varied between 2.34 mF to 4.7 mF, to produce PFN total discharge energies between 16 J to 38 J. The repetition rate was set at 0.8 ± 0.1 Hz. The plasma was observed to form micro-discharges and a non-uniform arc as the PFN discharge energy became greater than 38 J. The linear region of the film deposition as a function of the PFN discharge energy is shown in Figure 4.12. The rate of change is given by the slope of the linear region, in terms of the deposition rate per discharge energy, $\Delta d/E_C$, in units of (Å/pulse)/J. The equation of the trend line for the linear region was found to be;

$$y = 0.4182x - 12.823 \qquad [4.2]$$

then,

$$\left(\frac{\Delta d}{E_C}\right)_{HV-anode} = 0.4182 \qquad [4.3]$$

These results were then compared to the carbon film deposition rates for argon plasma with the laser triggered hollow-anode configuration described in Section 3.2.2. and Table 3.1 where the there was no film deposition at PFN discharge energies of 65.7 J and lower and where the deposition rate per discharge energy was:

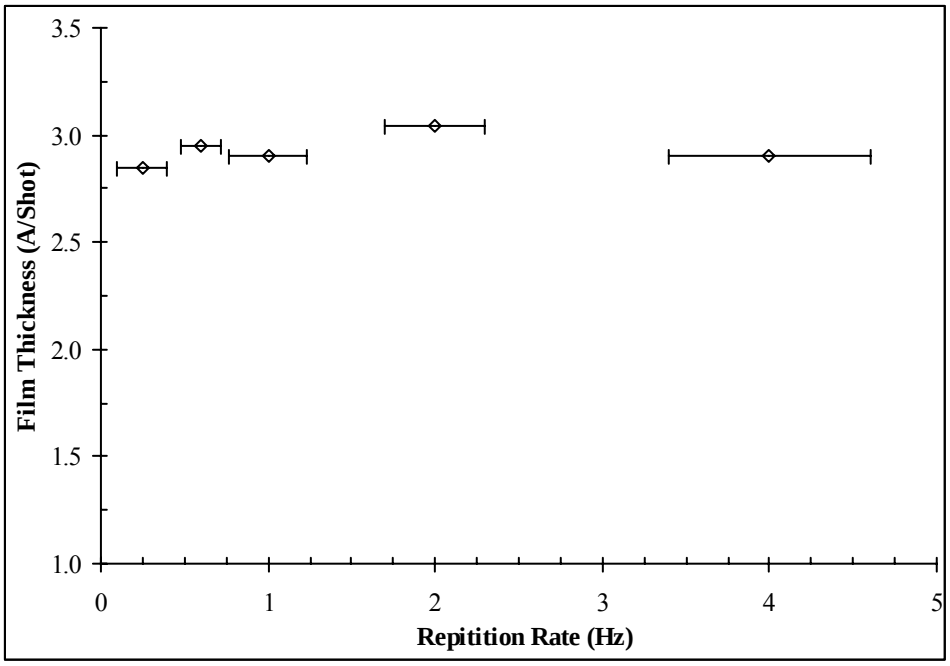

Figure 4.11. On-axis carbon film thickness measurements as a function of the PFN discharge energy. Films were deposited in argon ambient using the hollow-anode configuration.

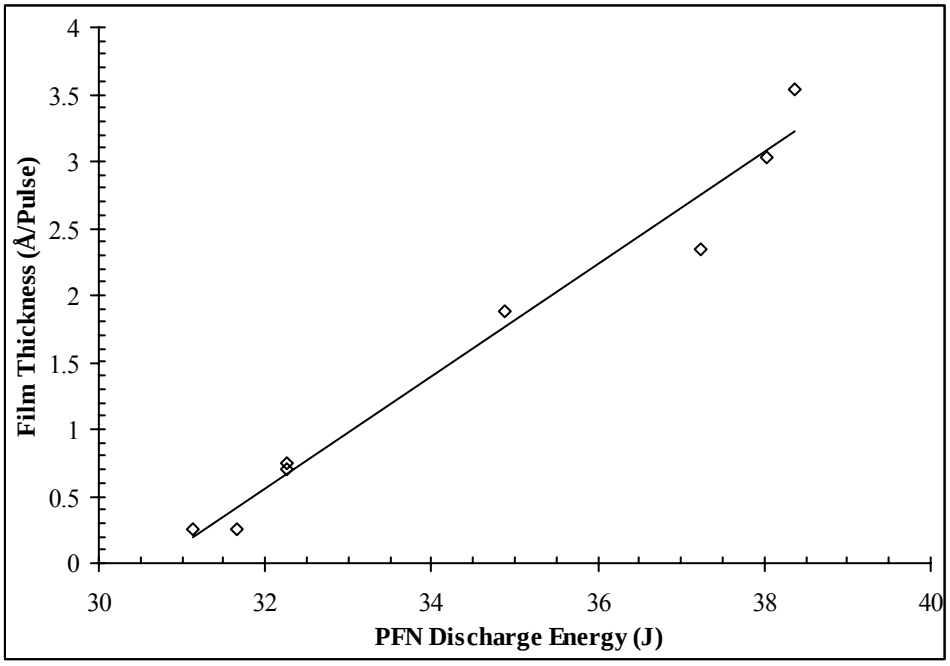

Figure 4.12. The linear region of the carbon film thickness measurements as a function of the PFN discharges energy. Films deposited in argon ambient using the hollow-anode configuration.

$$\left(\frac{\Delta d}{E_C}\right)_{Ar-anode} = 0.0063 \qquad [4.4]$$

The $\Delta d/E_C$ ratio of the high-voltage triggered to laser triggered hollow-anode configurations in argon is:

$$\frac{\left(\frac{\Delta d}{E_C}\right)_{HV-anode}}{\left(\frac{\Delta d}{E_C}\right)_{Ar-anode}} = \frac{0.4182}{0.0063} = 66.4 \qquad [4.4]$$

therefore, the deposition rate per discharge energy for the high-voltage triggering is approximately 66 times greater than that of the laser triggered hollow-anode electrode configuration in an argon plasma. Higher deposition rates at significantly lower PFN discharge energies were achieved using the high voltage triggered hollow-anode system than using the laser triggered system. It may be concluded that for the laser-triggered configuration the majority of the PFN discharge energy was used to ionize the plasma while with the high-voltage triggered configuration the glow discharge is strongly contributing to the ionization of the plasma.

4.3.2.2 Titanium Film Thickness Measurements

Preliminary investigations for deposition of titanium using the high voltage triggered hollow-anode configuration found that the hollow-anode would become hot enough to melt due to the electron bombardment when operated under the same parameters used for carbon deposition. Therefore, the electrode configuration was changed to the hollow-cathode configuration for titanium deposition. The titanium rod-anode would become heated and essentially be an evaporative process. The PFN initial

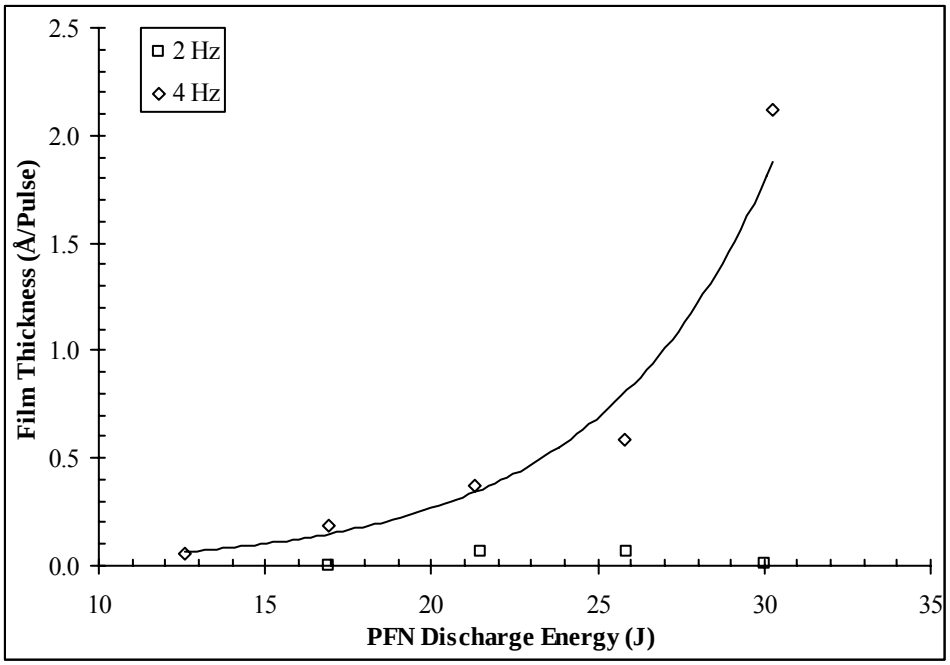

Figure 4.13. Titanium film thicknesses as a function of PFN discharge energy at 2 Hz and 4 Hz.

voltage was set at 90 VDC and the PFN capacitance was varied between 4.8 mF and 8.4 mF, to produce PFN discharge energies in the range of 12 J to 30 J. The repetition rate was varied at 2 Hz and 4 Hz. There was negligible titanium deposition at 2 Hz at discharge energies less than 40 J, and at this energy and higher the hollow-cathode became hot enough for thermionic electron emission and the repetition rate would become unstable. At 4 Hz as the PFN energy increased the deposition rate increased, see Figure 4.13. However, as the discharge energy approached 30 J the tip of the rod became molten enough that it could not support its own weight. It would start to liquefy causing explosive ejections of molten titanium and create a short between the anode and cathode. Figure 4.14 shows pictures of various titanium rods after being exposed to different PFN discharge energies. The effect of the plasma discharge process can be clearly seen as one

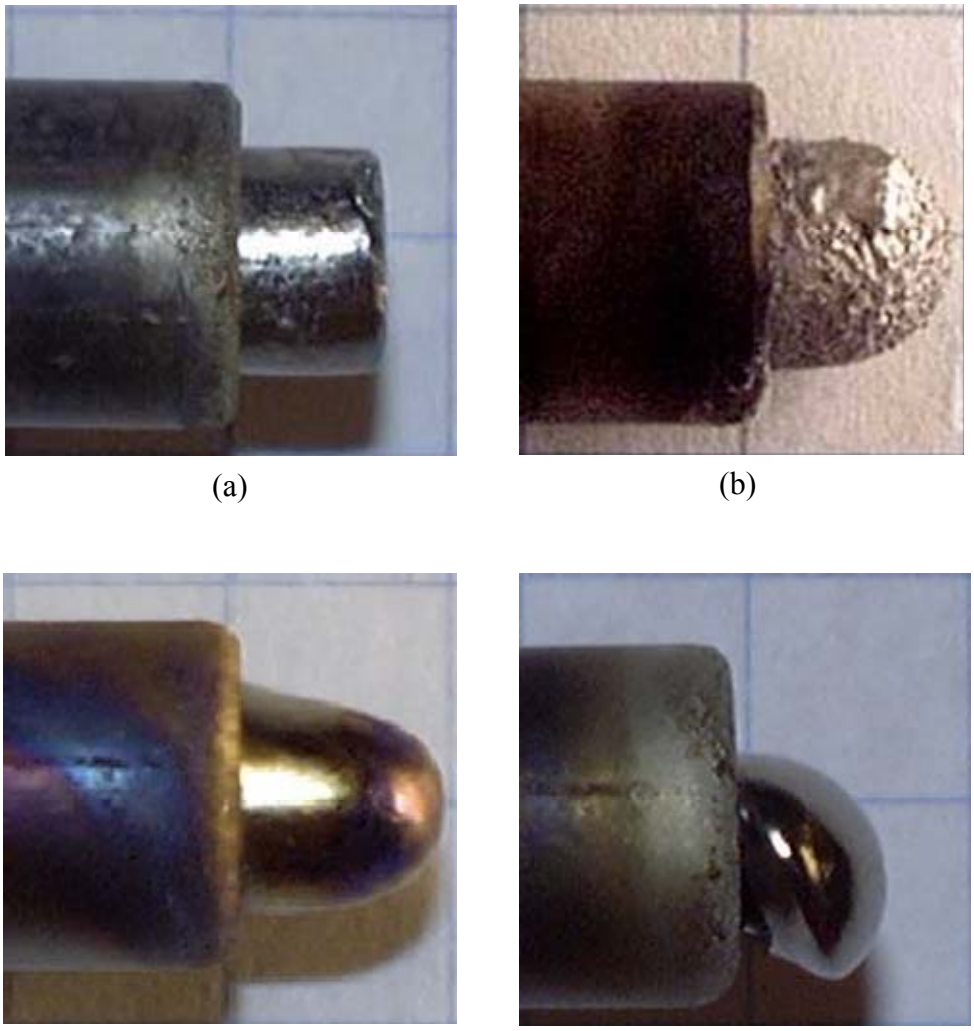

(a) (b)

(c) (d)

Figure 4.14. Titanium rod-anode at various PFN discharge energies of (a) 0 J, (b) 16.9 J, (c) 25.8 J, and (d) 30.3 J.

examines the morphology of the tip from a new tip at 0 J, a sputtered tip at 16.9 J, a melted surface of the tip at 25.8 J, and a completely molten tip at 30.3 J of PFN discharge energy. Trials operated at 2 Hz in the PFN discharge energy range of 9 J to 30 J would affect the titanium tip similar to the sputtered tip but not produce a detectable film.

4.3.3. Scanning Electron Microscopy of the Thin Films

SEM micrographs are presented to investigate the quality of the carbon and titanium films deposited by high-voltage triggered hollow-electrode arc discharge. The SEM micrographs presented in Figures 4.15 through 4.17 and Figures 4.18 through 4.21 show the surface morphology of the carbon and titanium films deposited, respectively at increasing PFN discharge energies. These films contain a higher density of particles throughout the film surface area, than with the laser triggered hollow-electrode configurations presented in Section 3.2.3.

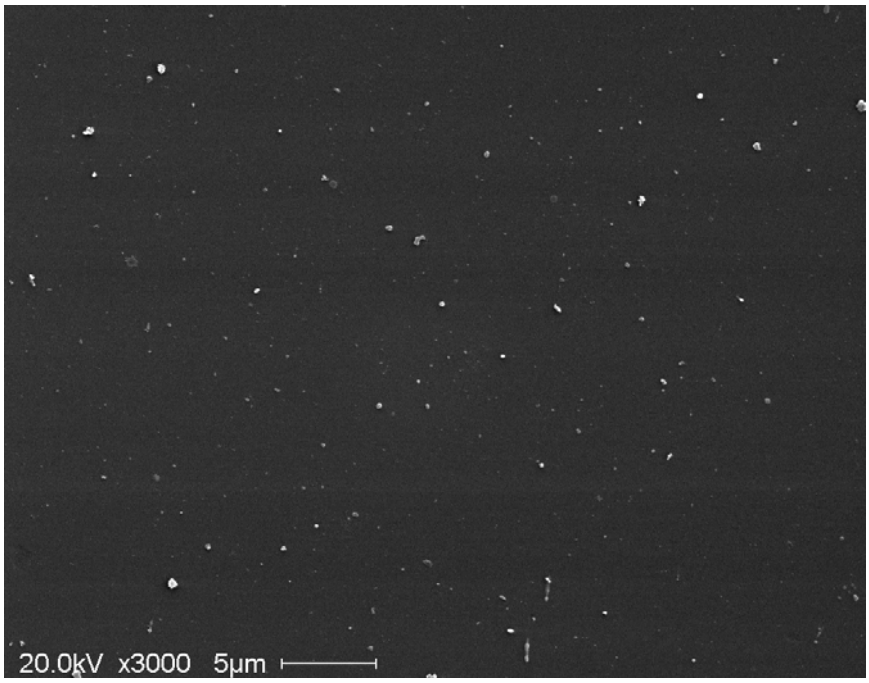

Figure 4.15. SEM micrographs of a carbon film deposited with hollow-anode configuration at a PFN discharge energy of 32.3 J.

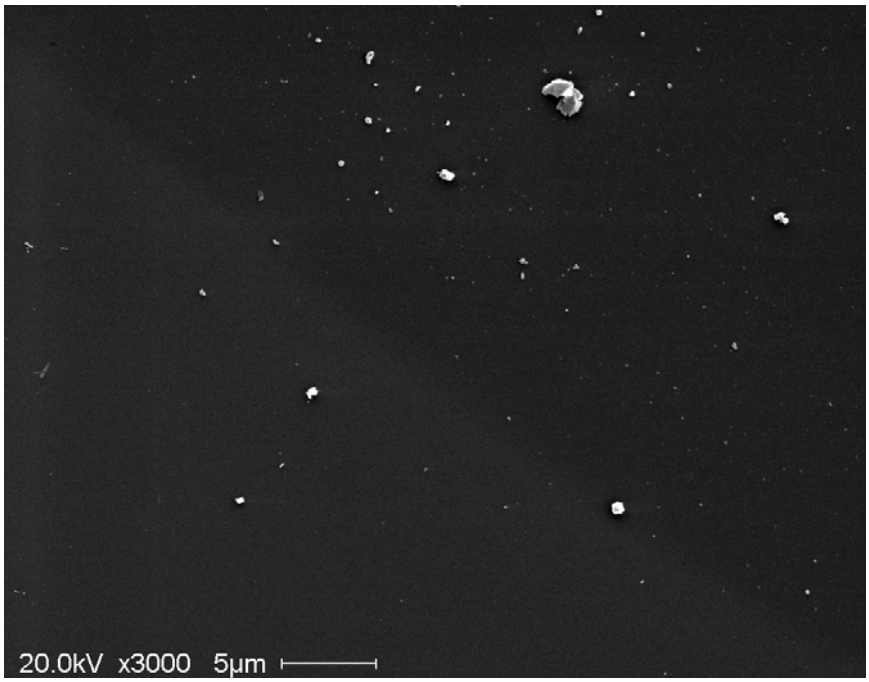

Figure 4.16. SEM micrographs of a carbon film deposited with hollow-anode configuration at a PFN discharge energy of 34.9 J.

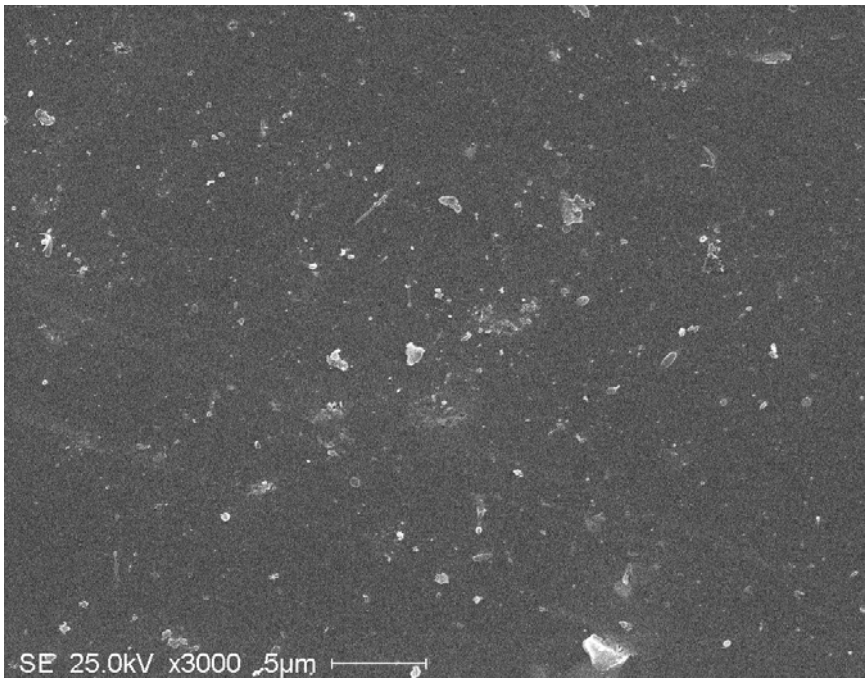

Figure 4.17. SEM micrographs of a carbon film deposited with hollow-anode configuration at a PFN discharge energy of 38.0 J.

Each of the carbon films has an array of particulates. Figure 4.15 shows the film deposited at a discharge energy of 32.3 J, and there are distributed sub-micron particles. The film deposited at 34.9 J has fewer sub-micron particles, but has micron and larger sized irregularly shaped particles, as shown in Figure 4.16. Figure 4.17 shows the film deposited at 38.0J, and there are a large number of various sized irregularly shaped particles.

The titanium films correspond to the titanium rod tip figures in Section 4.3.2.2, Figure 4.14(a-d). The sputtered tip, see Figure 4.14 (a), formed during the PFN discharge energy of 16.9 J and produced a film with many particles and molten droplets, as seen in Figure 4.18. The film deposited at discharge energy 21.3 J produced the film with the least particles and droplets, as seen in Figure 4.19. The shiny smooth tip, see Figure 4.14(b), from the 25.8 J energy discharge produced a film similar to the 21.3 J film with a lower number of particulates and molten droplets, as shown in Figure 4.20. The completely molten tip, see Figure 4.14(d), formed by the 30.3 J discharge energy produced the film with the most and largest molten droplets and few irregularly shaped particulates.

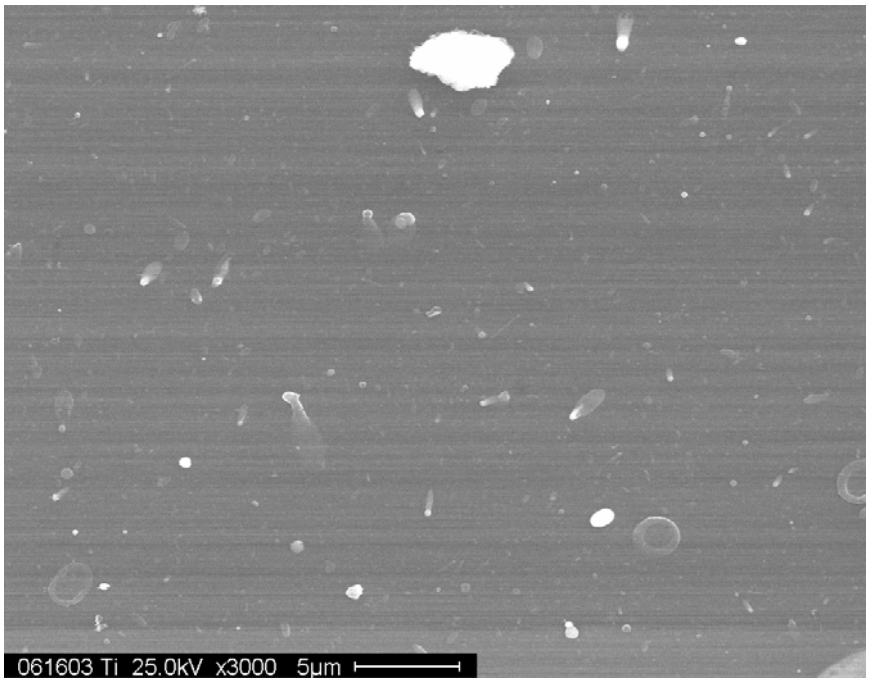

Figure 4.18. SEM micrographs of a titanium film deposited with hollow-cathode configuration at a PFN discharge energy of 16.9 J.

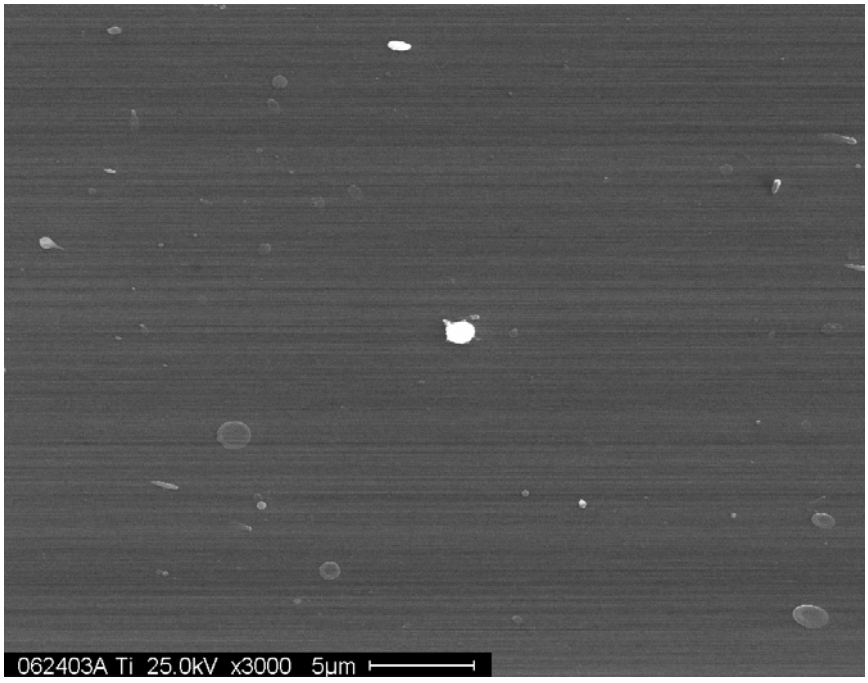

Figure 4.19. SEM micrographs of a titanium film deposited with hollow-cathode configuration at a PFN discharge energy of 21.3 J.

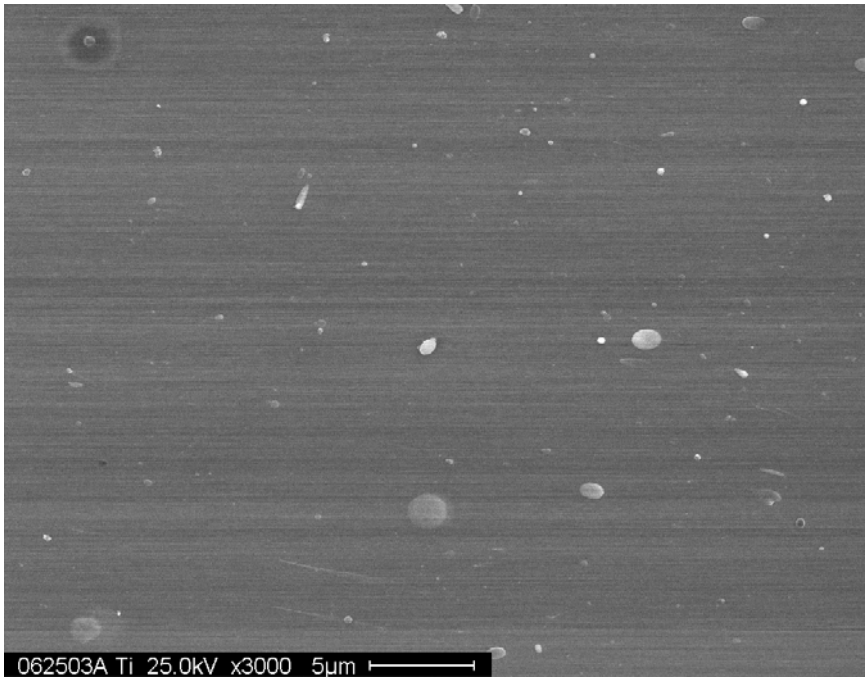

Figure 4.20. SEM micrographs of a titanium film deposited with hollow-cathode configuration at a PFN discharge energy of 25.8 J.

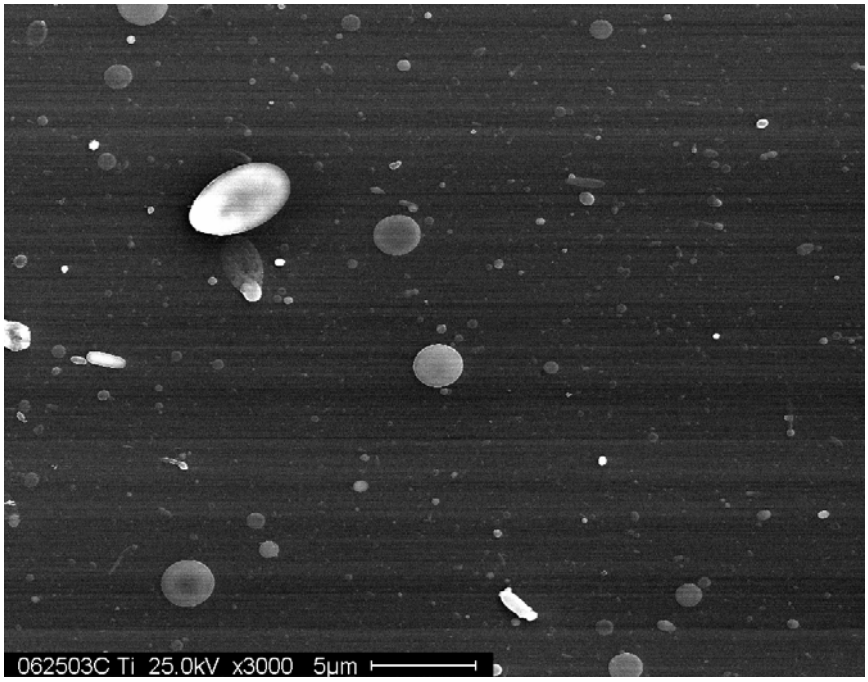

Figure 4.21. SEM micrographs of a titanium film deposited with hollow-cathode configuration at a PFN discharge energy of 30.3 J.

4.4. Titanium-Carbon Dual Plasma Configuration

The dual plasma, high-voltage triggered hollow-electrode transient plasma discharge system consists of two discharge heads, two PFNs, two glow discharge networks, and a vacuum chamber. The same vacuum system is used as described in Chapter 2.

4.4.1. System Description

The dual plasma system utilizes two high-voltage discharge heads as shown in Figure 4.1 and arranged as shown in Figure 4.22. One is a hollow-cathode electrode configuration with a titanium rod-anode, and the second one is a hollow-anode electrode configuration with a carbon rod-cathode. Each discharge head has an independent PFN, and glow discharge network, as shown in Figure 4.2 and 4.2, respectively. The ambient gas used to create the pulsed plasma is argon as in Chapter 4.1.

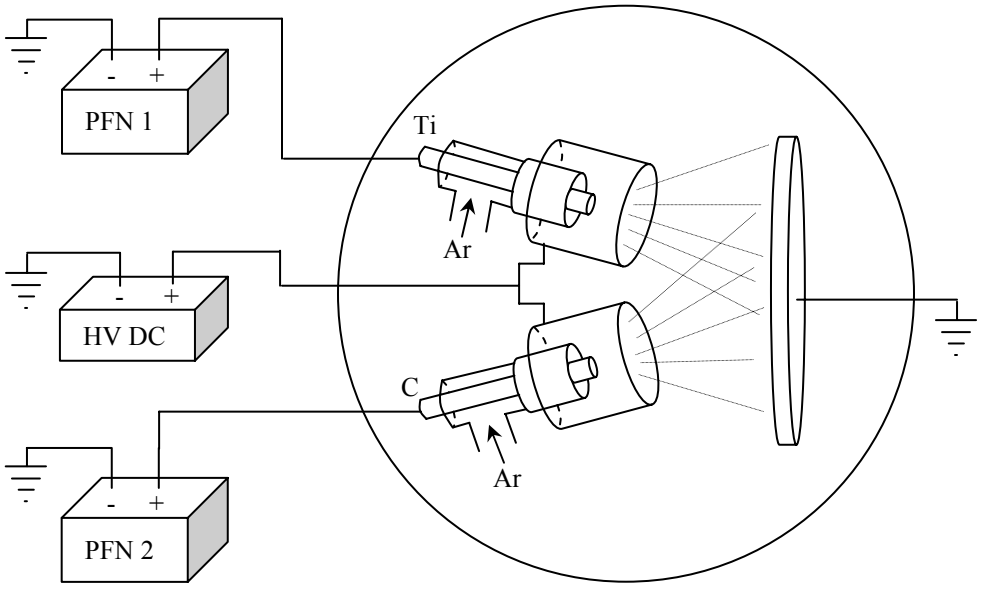

Figure 4.22. Electronically triggered dual hollow-electrode plasma system for TiC film growth.

4.4.2. Characterization of the Thin Films Deposited

In this section the details of the deposition and characterization of simultaneously deposited carbon and titanium thin films by the high-voltage triggered hollow-electrode transient plasma discharge are discussed. The goal is to investigate the process's ability to produce multi-component thin films from two separated material sources to yield TiC thin films. Film deposition rates, SEM micrographs, EDS, and XRD of the films deposited are presented as part of the film morphology studies.

4.4.2.1. Film Thickness Measurements

Film thickness measurements were performed following the same procedure presented in Section 3.2. On-axis film thickness measurements of the titanium-carbon films deposited by argon plasmas were obtained.

This is an initial investigation of the feasibility of simultaneously depositing titanium and carbon films from separated plasmas sources to form a multi component film as TiC or Ti-C. Since the two discharge head have separate PFNs and glow discharge sources, separate conditions for titanium and carbon can be set to attempt to deposit a 1:1 film of titanium and carbon to form TiC. Conditions were chosen as presented in chapter 4.3.2. which will yield equal parts titanium and carbon without damage to the discharge heads.

A film growth rate of 0.5 Å/pulse from each source was chosen, to produce a total of 1.0 Å/pulse. A repetition rate of 4 Hz was chosen since both discharge sources should pulse at the same rate and the deposition rate of titanium is dependent on the frequency while carbon is not. For the titanium discharge system, the PFN initial voltage was set at

90 VDC, and the PFN capacitance was set at 7.2 mF, to produce a PFN total discharge energy of approximately 25.5 J. For the carbon discharge system, the PFN initial voltage was set at 120 VDC, and the PFN capacitance was set at 4.7 mF, to produce a PFN total discharge energy of approximately 32 J. The dual plasma system was allowed to discharge for a total of 1000 pulses to produce an expected 1000 Å thick film for a deposition rate of 1 Å/pulse for each trial.

The two discharge systems pulsed simultaneously, such that there was ± 5.0 μs between the start of the two current pulses, see Figure 4.23. There were no missed pulses from either source. Multiple deposition trials were completed and the film thickness varied and ranged from 230 Å to 1200 Å for an average deposition rate of 0.67 ± 0.42 Å/pulse. This is lower and more varied than expected under the given conditions.

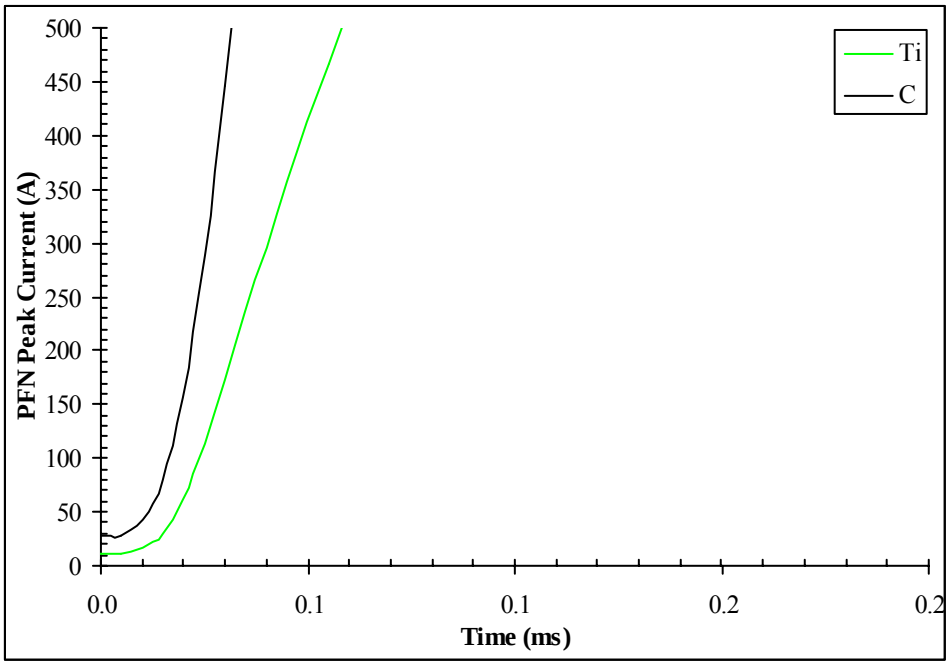

Figure 4.23. Synchronization of the two PFN discharges.

4.4.2.2. Quality of the Deposited Films

SEM micrographs, EDS scans, and XRD results are presented to investigate the quality of the titanium-carbon films deposited by the dual plasma high voltage triggered hollow electrode system. These particular films contain a high density of particles throughout the film surface area.

4.4.2.2.1 Scanning Electron Microscopy of the Thin Films

A typical SEM micrograph is presented in Figure 4.24. The SEM shows the surface morphology of the titanium-carbon film deposited. The film contains a high density of sub-micron particles and molten droplets throughout the film surface area. The angled droplets are a result of the discharge heads not being mounted perpendicular to the substrate surface due to the configuration of the discharge heads within the system.

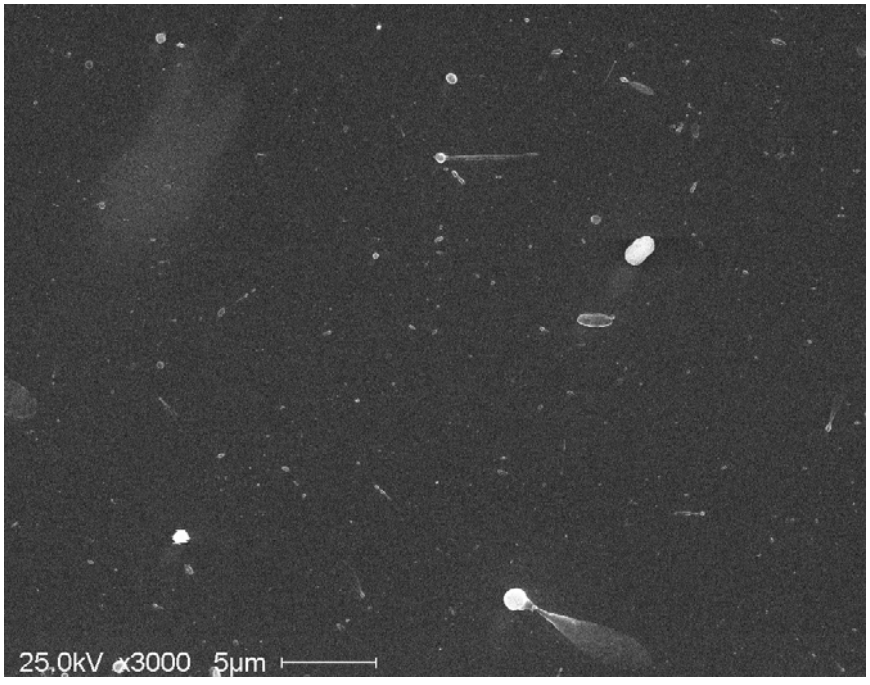

Figure 4.24. SEM micrograph of a titanium-carbon film deposited using the dual hollow-electrode configuration.

4.4.2.2.2. Electron Dispersive X-Ray Spectroscopy of the Thin Films

The two films, deposited with a substrate temperature of 500 ^{o}C, were examined by EDS and the composition spectrum for the titanium-carbon films dual plasma system is shown in Figure 4.25 and 4.26. Figure 4.25, for a 725 Å thick film shows a predominant peak at 0.28 keV, corresponding to the carbon K 1s orbital, and other peaks at 0.46 and 0.56 keV, corresponding to the titanium L_I 2s through L_{III} $2p_{3/2}$ orbital, as shown in Table 2.2. The EDS quantification of the film shows 37.49% of carbon and 13.81% of titanium by atomic weight percentage, as shown in Table 4.1. The significant material source for this electrode configuration is from the carbon hollow cathode. There is a dominant oxygen peak also which is expected since titanium films oxidize rapidly when exposed to air for the first several nanometers of the film.

The composition spectrum for second film which is 1164 Å thick is shown in Figure 4.26. The spectrum shows a peak at 0.27 keV, corresponding to the carbon K 1s orbital, and other peaks at 0.46 and 0.56 keV, corresponding to the titanium L_I 2s through L_{III} $2p_{3/2}$ orbitals, as shown in Table 2.2. The EDS quantification of the film shows 6.76% of carbon and 7.96% of titanium by atomic weight, as shown in Table 4.2. This is very close to a 1:1 ratio of titanium to carbon for the possibility of a majority TiC film.

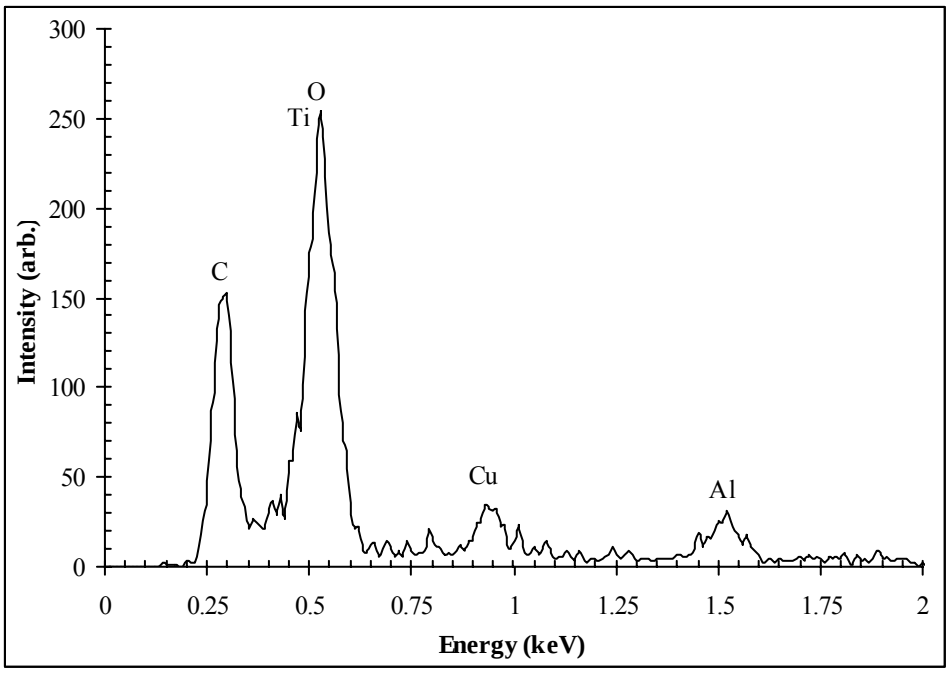

Figure 4.25. EDS spectrum of a titanium-carbon film deposited using the dual hollow-electrode configuration, 500 ºC substrate temperature, and 725 Å thick.

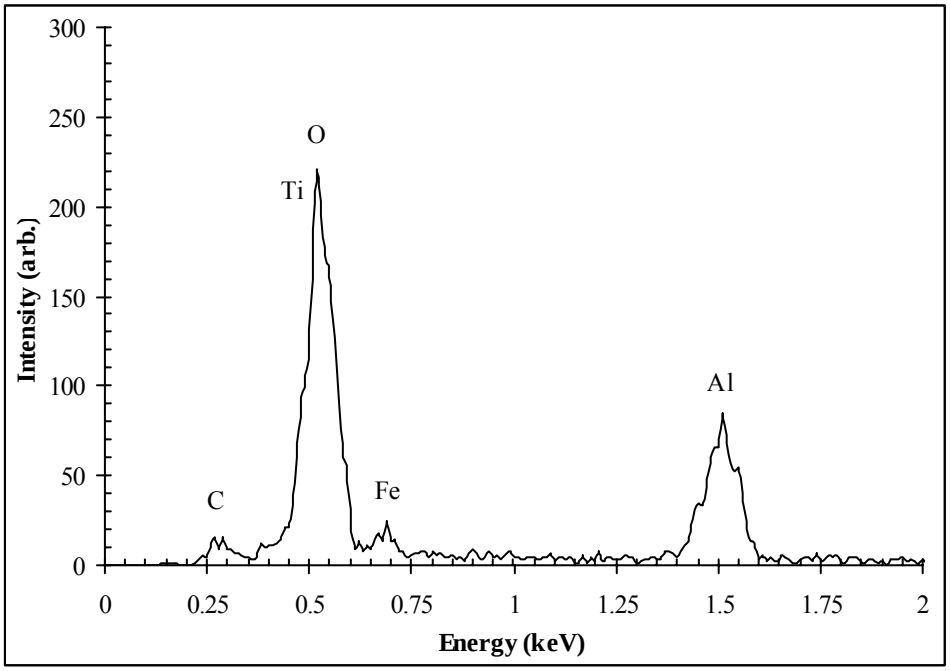

Figure 4.26. EDS spectrum of a titanium-carbon film deposited using the dual hollow-electrode configuration, 500ºC substrate temperature, and 1164 Å thick.

Element	Wt %	At %
C K	21.40	37.49
Ti L	31.50	13.81
O K	30.53	40.07
Cu L	9.45	3.12
Al K	7.07	5.50
Total	100.00	100.00

Table 4.1. Weight percentage and atomic weight percentage obtained from the EDS spectrum for a titanium film deposited at 500 ºC and 725 Å thick.

Element	Wt %	At %
C K	3.52	6.76
Ti L	16.53	7.96
O K	36.82	53.09
Fe L	10.61	4.38
Al K	32.51	27.80
Total	100.00	100.00

Table 4.2. Weight percentage and atomic weight percentage obtained from the EDS spectrum for a titanium film deposited at 500 ºC and 1164 Å thick.

4.4.2.2.3. X-Ray Diffraction of the Thin Films

In X-ray Diffraction (XRD), a beam of X-rays is focused on a sample where crystals may or may not have varied and random orientation. A monochromator gives an incident beam of only the K alpha Cr line, the x-rays will be reflected, not fluoresced, at the appropriate Bragg angle. The 2D spacings between the denser layers in the crystal lattice can be measured. XRD can be used to identify minerals, but also to analyze one element in one mineral by selecting a known 2D spacing and counting the intensity.

The 2Θ range of 20 to 80 degrees was scanned where the predominant peaks for TiC and TiO_2 appear. Three films deposited with a substrate temperature of 500 ºC were investigated. Figure 4.27 shows an XRD spectrum for a successful titanium-carbon film. Figure 4.27 shows the XRD spectrum for the film with the expected film thickness, 1164 Å, and TiC (111) and TiC (200) peaks appeared. The intensity of the peaks is low so the

abundance of TiC in the film may be low. Figure 4.28 shows a picture of a typical high-voltage triggered PFN discharge.

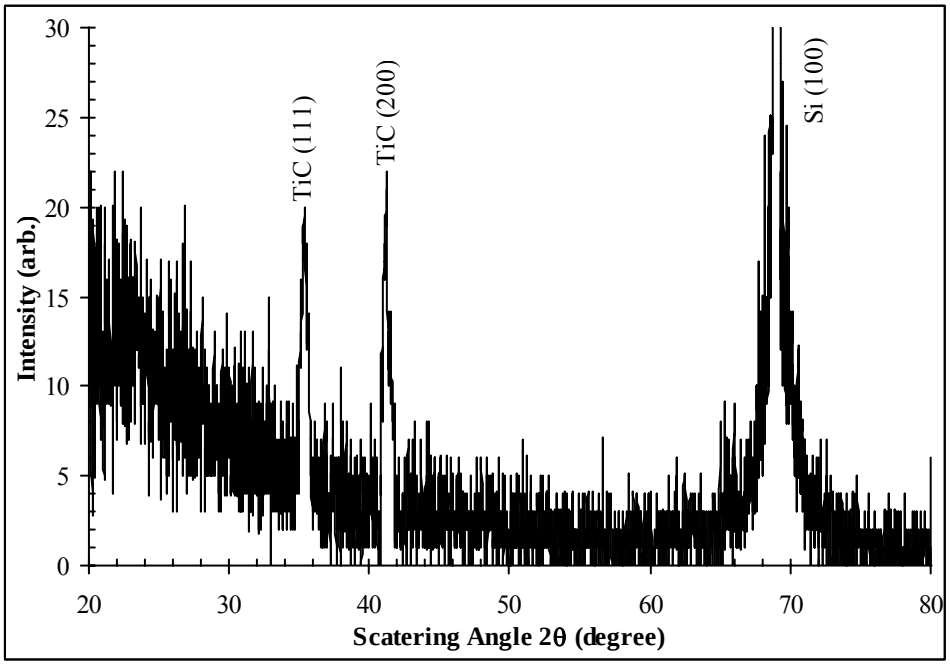

Figure 4.27. XRD spectrum of a titanium-carbon film deposited using the dual hollow-electrode configuration and 500 ºC substrate temperature.

Figure 4.28. Picture of a high-voltage triggered PFN discharge.

CHAPTER 5. CONCLUSION

The aim of this work was to develop a reliably triggered plasma source that produces ionized vapor pulses of metallic species using a CO_2 laser trigger to initiate the plasma pulse discharge. Investigations examining the discharge reliability and process parameters have developed better control of the process. PFN discharge reliability was found to be dependent on triggering CO_2 laser fluence and laser modes incident on the discharge head cathode, on ambient pressure, and on the initial voltage of the PFN. Through proper selection of these parameters PFN discharge reliability was raised from 10 - 18% reliability to 100% reliability. Once the reliability issue was resolved proper investigations to characterize the deposition technique could be pursued.

Cathode corrosion by the triggering laser which was found to be contaminating the substrate and vacuum system was also found to be the source of the initially deposited films, rather than the plasma discharge. Cathode corrosion was found to be dependent on the triggering CO_2 laser fluence incident on the discharge head cathode as well as the PFN discharge energy. At high enough levels of CO_2 laser and PFN discharge energies hollow-cathode corrosion was eliminated, ridding the process of this source of contamination. Corrosion was still present with the use of the hollow-anode configuration which permitted deposition of the rod-cathode material, a desired configuration of the project. Contamination of the growing films was protected from this corroded material by installing ablation shielding on the discharge head, separating the corrosion from the plasma.

Through investigations characterizing the PFN discharge process, the discharge was found to be dependent on the ambient pressure of the system as well as the type of gas used. The discharge was also found to be dependent on the PFN capacitance, initial voltage, and inductance. Maximum output of the process can be adjusted through appropriate values of these parameters.

Through characterization of the deposited films and varying the electrode materials the source of the deposited material was found to originate from the cathode of the discharge head indicating that the main process mechanism is ion sputtering of the cathode and not electron bombardment of the anode. Characterization of the films also determined the deposition rate of carbon films using this configuration and the minimal discharge energy required. Through the use of film deposition studies and ICCD optical diagnostics, there was found to be no film deposition rate dependence on an applied magnetic field strength up to 18 millitesla. However, the light emission of the plasma is affected.

Micro-droplets and macro-particles are found in the plasma and deposited films. The population of these particulates increases as the discharge energy and deposition rate is increased. Attempts to block or filter the micro-droplets from the plasma were not investigated, but the parameters to minimize their production were investigated. Other groups have reported effective low angle shielding and magnetic filters to reduce or eliminate the particles.

In order to simplify the hollow-electrode system and completely eliminate the cathode corrosion as a source of contamination, the triggering CO_2 laser was eliminated and an electronic high voltage triggering of the hollow-electrode process was investigated. The controlled triggering utilized the inherent capacitive effect of the

discharge head geometry to set the frequency of the PFN discharge. With this configuration, carbon film deposition rates compared to the laser-triggered system were obtained, but at much lower PFN discharge energies. The lower PFN discharge energy requirements also reduced the system component fatigue such as PFN power supplies and discharge head components. The deposition of titanium films was also possible using this configuration. Titanium could not be reliably deposited using the laser-triggered configuration due to the high discharge energy requirements and characteristics of titanium such as high melting temperature.

Once both titanium and carbon could be reliably deposited, another goal of the project could be investigated, that of multi-component film deposition of predetermined stoichiometry or multi-layer films. A dual-plasma system was examined for attempting to deposit TiC films using separate carbon and titanium sources. Films containing TiC were deposited. However, reproducibility issues need to be addressed for this to be a viable deposition method for multi-component films.

REFERENCES

[1] W. D. Sproul, "Physical vapor deposition tool coatings", *Surface and Coatings Technology* **81**, 1-7 (1996).

[2] W. Grzesik, Advanced Protective Coatings for Manufacturing and Engineering, Cincinnati: Hanser Gardner Pub., Chp. 5 (2003).

[3] J. L. Vossen and W. Kern (eds.), Thin Film Processes II, San Diego: Academic Press, pp. 11-77 and 209-280 (1991).

[4] J. J. Cuomo, J. M. E. Harper, C. R. Guarnieri, D. S. Lee, L. J. Attanasio, J. Angilello, C. R. Wu, and R. H. Hammond, *J. Vac. Sci. Technol.* **20**, pp. 349-354 (1982).

[5] D. M. Mattox, *J. Appl. Phys.* **34**, 2493 (1963).

[6] D. M. Mattox, in "Deposition Technologies for Films and Coatings" (RF Bunshah, ed.) pp. 244-287, New Jersey: Noyes Pub., (1982).

[7] T. Takagi, "Role of Ions in Ion-Based Film Formation", *Thin Solid Films* **92**, pp. 1-17 (1982).

[8] D. M. Mattox, "Fundamentals of Ion Plating", *J. Vac. Sci. Technol.*, **10**, no. 1, pp. 47-52 (1973).

[9] R. D. Bland, G. J. Kominiak, and D. M. Mattox, "Effect of Ion Bombardment During Deposition on Thick Metal and Ceramic Deposits", *J. Vac. Sci. Technol.* V11(4), pp. 671-674 (1974).

[10] T. Spalvins, "Survey of Ion Plating Sources", *J. Vac. Sci. Technol.*, **17**(1), pp. 315-321 (1980).

[11] H.K. Pulker, M. Larden, R. Buhl, and E. Moll, *J. Vac. Sci Technol.* **A4**(6), 2922-2924 (1986).

[12] A. J. Perry and H. K. Pulker, *Thin Solid Films* **124**, 323 (1985).

[13] A. Anders, I. G. Brown, R. A. MacGill, and M. R. Dickinson, *J. Phys. D: Appl. Phys.* **31**, pp. 584-587 (1998).

[14] D. M. Mattox, Handbook of Physical Vapor Deposition (PVD) Processing, New York: Noyes, pp. 378-397 (1998).

[15] I. G. Brown, "Cathodic Arc Deposition of Films", *Annu. Rev. Mater. Sci.* **28**, pp. 243-269 (1998).

[16] A. Anders, S. Anders, A. Förster, and I. G. Brown, "Pressure Ionization: Its Role in Metal Vapour Vacuum Arc Plasmas and Ion Sources", *Plasma Sources Sci. Technol.*, **1**, pp.263-270 (1992).

[17] R. L. Boxman, D. Sanders, and P. J. Martin, Vacuum Arc Science and Technology, New York: Noyes, pp. 396-453, (1996).

[18] J. Kutzner and H. C. Miller, "Integrated Ion Flux Emitted from the Cathode Spot Region of a Diffuse Vacuum Arc", *J. Phys. D.: Appl. Phys.*, **25**, pp. 686-693 (1992).

[19] V. M. Lunev, V. G. Padalka, and V. M. Khyoroshikh, *Soc. Phys. Tech. Phys.* **22**, pp. 858 (1977).

[20] P. Mukherjee, J. B. Cuff, and S. Witanachchi, *Appl. Surf. Sci.* **127-129**, pp. 620-625 (1998).

[21] S. Witanachchi, Y. Ying, A. Miyawa, and P. Mukherjee, *Mater. Res. Soc. Symp. Proc.* **483**, pp. 185 (1998).

[22] P. J. Martin, *Vacuum* **36**, pp. 585 (1986).

[23] V. A. Osipov, V. G. Padalka, L. P. Sablev, and R. I. Stupak, *Inst. And Exp. Techniques*, **21**(6), pp. 1650-1652 (1978).

[24] C. W. Kimblin, "Erosion and Ionization in the Cathode Spot Regions of Vacuum Arcs", *J. Appl. Phys.* **44**, pp. 3074-3078 (1973).

[25] C. W. Kimblin, "Cathode Spot Erosion and Ionization Phenomena in the Transition from Vacuum to Atmosphere Pressure Arcs", *J. Appl. Phys.* **45**, pp. 5235-5244 (1974).

[26] W. D. Davis and H. C. Miller, "Analysis of the Electrode Products Emitted by DC Arcs in a Vacuum Ambient", *J. Appl. Phys.* **40**, pp. 2212 (1962).

[27] D. T. Tuma, C. L. Chen, and D. K. Davies, *J. Appl. Phys.*, **49**(7), (1978).

[28] T. Utsumi and J. H. English, *J. Appl. Phys.* **46**, pp. 126-131 (1975).

[29] J. E. Daalder, *J. Phys. D: Appl. Phys.*, **9**, pp. 2379-2395 (1976).

[30] S. Witanachchi, P. Mahawela, and P. Mukherjee, “Laser-Triggered Hollow-Cathode Plasma Process for Film Growth”, J. Vac. Sci. Technol. A, **22**(5), pp. 2061-2066, (2004).

[31] H. Ehrich, B. Hasse, M. Mausbach, and K. G. Muller, *IEEE Trans. Plasma Sci.* **18**, pp. 895-903 (1990).

[32] I. I. Aksenov, V. A. Belous, V. G. Padalka, and V. M. Khoroshikh, *Sov. J. Plasma Phys.* **4**(4), pp. 425-428 (1978).

[33] I. I. Aksenov, V. G. Padalka, N. S. Repalov, and V. M. Khoroshikh, *Sov. J. Plasma Phys.* **6**(2), pp. 173-176 (1980).

[34] A. Anders, R. A. MacGill, M. M. M. Bilek, and I. G. Brown, U. S. Patent 6,465,780, October 2002.

[35] B. K. Gan, M. M. M. Bilek, D. R. McKenzie, P. D. Swift, and G. McCredie, “Optimizing the Triggering Mode for Stable Operation of a Pulsed Cathodic Arc Deposition System”, *Plasma Sources Sci. Technol.,* **12**, pp. 508-512 (2003).

[36] K. Yukimura, R. Isono, T. Monguchi, and K. Yoshioka, *J. Vac. Sci. Technol. B,* **17**, pp. 871-874 (1999).

[37] G. C. Watt and P. J. Evans, *IEEE Trans. Plasma Sci.,* **21**, pp. 547-551 (1993).

[38] A. Anders, I. G. Brown, R. A. MacGill, and M. R. Dickinson, “’Triggerless’ Triggering of Vacuum Arcs”, *J. Phys. D: Appl. Phys.,* **31**, pp. 584-587 (1998).

[39] A. G. Nikolaev, G. Y. Yushkov, E. M. Oks, R. A. MacGill, M. R. Dickinson, and I. G. Brown, “Vacuum Arc Trigger Systems Based on *E*x*B* Discharges”, *Rev. Sci. Instrum.,* **67**, pp. 3095-3098 (1996).

[40] R. L. Boxman, “Triggered Mechanisms in Triggered Vacuum Gaps”, *IEEE Trans. Electron Devices.,* **24**, pp. 122-128 (1997).

[41] G. R. Govinda Raju, R. Hackman, and F. A. Benson, “Firing Characteristics of a Triggered Vacuum Gap Employing a Dielectric Coated with a Semiconducting Layer”, *J. Appl. Phys.,* **48**, pp. 1101-1105 (1977).

[42] I. I. Aksenov and V. A. Belous, *High Temperatures* **17**, pp. 103 (1979).

[43] I. I. Aksenov and V. A. Belous, *Instrument & Experimental Tech.* **22**(3), pp. 785-786 (1979).

[44] D. B. Geohegan, in: D. B. Chrisey and G. K. Hubler (eds), Pulsed Laser Deposition of Thin Films, New York: Wiley, pp. 115-161 (1994).

BIBLIOGRAPHY

K. Ahmed, *A Novel Dual Laser Ablation Process for High Quality Film Growth,* Ph.D. Dissertation, University of South Florida, 1996. S.

J. T. Cheung and H. Sankur, "Growth of thin films by laser-induced evaporation," CRC Ctrit. Rev. Solid State Mater. Sci., Vol. 15, no. 1, pp. 63-109

D. B. Geoheagn, in: D. B. Chrisey and G. K. Hubler (Eds), *Pulsed Laser Deposition of Thin Films*, New York: Wiley, 1994, pp. 115-166.

J. Hecht, *The Laser Guidebook*, New York: McGraw-Hill, Inc., 1992, pp. 159-183.

A. Siegman, *Lasers*, California: University Science Books, 1986, pp. 491-493.

R. K. Singh, O. W. Holland, and J. Narayan, "Theoretical model for deposition of superconducting thin films using pulsed laser evaporation technique," J. Appl. Phys., Vol. 68, no. 1, pp. 233-247, 1990.